Norwegian University
of Life Sciences

Master's Thesis 2021 30 ECTS
Faculty of Science and Technology

Influence of Mean Tension on Mooring Line Fatigue Life for a Floating Offshore Wind Turbine

Middelspenningens påvirkning på forankringsliners utmattingslevetid for flytende vindturbiner

Ludvik Kjosås Bergmann
Mechanical Engineering and Process Technology

Abstract

A growing energy demand throughout the world has seen an increasingly higher interest in wind turbines operating in deeper waters. By reaching deeper waters, higher wind speeds and less turbulence are more likely. Annoyance with visual and noise attributes of increasingly larger wind turbines will not affect residents. Currently, the cost of energy for floating concepts is too high and the technology is not yet competitive. As a result, the costs for floating wind must be reduced to become a viable alternative for energy production.

Recently published studies have documented a significant mean load effect on fatigue capacity for offshore mooring chains, showing that a reduction of mean loads gives an increase in fatigue life. Standard design practice has been to base S-N fatigue design curves on tests carried out at 20 % of the chain minimum breaking load (MBL). These curves are then used to compute damage for all tension cycles, regardless of their actual mean value.

This thesis investigates the mean load dependency in mooring chains for a floating offshore wind turbine by describing the mean load tension associated with each stress cycle in three different ways. The first method takes the average of the maximum and minimum load in each cycle, namely the cycle mean. Second, a 1-hour mean load representation for the sea state the cycle is encountered in follows, called the 1-hour mean. Finally, the mooring lines pre-tension is applied as a basis for the mean load. A parametrized S-N curve design approach developed by Fernandez et al. [1] is used to account for the mean tension while keeping the same level of confidence of the existing curves. The method applies a Smith-Watson-Topper correction model, which includes relevant stress concentration factors for R3 graded chains. Time-domain analysis of a semi-submersible floating platform has been performed on the INO WINDMOOR 12 MW wind turbine to provide reliable results, under relevant wind and wave loads. The model was exposed to 21 different FLS conditions, all performed at a water depth of 150 m.

For most sea states, the mean tension is seen to be below 20 % MBL, even though some deviations occur. Furthermore, slight deviance between 1-hour mean and cycle mean can be found, due to the rainflow counting algorithm accounting for cycle means, also half-cycles. However, a significant reduction in fatigue damage can be seen for all mooring lines, especially for the lines located on the leeward side of the wind.

Sammendrag

Et økende energibehov i verden har gitt større interesse for at vindturbiner skal kunne operere i dypere farvann. Dypere farvann betyr at vindhastigheten øker, samt mindre turbulens som fører til en mer effektiv energiutnyttelse. Ved å flytte vindturbinene lengre ut i havet vil ikke mennesker påvirkes i særlig grad av støy og visuelle forhold. Teknologien for flytende havvind er i stadig utvikling og kommersialiseres i større grad enn tidligere, selv om det per i dag ikke er særlig kostnadseffektivt. For at dette konseptet skal være levedyktig fremover, må kostnadene reduseres slik at det kan være et fornuftig alternativ for global energiproduksjon.

Nylig publiserte studier har vist en signifikant betydning av middelspenningens innvirkning på utmattingskapasiteten til offshore forankring, og har samtidig vist at en reduksjon av middelspenningen kan øke utmattingslevetiden. Standard S-N kurver for ankerkjettinger er konstruert med hensyn på 20 % av minimal knekklast (MBL). Disse kurvene gjør seg gjeldende for alle spenningssykler, uavhengig av middelspenningsverdien. Dette medfører en underestimering av utmattingslevetiden for kjettinger som ikke utsettes for høye middelspenninger, og en tilsvarende overestimering av levetiden til enheten som faktisk er utsatt for middelspenninger over 20 % MBL.

Denne oppgaven undersøker avhengighetsforholdet til middelspenningen i ankerkjettinger for flytende vindturbiner ved å beskrive middelspenningen som er assosiert med hver spenningssykel på tre ulike måter. Den første måten tar utgangspunkt i gjennomsnittet av maksimal og minimal last i hver sykel, derav navnet sykel-middel. Den neste metoden baseres på 1-times middelspenning for hver sjøtilstand, og kalles derfor 1-times middel. Til slutt undersøkes muligheten for å benytte ankerkjettingens forspenning som utgangspunkt for middelspenningen. En parametrisert S-N kurve utviklet av Fernandez et al. [1] benyttes som utgangspunkt for å ta høyde for middelspenningen, samtidig som konfidensintervallet til eksisterende kurver ivaretas. Metoden benytter seg av Smith-Watson-Topper korreksjonsmodellen, hvor relevante spenningskonsentrasjonsfaktorer (SCF) for grad R3 av ankerkjettinger er inkludert. En tidsdomene analyse av den halvt nedsenkbare INO WINDMOOR 12 MW vindturbinen er gjennomført for å generere pålitelige resultater til analysen, under 21 ulike vind- og bølgelasttilfeller ved en dybde på 150 m.

I samtlige simulerte sjøtilstander ligger middelspenningen under 20 % MBL, selv om noen avvik forekommer. Videre foreligger det en liten forskjell mellom 1-times middel og sykel-middel-metoden. Resultatene viser likevel at det potensielt eksisterer en betydelig reduksjon i utmattingsskaden for samtlige ankerliner, og da spesielt for liner som ligger i le av vinden.

Acknowlegdement

The work with this thesis has been carried out at the Norwegian University of Life Sciences at Ås, Norway during the spring semester of 2021, and is the end of a master's degree within the field of mechanical engineering and process technology. The topic of interest was chosen after gaining insights into the maritime industry during employment at BW Offshore during the summer of 2020, which enhanced my interest in complicated technologies. The main topic of the thesis was later developed in collaboration with SINTEF Ocean, under the supervision of Marit Irene Kvittem. I would like to thank you very much. In addition, I would also like to thank Tor Anders Nygaard for his help as a co-supervisor for this thesis.

Working with the thesis has been very interesting, opening up a new world of undiscovered areas for me personally. Being unfamiliar with the software SIMA, and running analysis was challenging and took some time to discover, even being warned. This also applies to the post-processing of all results in Python. I also want to express my deep gratitude to all of whom helped me to develop codes and functions.

I would also like to thank Erling Lone for his helpful insights on the topic of interest. It has been vital for the progress of the thesis. Further inputs and filtering routines in Python are acknowledged. All of this would not have been possible without the help of Marit I. Kvittem. Lastly, I would like to thank my fellow student colleagues at Hemsen for valuable discussions throughout these five years at NMBU.

Ås, June, 2021

Ludvik K. Bergmann

Contents

List of Figures

List of Tables

List of abbreviations

ALS Accidental Limit State

BEM Blade Element Momentum

DFF Design Fatigue Factor

DLC Design Load Case

DLE Design Load Effect

DOF Degrees of Freedom

DNV Det Norske Veritas

FLS Fatigue Limit State

FOWT Floating Offshore Wind Turbine

FPSO Floating, Production, Storage, Offloading

GE General Electric

IEA International Energy Agency

IEC International Electrotechnical Commission

JONSWAP Joint North Sea Wave Project

MBL Minimum Breaking Load

ML Mooring Line

MWL Mean Water Line

OPB Out-of-plane bending

OG Oil & Gas

PM Pierson-Moskowitz

RNA Rotor-Nacelle Assembly

ROSCO Reference OpenSource Controller

RPM Rotations per Minute

SCF Stress Concentration Factor

SPAR Single Point Anchor Reservoir

SWT Smith-Watson-Topper

TLP Tension Leg Platform

ULS Ultimate Limit State

VSVP Variable-speed-variable-pitch

List of Symbols

a	Axial induction factor
A	Rotor swept area
α	Height exponent
A_d	Actuator disc area
a_D	Intercept parameter
β	Weibull scale parameter
γ	Weibull form parameter
c	Chord length
C_D	Drag coefficient
C_L	Lift coefficient
C_M	Pitching moment coefficient
C_p	Power coefficient
C_T	Thrust coefficient
F_T	Rotor thrust
f	Wave frequency
Hs	Significant wave height
I	Turbulence intensity
L_k	Velocity component integral scale parameter
σ	Standard deviation
r	Rotor radius
P	Power
p	Probability of occurrence
U	Wind speed
U_∞	Far-field wind velocity
$\bar{U}$	Mean wind speed
Tp	Peak wave period
Ws	Wind speed
z	Height variable

1 Introduction

1.1 Motivation

Throughout the globe, large areas exist that are considered to be appropriate for the development of renewable energy. Floating offshore wind turbines are considered to be quite immature and are one of the technologies where the associated potential is considerable. There is still large room for improvement and new innovations within the field may lead to reductions in costs. Further research and standardization within the industry will lead to more competition between companies and give valuable insight into the risks included in offshore wind projects.

The knowledge and technology behind floating offshore wind have many similarities with the technology being utilized in the oil and gas industry. If a country, such as Norway, is able to use previous knowledge and experience in that field, it will ultimately lead to added value in several businesses by being a leading actor as an international supplier. Again, Norway can position itself as an international supplier of offshore wind technology and use its competence and ability to innovate within maritime and offshore businesses [18].

For Europe to become carbon neutral within 2050, and at the same time achieve the goals in the Paris agreement to limit global emissions, it is necessary to promote an energy transition to renewable energies. Thus, floating offshore wind will become a core solution to this problem. The cost of FOWTs exponentially increases with water depth as mooring line material volumes increase drastically. Therefore, an important aspect is to reduce these costs and at the same time understand the fatigue capacity of mooring chains to mitigate the probability of accidents. A contribution to this is to detect the mean tension effects, and show that a reduction of the current mean load standard design curves may lead to a considerable increase in fatigue life.

1.2 Previous research

Recent studies have claimed that the importance of mean load and its contribution to fatigue life of mooring chains is considerable, showing that a reduction of the mean load gives an increase in fatigue life. Current S-N design curves from DNVGL-OS-E301 [11], applicable to determine the fatigue life, are based on fatigue test performed at a mean load of 20 % of minimum breaking load (MBL). These curves are then used to compute the damage of all tension cycles, regardless of their mean value. Mean loads for mooring chains usually experience less than 20 %, however, a problem has been to quantify the dependency.

One approach to verify the dependency was carried out by Fernandez et al. [1] who ran fatigue tests for a large number of mooring chains for different chain diameters and grades, as well as mean tensions ranging from 7-20 % MBL. Furthermore, they applied Smith-Watson-Topper (SWT) mean stress correction model to transform the stress states into associated mean tensions. This resulted in a new correction function for the intercept parameter of the S-N curves while keeping the same confidence level as existing curves.

The work of Fernandez et al. [1] made way for further studies on the intercept parameter and the parametrized S-N design curve, resulting in a comparative study investigating the mean loads experienced during fatigue damage accumulation on a semi-submersible unit (O&G), operating in harsh Norwegian sea conditions by Lone et al [19]. In addition, they proposed a method to associate mean load with stress cycles in three different ways; cycle means – calculated as an average of the maximum and minimum load in each individual cycle, a 3-hour mean – based on the 3-hour mean load for the sea state the cycle is encountered in and finally the pretension – represented by the component's pretension. Moreover, by comparing the original fatigue design curve yielded from DNVGL-OS-E301 to the mean load methods, a single correction factor was proposed to allow for mean load correction. The research clearly showed that the orientation of the mooring line was of great importance, together with wind and wave directions. However, the most important result was the fact that the accumulated S-N design curves yielded too high mean loads compared to actual mean loads for the mooring systems, hence a reduced fatigue life. By applying the mean load stress correction methods, fatigue life could be extended by a significant amount of time.

Mean tension dependency with the intercept parameter method presented in this thesis has never been studied for a FOWT. The mooring lines of a semi-submersible FOWT will experience large differences in mean loads depending on the line orientation. Thus, higher mean loads on the windward side and lower mean loads on the leeward side during power production. For semi-submersible units (O&G), the highest fatigue damage reduction can be seen on the leeward side of the dominating wave direction. Contrary to a semi-submersible unit, the motion response of FOWT is more wind dominant.

1.3 Objective

The goal of this master thesis is to understand and quantify the mean tension dependency for the mooring lines of a FOWT, to deliver realistic design curves with unified reliability levels. For this assessment, the INO WINDMOOR 12 MW turbine is used as a case study in an aero-hydro-servo-elastic model implemented in SIMA. To complete this task these questions are investigated:

- Which mean load levels will a semi-submersible FOWT be exposed to?
- How does different mean load cycle counting methods influence mooring line fatigue life?
- Can a simplified form of a single mean load correction factor be used to provide understandable mean load results?

At the time of writing this thesis, no standard guidelines for assessing the mean tension in mooring lines exist for FOWT. Standard engineering practice is based on 20 % MBL for S-N design curves, which is well above the typical loads for most real mooring lines.

1.4 Scope

For the investigation of these research questions, FLS time-domain simulations are performed on INO WINDMOOR 12 MW with a total of 21 different design load conditions. The structural behaviour was validated and compared to the base case. In addition, different performance parameters were verified to check that the simulations worked accordingly. Further, the fatigue damage was calculated through modified Python scripts, including a method of obtaining mean tensions and an evaluation of them.

Mean tension dependency has never been evaluated with the intercept parameter method for FOWT. A total of three different mean tension cycle counting methods were analysed with the focus of detecting variations and differences, and to see their influence on the mooring line fatigue life.

2 Background

Floating offshore wind turbines have had a greater focus in recent years and the market seems to increase incentives for an energy transition from fossil fuels into renewable energy resources. Continuous efforts are devoted to the development of wind energy technology to exploit wind energy resources in deeper waters. This chapter gives an overview of the development of the offshore wind sector and different mooring concepts are introduced. Furthermore, insight to mean tension and its influence on fatigue is briefly described.

2.1 Development of floating offshore wind

2.1.1 Historical perspective

For several centuries windmills have been used for beneficial purposes such as grinding and pumping water. Towards the end of the 19^{th} century, the first wind turbine was used for electricity production and was constructed by Charles F. Brush and was a 12 kW direct current windmill generator. In the 1970s, the oil market price experienced a great increase, which initiated countries to look into other options for energy production, and several programs for research and development started. Prototypes of vertical-axis designs using straight blades were introduced in the UK, while the USA tested a horizontal-axis 3 MW wind turbine in 1981 [20]. Important engineering information was gained through these research programs and the development progressed.

As the oil market price and limited fossil fuel resources was the stimulus for the development of wind energy in the 70s, the main driver these days are based on lower emissions and a greener energy transition. Wind energy has been identified as having a key role in the supply of renewable energy, and onshore wind sites in the US are now being re-equipped with larger modern wind turbines [20].

The past 20 years have seen a rise in the offshore wind industry. In Norway, it all started in 2001 with Statoil's Hywind project. After years of testing, a full-scale solution was ready in 2009, located west of Karmøy with a 2.3 MW turbine. They continued the development of floating wind turbines and completed the world's first floating wind park, Hywind Scotland, which has produced electricity since 2017 with a total installed capacity of 30 MW consisting of five 6 MW turbines. The solution is based on a spar-buoy design.

2.1.2 Current situation and future predictions

The first offshore wind turbine was installed in Nogersund, Sweden in 1990 and was a 220 kW pilot-turbine. Furthermore, throughout the 21st century the trend has been increasing, and in 2019, new installations in Europe reached 15.4 GW, whereas 24 % was offshore wind with a capacity of 3.6 GW. Around half of the offshore installations were located in the UK with the remaining in Germany, Belgium, Denmark, and Portugal. According to Europe's largest wind power network, WindEurope [21], a total capacity of 205 GW of wind power had been installed in Europe with 11 % being offshore.

Since there is an abundance of wind resources available around the world, wind farm developers onshore install increasingly larger turbines. This is inevitably cost-driven as well, due to a larger power per unit. However, with the visual impact and noise generated and the fact that there is a need for large expanses of land to set up these farms, the wind power expansion slows down. Nonetheless, those issues are not existing when wind turbines are built at sea. The future of developing offshore wind parks will still require large areas with good wind resources available and as few conflicts of interest as possible. As the costs of development and operation offshore are more expensive than landbased fields, accurate site predictions are of great importance.

Due to COVID-19 restrictions in the wind power industry, the supply chain experienced disruptions in the first semester of 2020 concerning production and assembly. However, Europe still managed to increase its capacity by 5.1 GW, where 1.2 GW were new offshore installations [22]. The outbreak has inevitably had a significant impact on electricity consumption, as more people have been encouraged to stay at home. Despite challenging economic environments, financing of new wind farms has seen a record due to a strong 2019 for offshore wind energy [22]. Table 2.1 displays a list of upcoming floating wind projects, with the majority of the activity located in Europe.

Table 2.1: List of upcoming floating wind projects [16].

First power	Country	Project name	Total capacity	Turbine rating	Concept
2021/2022	France	Les éoliennes flottantes de Groix and Belle-Ile	28.5 MW	9.5 MW	Sea Reed
2021/2022	France	Les éoliennes flottantes du Golfe du Lion	30 MW	10 MW	WindFloat
2021/2022	France	EolMed (Gruissan) Pilot Farm	30 MW	10 MW	Damping Pool
2021/2022	France	Provence Grand Large	25.2 MW	8.4 MW	TLP
2021/2022	Japan	Goto City	22 MW	2-5 MW	Hybrid Spar
2021/2022	Norway	Hywind Tampen	88 MW	8 MW	Hywind
2022	Ireland	AFLOWT	6 MW	6 MW	Hexafloat

2.2 Floating platforms and mooring concepts

The fact that a large proportion of the world's wind resources are localized in deep waters, creates challenges for the offshore wind industry. Current technology is mainly based on shallow areas (≤ 30 m). However, by moving wind sites further away from the shore and into deeper waters, the wind force is increased by an increasing wind speed and it will reduce the visual impact. Several different concepts have been developed and are possible solutions for wind turbines. This includes spar, semi-submersible, Tension Leg Platform (TLP), and barge.

2.2.1 Classifications of platforms

In the wind power industry, water depth is separated into three zones: shallow (< 20 m), transitional (between 20 m and 50 m), and deep (> 50 m). Fixed monopile structures are normally used in shallow waters, and at some transitional cites as it is economically suitable [2]. By moving to deeper waters, the material costs increase and other foundations become applicable. These are described in the following, and depicted in Figure 2.1.

- **Spar**: Is cylinder-shaped and moored to the sea bottom with catenary mooring lines. The platform generates stability through ballast weights and has a large buoyancy section near the free surface and a ballast tank closer to the bottom. Due to the large draft, it is more suitable to harsh conditions, making it less vulnerable to wind and surface waves. However, this also requires a large water depth (> 80 m), and assembly in shallow water will therefore not be possible. Its relatively simple substructure construction results in lower costs of fabrication.

- **Semi-Submersible platform**: A semi-submersible platform utilizes a combination of buoyancy and ballast to gain stability. The floating structure is moored to the seabed with catenary mooring lines. It has a flexible design with respect to water depth, however, a quite complex structure results in large amounts of steel. An advantage with such a design is that the draft is small, compared to a SPAR platform, and as a result, it can be assembled onshore and towed to its final position. The WindFloat concept [23] utilizes such a system and has an active ballast system to keep the turbine upright and thus maximize power output.

- **TLP - Tension Leg Platform**: TLP foundations have a high level of buoyancy and consist of cylindrical tendons or tethers moored to the seabed. The tendons are connected directly underneath the floating structure, and tensions in the tendons are critical as a fracture may lead to capsizing. Stability is gained through the tensions in the mooring system. TLP has several advantages, such as a low structural mass and material usage, leading to reduced costs. In the same way as the semi-sub, the platforms can be assembled onshore, however, towing

can normally not be done without extra stabilization to its final position and makes for a complicated installation procedure. Furthermore, high loads on the mooring and anchoring system are a disadvantage and also the least developed concept for wind energy applications.

- **Barge** - A barge platform is mainly stabilized through buoyancy, with a large waterplane area and low drift. This means that the platform is highly susceptible to dynamic motions, being limited in terms of platform pitch-stability, wave sensitivity, and control complexity. Therefore, one option is to use a damping pool technology that optimizes stability and performance. BW Ideol is a company that utilizes such a system, with the possibility of quayside installation [24].

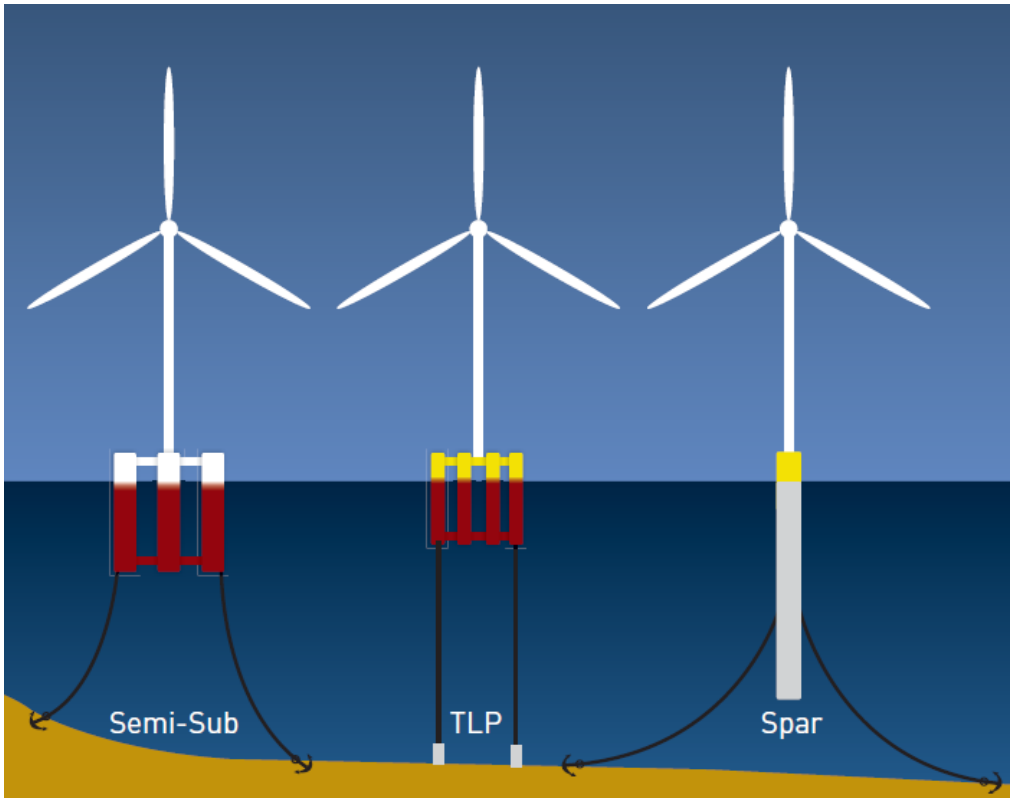

Figure 2.1: Design overview of different floating platforms. Originally from [2].

2.2.2 Mooring concepts

Floating offshore wind industry mainly utilizes three different mooring concepts. These are catenary, taut-line, and tension leg. These methods depend on weather conditions, depth, size of the platform, and costs. The mooring system characteristics have a large impact on the floating structure's static stability and dynamic response to environmental loads [3].

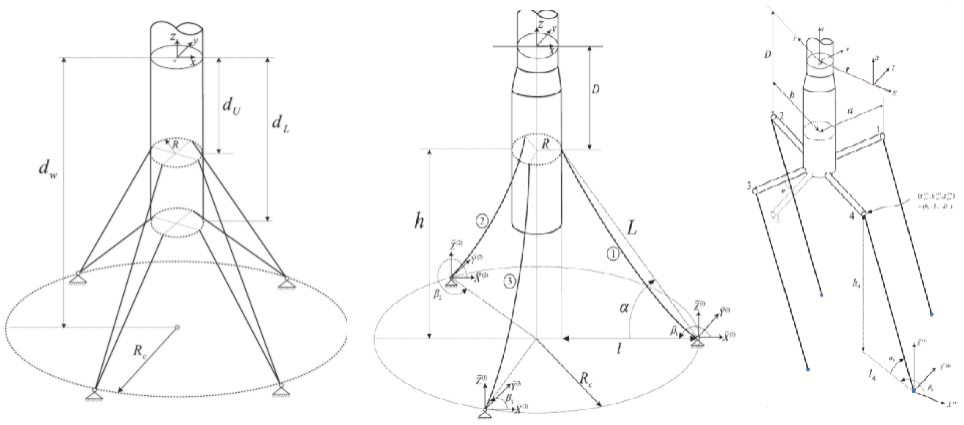

Figure 2.2: Overview of different mooring systems. From left: Taut-leg, catenary and TLP [3].

Catenary mooring systems consist of long chains and steel ropes/wires with the mooring system in a horizontal position at the seabed. Wires are applied to limit the pre-tensioning and reduce costs and chain is used to obtain the catenary effect. The foundation is limited to vertical motion as anchors may be misplaced and the vertical component of the tension is assumed to be zero at the anchor. If the structure moves, the catenary shape changes by changing the tension in the line. Tension is created through the suspended length of the line and the distance from the fairlead and to the anchor. Increased tension acts as stiffness to the motions of the structure, and the angular placement of the lines provides stiffness in all directions. In order to keep the floating structure within its boundary conditions, the mooring system is pre-tensioned. Lower pre-tensioning result in lower maximum tensions in the line but offsets of the boundary condition is higher, hence it has to be tuned appropriately.

In the taut-mooring system, the mooring lines have a linear shape from the anchor to the floating structure. This configuration depends on the axial elasticity of the line to provide the required restoring force to the structure. Compared to a catenary mooring system, it has higher linear stiffness and the attached anchor is exposed to both a vertical and horizontal force. The lines are pre-stressed with an angle between 30° to 45° to the horizontal plane. Figure 2.2 shows that the taut mooring system occupies a reduced area compared to the catenary system, mainly due to the catenary shape.

A tension leg mooring system is vertically moored as seen in Figure 2.2, by vertical tendons or tethers withstanding large tensile loads. These are anchored by suction piles, driven piles, or a template foundation [25]. Platforms moored with this type of configuration are favorable in deep waters ($>$ 300 m). The buoyancy is achieved through submerged pontoons whose displacement exceeds the structure's total gravity or deadweight loading. The tethers are extensions from the

columns and moored to foundations on the seabed, keeping the floating structure in position during all weather conditions.

2.2.3 Mooring stiffness characteristics

The dynamic response of the floating structure can be optimized by using mooring lines and its mean position varies for different mooring line pre-tensions. Tension in the fairleads must be incorporated and taken into account in the platform's structural design. Therefore, it is essential to determine the effect of the mooring line pre-tension as this will aid in an optimal pre-tension level, as well as motion response. As the mooring line achieves a catenary shape and the anchor is subjected to horizontal forces only, the pre-tension is referred to as the horizontal holding capacity, dependent on the horizontal distance from the fairlead to the anchor.

The stiffness in the mooring lines provides a restoring force. For a floating structure, the restoring forces in heave, roll, and the pitch comes from hydrostatic and mass considerations. For an un-moored system, there exists no stiffness in surge, yaw, and sway, since there are no constraints against these motions. However, by utilizing mooring lines, these constraints become induced. The stiffness controls the mean offset of the vessel, thus influencing the low-frequency motion [4]. Two basic principles provide restoring force of a moored system, shown in Figure 2.3:

- Geometric stiffness
- Elastic stiffness

Geometric stiffness is provided through a change of tension due to a change in mooring line geometry. Contrary to geometric stiffness, elastic stiffness is mostly relevant for taut moored systems with fiber ropes. In this case, the stiffness is provided by axial elongation of the line, thus it is a measurement of the fiber rope's ability to resist elongation.

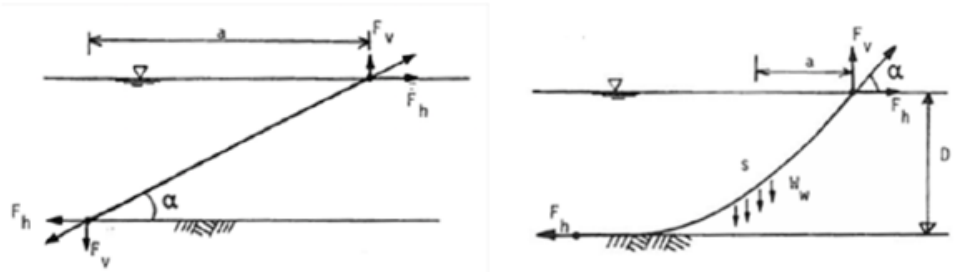

Figure 2.3: Mooring line stiffness characteristics, elastic stiffness (left) and geometric stiffness (right) [4].

2.3 Mean tension in mooring lines

2.3.1 Mooring chain structure and material grading

Mooring chains are normally manufactured out of hot rolled low alloy carbon steel composed of a series of interconnected links (see Figure 2.4). The figure also marks (red dots) the two locations where fatigue failure is most likely to occur under tensile loading [26]. Thus, the two points denote the regions where the highest principal stresses occur. The most likely fatigue crack propagation direction is horizontally in point (2), known as the crown, and vertically in the material at point (1) named the bend. The inner part of the weld is also a hot spot of the studless chain link.

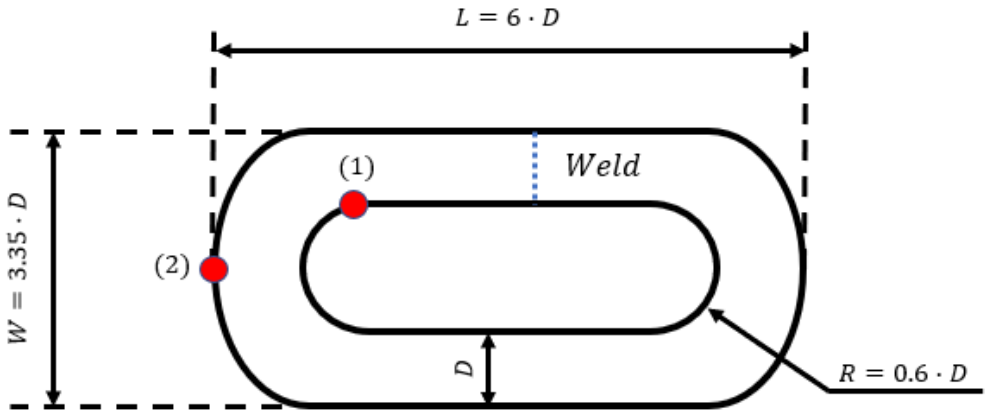

Figure 2.4: Nominal dimensions of a chain link.

The manufacturing process of mooring chains is comprised of several steps. This includes cutting the length of the chain link out of a bar and hot bending, which allows the material shape to be altered to the exact chain specifications. Further, a flash butt welding process of the extremities is performed, in which the energy transfer is provided by resistance heat in the parts being welded. Then, a heat treatment stage is performed composed of quenching in water, followed by heating and cooling. Finally, the chain undergoes an operation of proof loading, where it is subjected to a specified amount of load depending on the chain grade [27]. According to [26], the Minimum Breaking Load (MBL) is defined as the minimum load that a chain segment of at least three chain links must withstand during 30 seconds without fracturing. The imposed mean loading is referred to as a percentage of the MBL.

Chains are graded after their yield strength of the steel and are classified into six different categories: R3, R3S, R4, R4S, R5, and R6 [27]. Fatigue life tests on different grades of mooring chains have shown three times longer lifetime for category R4 and R5, compared to grade R3 [1]. Tests from previous years were performed at 20 % MBL, while recent tests were executed at 7-15 % with

a resulting mean at 11 %. The result yielded a strong identification of mean tension playing an important part and has further been undermined by the research of Zhang [28] and Martinez [29]. Moreover, the influence of mean tension has been quantified with the help of correction functions such as SWT's model, proposed as a superior model to account for the mean stress effect on fatigue life [1, 30].

2.3.2 Fatigue life in mooring lines

Fatigue is the creation and growth of cracks during dynamic loading and is an important design criterion for mooring lines. Mooring systems maintain a dynamic floating structure within their predefined geographical area, with a specified tolerance. Historically, mooring systems have been of great importance within the oil and gas industry. In recent years it has also seen a rise in the renewable energy sector. For both industries, a failure in mooring lines could be devastating, leading to large accidents and have an environmental impact [26]. During 2010-2013 a total of 15 reported failures with mooring lines occurred on the Norwegian continental shelf and were caused by a mixture of overload, fatigue failure, and mechanical damage [31]. A large amount of incidents necessitates an improvement of the guidelines and standards and actualizes the need of studying the factors affecting fatigue life in mooring lines.

S-N curves for mooring lines are based on tests performed with a single mean tension and are assumed to be 20 % of the chains MBL. The curves are further used to calculate the damage to all tension cycles independent of their mean values. Moreover, today's method of calculation only takes into account the tension amplitude independent of the related mean tension for all cycles. Since the fatigue response of floating units occurs at varying mean tensions, and different sea states influence the mean tensions, it is necessary to understand its dependence on fatigue life [1].

The research found that the influence of mean tension in mooring lines may contribute more than expected to fatigue failure and that the fatigue capacity increases significantly in chains when being cyclically loaded with a reduced mean tension [1]. Many tests have been completed in full scale focusing on the influence of mean tension, and results have shown that fatigue life is highly dependent on mean tension [1, 28, 32]. For systems operating at lower mean tensions than 20 % MBL, this results in unnecessary costs and maintenance being performed at a too early stage. Meanwhile, systems with loadings higher than 20 % MBL will operate at unacceptable levels and reduce the fatigue life.

3 Environmental Conditions and Environmental Loads

A complete description of the environmental conditions and environmental loads is necessary when predicting and analyzing loads acting on floating structures. The following conditions are considered in this thesis:

- Wind
- Wave
- Current

Environmental conditions are natural phenomena and occur as a stochastic character. It contributes to structural damage and operational disturbance. Therefore it is important to understand these processes. An overview of environmental loads a FOWT is subjected to is given in Figure 3.1.

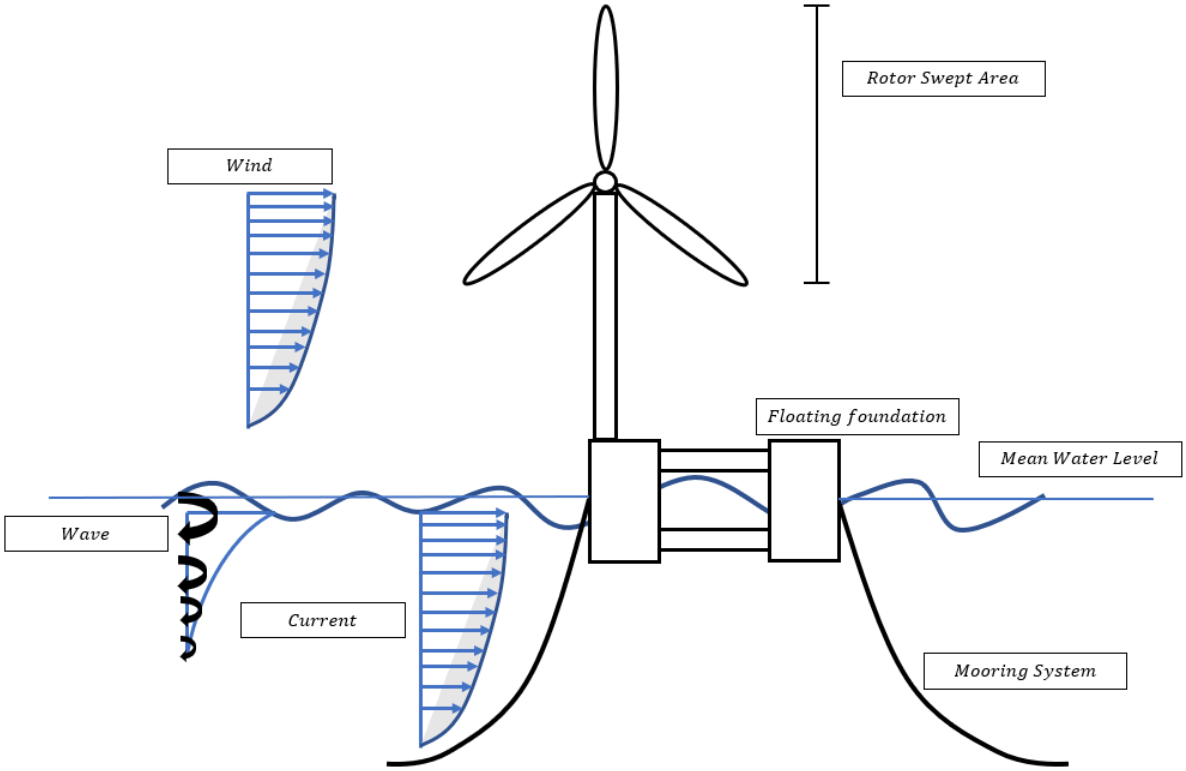

Figure 3.1: Environmental loads acting on a floating structure.

3.1 Stochastic modeling

The environmental phenomena of wind and waves are usually described by variables of statistical nature. The typical engineering approach is to unveil all possible outcomes by describing these variations in short- and long-term distributions.

3.1.1 Short-term distribution

Wind and waves are random of nature and must be described by their stochastic characters. This means that the processes are functions of the time lead by a certain related probability. Short term variations are based on two assumptions:

- Stationarity: The variables are not affected by the time at which the time series is observed. This means the variations are time-invariant.
- Ergodicity: The measured variables reflect a typical behaviour of all other possibilities of the measurements. More specifically, any random sample from a stochastic process must have the ability to represent the average statistical properties of the entire process.

Thus, seasonality is very likely for wind and waves, so stationarity is fulfilled only for a few hours [9]. Two important parameters of short-term distributions are the significant wave height, Hs, and peak wave period, Tp. For time-domain simulations, these statistical parameters are obtained by an evaluation of energy density spectra, describing the amplitudes and frequency content of the variations [33]. Relevant wave spectra that characterize short-term stationary irregular sea states is a modified Pierson-Moskowitz spectrum, referred to as the JONSWAP spectrum.

Short-term wind speed variations usually mean fluctuations around the mean wind speed, known as turbulence and gusts. These fluctuations occur in three separate directions: longitudinal, lateral, and vertical [5]. To represent short-term wind speed variations, spatial turbulence models are frequently used. This includes the Mann turbulence model and the Kaimal spectrum. Within a turbulent wind field, several discrete events occur throughout a short period. The total wind speed will, as a result, be determined by the mean wind speed, $\bar{U}$, and the turbulence or gust:

$$U(x, y, z, t) = \bar{U}(z) + u(x, y, z, t) \tag{3.1}$$

The total wind speed is illustrated in Figure 3.2, where the gust is characterized and affected by: a) amplitude, b) rise time, c) maximum gust variation and d) lapse time.

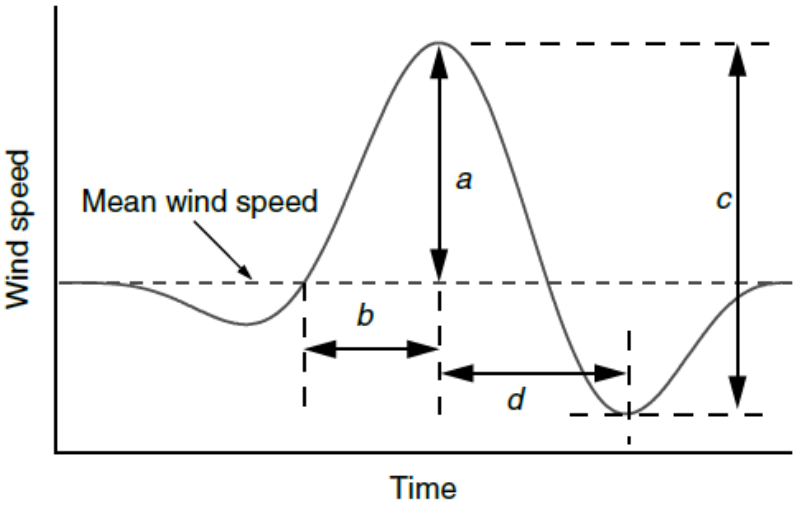

Figure 3.2: Total wind speed, originally from [5].

3.1.2 Long-term distribution

A long-term distribution defines extreme value statistics of environmental parameters during 20-100 years. Contrary to short-term distribution, the long-term distribution deals with the occurrence of extreme events, such as storms. In the design phase of offshore structures, a long-term distribution is preferred due to its likeliness of including irregular wind and wave behavior. However, the design life of the structure must first be established with consideration of two storm types that the structure will encounter during its lifetime. The first being a locally generated storm with wind and wind-generated waves. Secondly, it is a distant storm appearing as swells, generally being low-frequency waves. The local storm is described by return periods, defined as the average interval of time (years), in which a certain condition is exceeded.

The given condition for a return period is associated with a level of probability [9]. The availability of long-term information regarding wind and waves is scarce, due to difficulties in tracking the required measurements over several years. This gives rise to different probability functions describing the long-term distributions, i.e. Gumbel's standard skewed distribution or Weibull distribution.

Long-term wind speed variations are characterized by the variation of horizontal wind speed to the height above the sea surface. For engineering purposes, it comes with great importance to determine the variability of wind speed with elevation, namely the vertical wind shear profile [5]. These profiles may be found in standards, i.e. [34].

3.2 Wind conditions

The available energy in wind is a result of the kinetic energy of large amounts of air moving across the earth's surface. Wind turbine blades receive this kinetic energy and convert it to mechanical or electrical energy [35]. Wind speed varies with time and height above the surface. However, winds blow predominantly in a horizontal direction, corresponding to horizontal pressure gradients in the atmosphere. The power output, P from a wind turbine is given by:

$$P = \frac{1}{2} C_p \rho A U^3 \tag{3.2}$$

where ρ is the density of air, C_p is the power coefficient, A is the rotor swept area and U is the wind speed.

3.2.1 Variations in mean wind speed

The availability of wind varies greatly, both geographically and in space and time. Throughout the world, different climate regions exist, some windier than others. In a given region the wind speed may vary from year to year, and even larger variations can occur each decade. These long-term variations can complicate precise predictions of economic models to future wind parks. When the time range is shorter than a year, the seasonal variations are more predictable. To represent the variation in mean wind speed with respect to the height above sea surface for averaging times, such as 1 minute, 10 minutes, or 1 hour, an idealized wind profile can be utilized [36].

$$u(z) = u(z_0) \left(\frac{z}{z_0} \right)^{\alpha} \tag{3.3}$$

where $u(z_0)$ is the mean speed at the reference height above the sea surface, z is the height variable and $\alpha = 0,14$ and is a height exponent [37] based on the "Wind Power Law", which is a good approximation for wind profiles in boundary layers for a neutral atmosphere [38].

The wind speed is continuously changing, and to predict the production capacity of a wind turbine, it becomes necessary to understand when the wind is powerful. Normally, wind speed is measured with an anemometer and the mean speed is measured every 10 minutes at a specific height above the surface, as mentioned above. A Weibull distribution can be utilized to describe the cumulative probability density function for a random mean speed as:

$$F(u) = 1 - \exp\left[-\frac{u - \alpha^{\gamma}}{\beta} \right] \tag{3.4}$$

where β is the Weibull scale parameter and is a measure for the characteristic wind speed of the distribution. γ denotes the Weibull form parameter and specifies the shape of the distribution. Smaller

numbers for γ are the result of significantly variable winds. Lastly, α describes the localization and the probability of a velocity to occur.

3.2.2 Turbulence

Turbulence is described as fluctuations in wind speed as a function of time and space, and are generated based on two circumstances [20]:

- Friction with the earth's surface - Flow disturbances caused by topographical features
- Thermal effects - Masses of air moving vertically as a result of variations of temperature and hence density of air.

Often, these two aspects are strongly correlated, for instance when masses of air move across a mountain and are forced upwards into cooler regions where thermal equilibrium does not exist. Other factors that influence the phenomena of turbulence are temperature, pressure, density, and humidity. As it is quite complex, an appropriate method to describe it is to use statistical models.

Turbulence Intensity

Turbulence intensity is one factor characterizing the statistical variability in wind. Turbulence intensity decreases when the distance to the surface increases and is defined as:

$$I = \frac{\sigma}{\bar{U}} \tag{3.5}$$

where σ is the standard deviation to wind speed variations divided by the mean wind speed, usually defined over a 10 minute period or hour. In certain cases, no information regarding the standard deviation of the wind exists. For that matter, wind turbine classes are introduced and are defined in terms of wind speed and turbulence parameters. However, this will not give a precise representation of a specific site, but rather give insurance that the wind conditions are equal or less severe than the ones that define the class itself [39].

3.2.3 Wind spectrum

A stochastic process can be expressed as a spectrum, and the wind spectrum used in this thesis describes the variation of wind speed over a certain period. The wind spectrum or the turbulence spectrum describes the frequency distribution in the wind speed variations and how the turbulence energy is distributed as a function of the frequency. Wind spectrum models and turbulence intensity curves for Kaimal wind spectra recommended by the International Electrotechnical Commission (IEC) are divided into different classes based on their intensities for a mean wind speed. For FOWT

they recommend specific turbulence intensity data for the given area [40]. However, in many cases turbulence intensity data do not exist, hence IEC 61400-1 [34] Wind Turbine Classes are proposed to obtain a turbulence intensity reference value. The values do not represent a specific site, but rather guarantee that a design class may be installed on sites with wind conditions equal or less severe to the ones that define the specific class itself [39].

Spectral wind models can be utilized in order to determine the energy distribution of wind as a function of frequency. Fatigue life is a highly critical aspect for FOWT, and they are very sensitive to wind loads. The Kaimal wind spectrum is one of the most widespread models in the offshore wind industry and is given as:

$$\frac{fS_k(f)}{\sigma_k^2} = \frac{\frac{4fL_k}{V_{hub}}}{\left(1 + \frac{6fL_k}{V_{hub}}\right)^{\frac{5}{3}}} \tag{3.6}$$

where f is the frequency, k denotes indices of the components of wind velocities in the longitudinal, lateral and vertical direction. S_k is the single-sided velocity component spectrum, σ_k is the velocity component standard deviation and L_k is the velocity component integral scale parameter.

For offshore locations, the Frøya wind spectrum, originally developed for the Norwegian Sea, is recommended by DNVGL-RP-C205 [37].

$$U(T,z) = U_0 \cdot \left\{1 + C \cdot ln\frac{z}{H}\right\} \cdot \left\{1 - 0.41 \cdot I_U(z) \cdot ln\frac{T}{T_0}\right\} \tag{3.7}$$

where $H = 10$ m, $T_0 = 1$ hour and the averaging period $T < T_0$ at a height z above sea level. The Frøya model further implies that the mean wind speed, U_0, at a height H above sea level corresponds to extreme mean wind speeds with specified return periods of approximately 50 years [37]. The coefficient C depends on the mean wind speed:

$$C = 5.73 \cdot 10^{-2} \cdot \sqrt{1 + 0.148 \cdot U_0} \tag{3.8}$$

and I_U is given as:

$$I_U = 0.06 \cdot (1 + 0.043 \cdot U_0) \cdot \left(\frac{z}{H}\right)^{-0.22} \tag{3.9}$$

In Figure 3.3 the Frøya wind spectrum (API) is plotted against the Kaimal spectrum (IEC). The Frøya spectrum has higher energy in the low-frequency range compared to the Kaimal spectrum, and also includes a gust factor that allows for the conversion of mean wind speeds between different averaging periods.

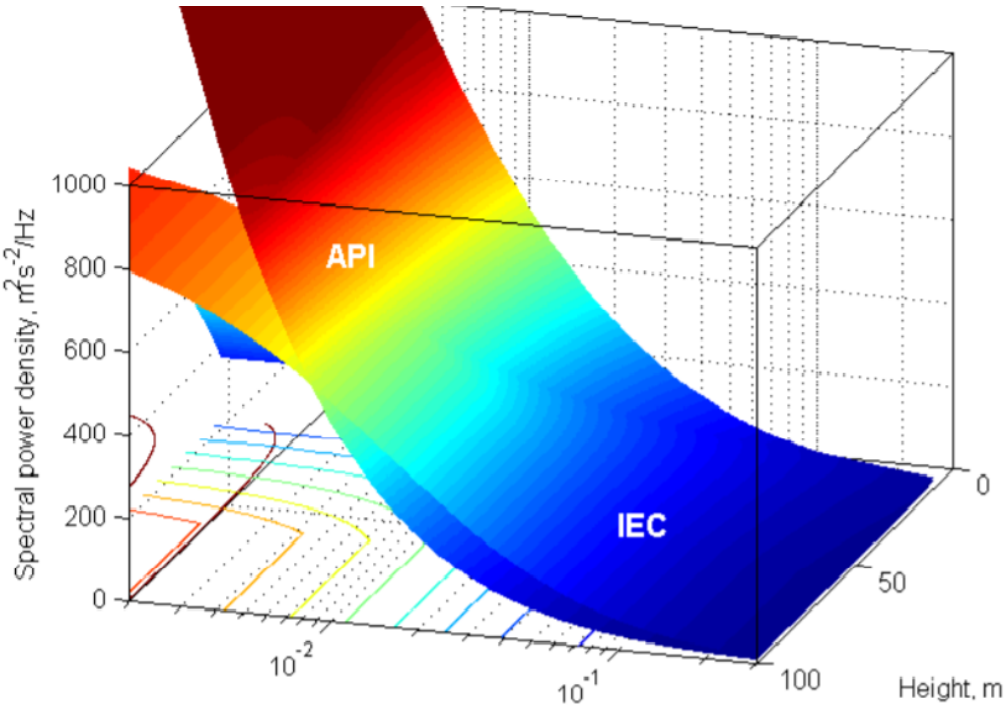

Figure 3.3: Frøya wind spectrum plotted together with the Kaimal spectrum [6].

3.2.4 Aerodynamic loads

Aerodynamic loads acting on the rotor blades of a wind turbine are determined by incoming wind velocity and the induced velocity due to the presence of the rotor. The airfoil shape of the wind turbine blade creates lift by pressure difference on the upper relative to the lower side. The combination of mean wind and turbulent fluctuations then develop mechanical power, in the form of torque. The kinetic energy in the wind is then converted to electrical energy. The lift force, L, is primarily generated as a consequence of the pressure difference on the airfoil surfaces and is perpendicular to the direction of the relative velocity of the incoming wind, U_{rel}. The drag force D, however, is parallel to the direction of the oncoming airflow.

To obtain dynamic responses of wind turbine blades, a blade element momentum (BEM) method is widely used in engineering practice, in combination with a structural analysis tool. The BEM is based on the assumption that the force of the blades is the only contribution to an overall change in linear momentum over the rotor [7]. This means that the angular momentum is not considered, despite the rotation of the turbine blades, wakes, and vortices appearing in the airstream. Furthermore, for a wind turbine, the axial thrust produces an overturning torque, resisted by the platform foundation and mooring lines. Thus, by modeling the rotor as an actuator disc in streamlined flow,

the thrust can be expressed by momentum theory:

$$dT = 2\rho A_d U_\infty^2 a(1-a) \tag{3.10}$$

For an incremental section of the rotor with actuator disc area $A_d = 2\pi r dr$, a denotes the axial induction factor defined as the fractional wind speed decrease at the turbine, as is a function of r [41]. The aerodynamic loads exerted on the blades can be expressed as:

$$\begin{aligned} dL &= \frac{1}{2} C_L \rho c U_{rel}^2 \\ dD &= \frac{1}{2} C_D \rho c U_{rel}^2 \\ dM &= \frac{1}{2} C_M \rho A_d c U_{rel}^2 \end{aligned} \tag{3.11}$$

where $U_{rel}^2 = (U_\infty \cdot (1-a))^2 + (\Omega r \cdot (1-a))^2$, in which Ωr denotes the apparent rotational speed at the blade section, c is the chord length, C_L, C_D and C_M is the lift, drag and pitching moment coefficients, respectively. The aerodynamic forces acting on the airfoil is shown in Figure 3.4, together with the velocities.

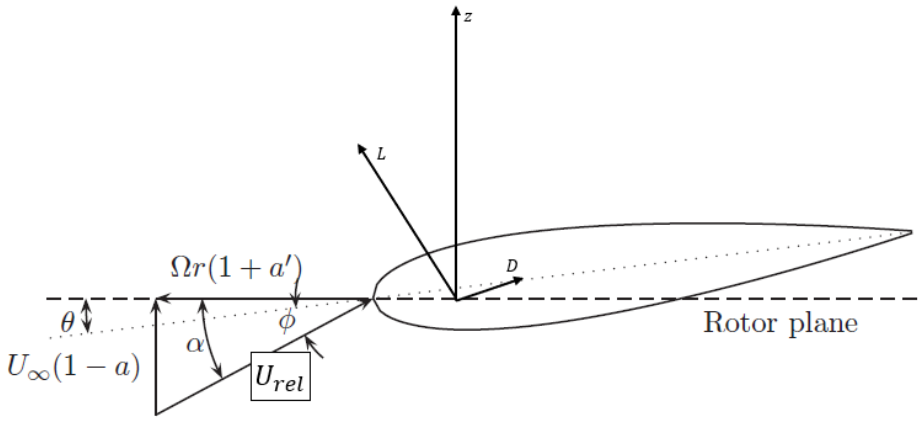

Figure 3.4: Resulting forces on a wind turbine airfoil, originally from [7].

Typically, the lift coefficient increases with an increasing angle of attack for low values of α and reaches a peak angle at some point. A further increase in the angle results in a decrease of the lift coefficient, also known as the stall limit. The reason is the suction at the upper area of the airfoil drops as a result of flow separation at higher angles of attack [7].

3.3 Wave conditions

Waves are described as irregular and have a random shape, height, length, and velocity. It is created due to disturbances propagating in different directions. Further, a sea state is a condition of an oceanic surface described as a simplified wave model. Considering structural design purposes, wave conditions may be described by stochastic methods applying wave spectra [37] and are described in the following.

3.3.1 Wave spectrum

Irregular waves are described by several small linear wave components with different amplitude, frequency, phase, and direction [37]. To understand the wave phenomena, mathematical modeling is necessary, and in the same way as wind, the short-term wave conditions can be described with stochastic models utilizing wave spectra. The wave spectra are limited to a period of 30 minutes to 10 hours and contain parameters such as significant wave height Hs, peak wave period Tp, and shape factors. Many wave spectra exist, however, these are often only suitable for certain areas. The Pierson-Moskowitz and JONSWAP wave spectra are two widely used models within the offshore wind industry.

The Pierson-Moskowitz (PM) wave spectrum describes a fully developed sea state in which the wind blows over a large area at a constant speed and direction for several hours, and is given as:

$$S_{PM}(\omega) = \frac{5}{16} \cdot H_S^2 \, \omega_p^4 \cdot \omega^{-5} \exp\left(-\frac{5}{4}\left(\frac{\omega}{\omega_p}\right)^{-4}\right) \tag{3.12}$$

where $\omega_p = \frac{2\pi}{T_p}$ is the peak wave angular frequency and depends on the peak wave period T_p. H_S is the significant wave height and ω is the wave frequency [9]. In reality, waves do not exist in a fully developed state over a larger area, so the JONSWAP spectrum was introduced as a modified model of the PM:

$$S_J(\omega) = A_\gamma \; S_{PM}(\omega) \; \gamma^{exp\left(-0.5\left(\frac{\omega-\omega_p}{\sigma \; \omega_p}\right)^2\right)} \tag{3.13}$$

where γ represents a dimensionless peak enhancement parameter, A_γ is a normalization factor and σ is the spectral width parameter given as:

$$\sigma = \begin{cases} 0.07, \text{ for } \omega \leq \omega_p \\ 0.09, \text{ for } \omega > \omega_p \end{cases} \tag{3.14}$$

The additional peak in the JONSWAP spectrum is derived from γ when $\omega = \omega_p$ as it converges to 1 for small and large frequencies away from ω_p [8]. By increasing the value of γ, the JONSWAP spectrum experiences a more peaked shape, as seen in figure 3.5.

A spectral analysis of the JONSWAP spectrum would show different characteristics with individual waves, and an investigation of the response spectrum is a key tool for monitoring dynamic phenomena. To identify hidden periodicities and dominant cyclical behavior in a highly noisy signal, such as fairlead tension and its first-order wave excitation, a periodogram is proposed as a reliable source [42]. This is due to a limited observation time in the data, it is biased, and shows a high variance, which does not decrease by an increase of the observation time.

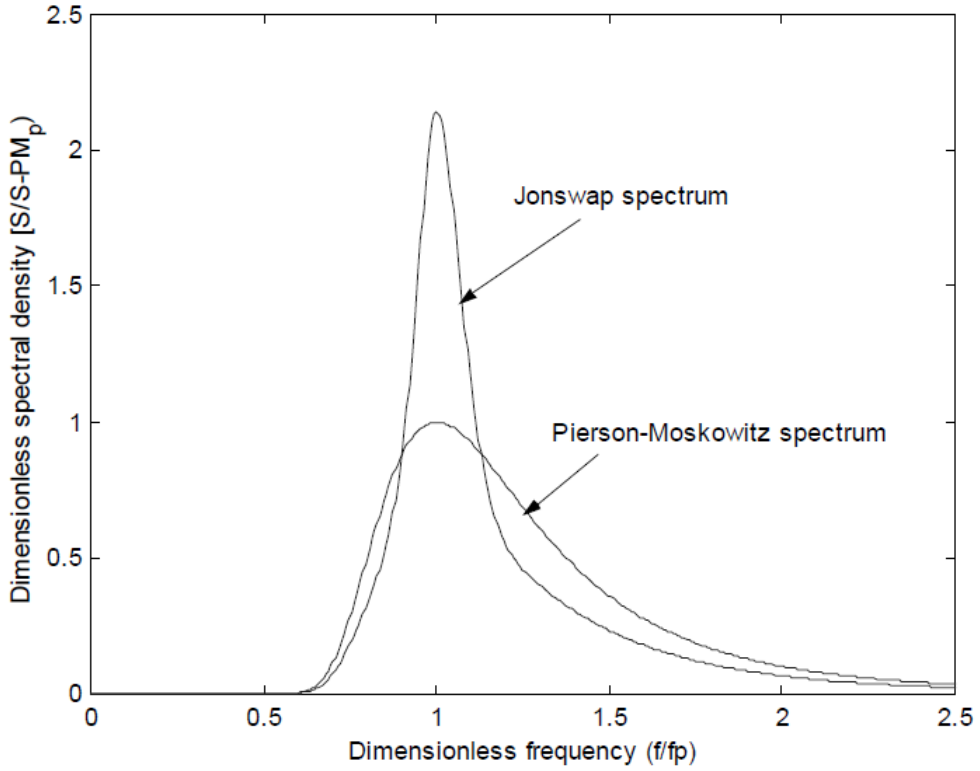

Figure 3.5: JONSWAP plotted against the Pierson-Moskowitz spectrum [8].

3.3.2 Hydrodynamic forces

Considering a floating structure forced to carry out harmonic motion being exposed to incompressible, inviscid, and irrotational fluids, two theories normally apply [43]. These are known as Morison's formula and potential flow theory. Morison's equation applies to slender structures, such as mooring lines. When the wavelength to diameter ratio is significantly large ($\lambda > 5D$) and non-linear viscous effects are negligible, the potential flow theory approaches the semi-empirical Morison's solution [33]. The Morison's formula is given in Equation (3.15) [44]:

- **Froude-Krylov force** - The force that acts on the body as if it were transparent to the wave motion. It can be described as a non-viscous drag force.

- **Viscous drag force** - The presence of a wake region downstream of the component. The wake region creates a low-pressure region and thus a pressure differential between upstream and downstream. The pressure differential causes a force to be exerted in the direction of the water particle velocity.

$$dF = \underbrace{\rho C_M A dz\ a}_{\text{Froude-Krylov}} + \underbrace{\frac{\rho}{2} C_D D dz |u - \dot{x}|(u - \dot{x})}_{\text{Viscous drag force}} - \rho A dz (C_M - 1)\ddot{x} \tag{3.15}$$

The forces are combined in Equation (3.15), expressing axial, lateral or transverse forces per unit length on slender structures The coefficients are described as:

- dF: Resultant force exerted on a cylindrical element.
- ρ: Fluid density.
- A: Cylinder area.
- dz: Incremental segment of the cylinder.
- a: Undistributed fluid acceleration at the midpoint of the cylinder.
- u: Undistributed fluid velocity at the midpoint of the cylinder.
- C_M: Hydrodynamic added inertia coefficient.
- C_D: Non-dimensional drag coefficient.
- $\ddot{x}, \dot{x}$: Acceleration and motion term of the cylinder.

Since the water particle motion during waves is oscillatory within a wave period, the downstream side of the cylinder reverses every half cycle, thus the pressure differential in Figure 3.6 causes a force to be exerted in the direction of the wave [9].

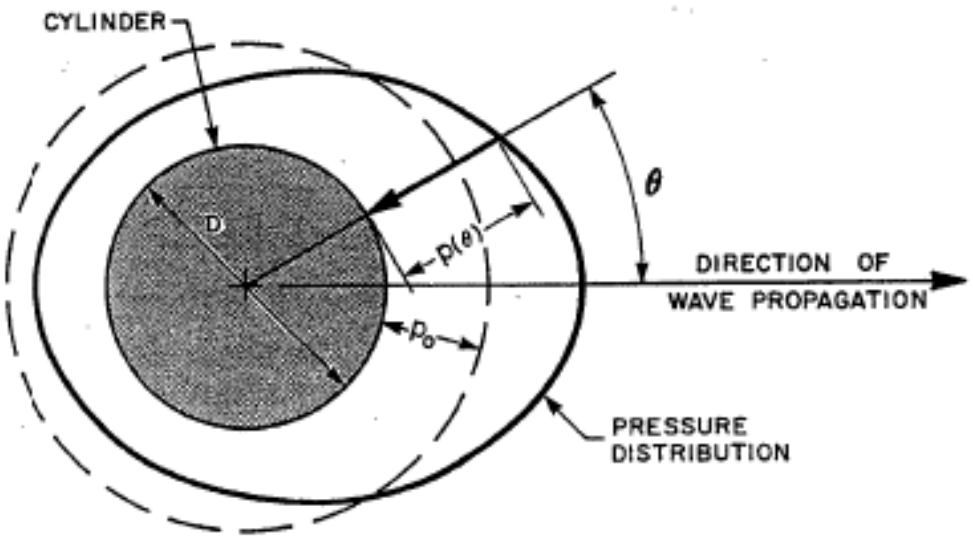

Figure 3.6: Example of a pressure distribution about a cylinder in waves [9].

Potential flow theory refers to a solution of the velocity potential used to characterize the flow with the viscous effects being confined within a linearized boundary layer for. The wave forces are found by pressure integration around a rigid body [33]. In order to use potential flow theory, the fluid must satisfy Laplace's equation:

$$\nabla^2\phi = \frac{\partial^2\phi}{\partial x^2} + \frac{\partial^2\phi}{\partial y^2} + \frac{\partial^2\phi}{\partial z^2} = 0 \tag{3.16}$$

where ϕ is the first order total velocity potential function. The potential flow equation approaches the simplified Morison's equation for cylindrical structural members when viscous effects are negligible and structures are large compared to the wave length [9]:

$$F^{wave} = F^{FK} + F^{Diff} \tag{3.17}$$

where the expression still contains the Froude-Krylov term from equation (3.15) and a diffraction component, F^{Diff}, accounting for wave propagation disturbances due to the presence of a structural body.

3.3.3 Wave kinematics

A simplified version of linearized wave theory is known as the Airy theory or sinusoidal wave theory, most commonly used for coupled analysis. It assumes that the wave height, H, is significantly smaller than the wavelength, λ, or the water depth, d, as well as the irrotational flow of an inviscid incompressible fluid. The Airy theory further assumes that the waves can be expressed according to the velocity potential function in Equation (3.16), where free surface conditions are satisfied at

MWL, rather than at the oscillating wave surface. The free surface water conditions come from the boundary value problem and may be summarized by three parts: a bottom boundary condition, free surface kinematic, and dynamic condition [9]. Further, the dispersion relationship between the wave period and the wavelength, in terms of angular frequency becomes [37]:

$$\omega = [gk \cdot \tanh kd]^{1/2} \tag{3.18}$$

By combining the free surface boundary condition and the linear dispersion, the velocity potential may be expressed as:

$$\phi = \frac{gH}{2\omega} \cdot \frac{\cosh k(y+d)}{\cosh kd} \sin\Theta \tag{3.19}$$

where $\Theta = k(x\cos\beta + y\sin\beta) - \omega t$ describes the phase and β is the direction of propagation, k refers to the wave number given as $k = 2\pi/\lambda$ and ω is the wave frequency. Moreover, application of equation (3.19) may be used to describe both the water particle velocity and acceleration, respectively, in horizontal and vertical direction.

3.4 Current

To describe the movement of water from one location to another, an oceanic current is introduced and should be considered for the design of mooring lines. Current is mainly driven by three factors [45]:

- Tide: Tidal currents change in regular patterns and create currents in the oceans.
- Wind: Wind drives current and circulates the water and is a strong factor near the ocean surface.
- Thermohaline circulation: Density differences in the water due to temperature and salinity variations occur at all ocean levels.

The current load data applied in this thesis is acquired from [39] and utilizes the surface current direction and speed characterization. The raw data ranges from 2003 to 2015 and some extremities occur, which before to characterization of current climate uses an averaging method. The current velocity varies with water depth, and closer to the water surface, the velocity is greater compared to deeper water. Due to the lack of exact measurements of current speed at different water depths, DNVGL-RP-C205 [37] recommends current speed profiles represented by a linear profile or a Potential profile. The result of the total current speed is comprised of wind- and tide component and their respective profiles are given as:

$$v_{c,wind}(z) = v_{c,wind}(0) \cdot \left(\frac{d_0 + z}{d_0}\right), \ for - d_0 \leq z \leq 0 \tag{3.20}$$

$$v_{c,tide}(z) = v_{c,tide}(0) \cdot \left(\frac{d + z}{d}\right)^{\alpha}, \ for \ z \leq 0 \tag{3.21}$$

$$v_c(z) = v_{c,wind}(z) + v_{c,tide}(z) \tag{3.22}$$

where $v_c(z)$ denotes the resulting current velocity, z is the total distance from still water level, d is the water depth to still water level and d_0 is the reference water depth for wind generating current, taken as half of the water depth at the Gulf of Maine, hence $d_0 = 75$ m [39]. The exponent α correlates to the 1/7 power-law, and a value of 0.14 has proven a good approximation for profiles in the neutral boundary layer, assuming unidirectional current [38]. As the power law index depends on various roughness characteristics and atmospheric stability, the exponent is replaced by a value of 0.11 for extreme wind conditions (ULS).

3.5 Response to environmental loads

The dynamic response of a FOWT can be investigated through turbulent wind and irregular wave conditions. As environmental loads act on a floating platform, they result in a structural response.

3.5.1 Equation of motion

The structural response of the floating platform is comprised of a global motion response (surge, sway, heave, roll, pitch, and yaw). The wind loads acting on the tower and nacelle are mainly considered as drag forces, while loads acting on the turbine blades both contain lift and drag forces. For hydrodynamic loads, Morison's equation can be used to calculate hydrodynamic loads on slender structures, such as mooring lines, while potential flow theory is applicable for large volume structures. The linear equation of motion for a semi-submersible platform with six degrees of freedom (DOF) and external forces can be described in the frequency domain. This differs from a time-domain analysis as non-linearities are replaced by linear approximations.

The motions of a floating structure can be divided into six DOF when subjected to waves, as seen in Figure 3.7. The motions along the translatory rigid-body DOF are referred to as sway, surge, and heave, while angular as roll, pitch and yaw and are used to specify the position and orientation of floating structures [44]. Each degree of motion is associated with an added mass term and a damping term.

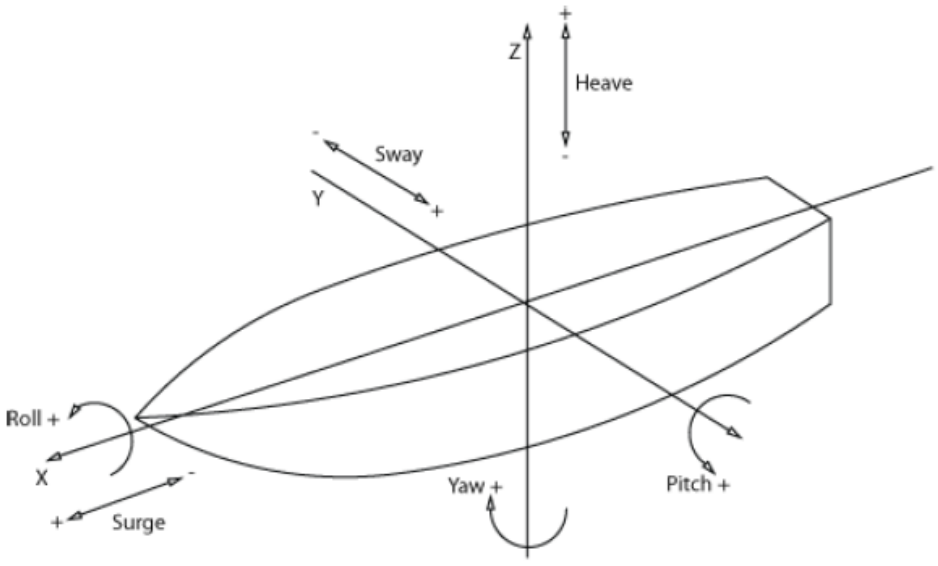

Figure 3.7: Definition of rigid-body motion, originally from [10].

In the frequency domain, the equation of motion is described as a 2nd order linear differential equation. The forces represent an external force vector, such as waves, mooring, or other, and is expressed as:

$$(M + A(\omega))\ddot{x}(\omega) + B(\omega)\dot{x}(\omega) + Cx(\omega) = F(\omega) \tag{3.23}$$

where ω is the angular frequency, M is a mass matrix of the rigid-body obtained from the platform, A is the added hydrodynamic mass matrix, B is the hydrodynamic damping matrix, C is a stiffness matrix, and $x(\omega)$ is the structural motion vector with its respective time derivations $\ddot{x}(\omega)$, $\dot{x}(\omega)$. However, as the semi-submersible platform used in this thesis is modeled as a SIMO body and based on non-linear time-domain analysis, an impulse-response function is introduced into Equation (3.23), which accounts for frequency-dependent added mass and linear radiation damping in time domain [33]:

$$(M + A_\infty)\ddot{x} + D_1\dot{x} + Kx + \int_0^t h(t-\tau)\dot{x}(\tau)d\tau = q(t, x, \dot{x}) \tag{3.24}$$

The linear external damping matrix is denoted as D_1, K is the hydrostatic restoring matrix, h is a matrix of retardation functions, thoroughly described in [46]. Lastly, the term q is a vector with external loads or a excitation load matrix, given as:

$$q = -mg\hat{k} \cdot r_g + \rho g V \hat{k} \cdot r_b + q_{1st} + q_{visc} + q_{FE} \tag{3.25}$$

where r_g and r_b represents position vectors from CoG and buoyancy to the origin. The first term, q_{1st} is a vector with 1st order wave loads, q_{visc} describes viscous contributions from columns and pontoons by a quadratic term of Morison's equation, and finally, q_{FE} is the loads imposed on the platform by the mooring system and tower base.

3.5.2 Excitation forces

The motions of a moored floating platform can be separated into static and dynamic contributions. Static motion is a result of mean forces acting on a vessel, providing a mean offset, whereas dynamic motion is the wave- high- and low-frequency motions. Mooring lines are influenced by wind forces and current, contributing to the static forces and a static tension that leads to the vessel having a mean offset [4]. Moreover, the total dynamic response can be differentiated into:

- Low frequency (LF): Wind frequency motions, including resonant wind-induced LF motions and second-order wave-induced resonant motion (not relevant for this thesis).
- Wave frequency (WF): Response to wave loads.
- High frequency (HF): Second order wave resonant response and resonant rotor frequencies.

As the LF resonant motion is sensitive to damping, the LF component of the line tension will be largely influenced by damping as well. Damping of LF motions relevant for this FOWT is drag forces on mooring lines, viscous loads on the hull, aerodynamic damping due to the rotor, variation of wind loads with the velocity of the structure, and friction of the mooring lines on the seabed [47]. The viscous loads used in this thesis, come from Morison drag coefficients and contributions from linear potential damping.

4 Fatigue of Mooring Chains

A brief overview of relevant topics related to fatigue in mooring chains is provided in this chapter. That is S-N curves, mean tension and stress correction methods, and a review of their effects on fatigue life of offshore mooring chains.

4.1 Mooring chain fatigue damage

Fatigue damage is defined as a change that occurs in a material that is subjected to a periodic variable load. The fatigue life commonly consists of three phases: crack initiation, crack propagation, and a final fracture. The fatigue life ends by the final fracture and occurs during the last up-loading tensile load cycle [48].

4.1.1 S-N curves

The fatigue capacity is expressed by a S-N curve or diagram, also named Wöhler curves, with logarithmic axis, given as:

$$n_c(s) = a_D \; s^{-m} \tag{4.1}$$

where $n_c(s)$ denotes the number of stress cycles, s is the stress range, a_D is the intercept parameter of the S-N curve and m is a slope parameter. For a studless chain the fatigue curve intercept parameter indicates a value of $a_D = 6.0 \cdot 10^{10}$ and $m = 3.0$ [11]. Fatigue capacities of S-N curves are associated with a 97.7 % probability of survival, assuming the fatigue test data to be normally distributed [48]. The reason for this is that for a given stress range, it is common to assume that the number of cycles is normally distributed along the regression line. Further, the probability of fatigue failure for a given lifetime is:

$$P_f = P(N_1 \leq N_{design}) = \Phi\left(\frac{logN_{design} - logN_{reg,1}}{\hat{s}}\right) \tag{4.2}$$

where Φ is the cumulative distribution function to the standard normal distribution and $\hat{s}$ is the standard deviation to $log(N_{reg,1})$, describing the mean value at $log(\Delta\sigma_1)$. Further, N_1 describes the number of cycles at $\Delta\sigma_1$, and N_{design} describes the number of cycles at $\Delta\sigma_{design}$. Since it is required by offshore fatigue standard that the design curve is located a little more than two standard deviations below the mean line [11], it results in:

$$logN_{design} \leq logN_{reg,1} - 2\hat{s} \tag{4.3}$$

By combining equation (4.2) and (4.3), it leads to:

$$P_f = \Phi\left(\frac{logN_{reg,1} - 2\hat{s} - logN_{reg,1}}{\hat{s}}\right) = \Phi(-2) = 0.02275 \tag{4.4}$$

where the value represents the area to the left of the Z-score, resulting in a 97.7 % confidence interval. In a corrosive environment, such as seawater, the fatigue life strongly depends on the R-value which describes the stress ratio during stress cycles:

$$R = \frac{\sigma_{min}}{\sigma_{max}} = \frac{\sigma_m - \sigma_a}{\sigma_m + \sigma_a} \tag{4.5}$$

Typical values for stress ratios in fatigue life tests have been performed at $R = 0.1$ [48]. The ratio of minimum to maximum stress in cyclic loading is often used to characterize the specific mean stress situation for a given amplitude where a higher ratio relates to higher mean stress. The mean tension, σ_m, is given as: $\sigma_m = \frac{\sigma_{max}+\sigma_{min}}{2}$, and is defined as the mean value of peak tensile stress and the peak compression value [49]. The stress amplitude is given as: $\sigma_a = \frac{\sigma_{max}-\sigma_{min}}{2}$.

To use test data for a specific mooring line component, DNVGL-OS-E301 [11] recommends performing a linear regression analysis. Either least square or maximum likelihood methods are preferred alternatives to establish reliable S-N curves. An overview of S-N curves for different chains is given in Figure 4.1.

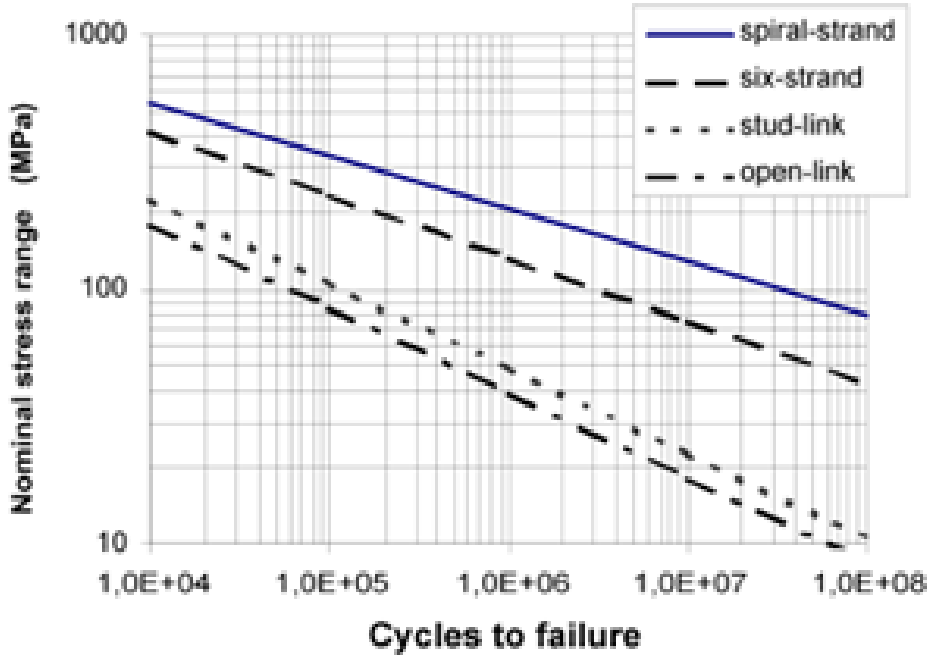

Figure 4.1: Example of S-N curves for chains intended to be applicable in sea water [11].

4.1.2 Fatigue Damage Accumulation - Miner-Palmgren's rule

The cyclic loading for mooring chains varies and changes throughout its lifetime. As a result, both the mean tension and amplitude tension also varies. The cyclic variations may be difficult to reproduce, however, by utilizing Miner-Palmgren's rule, it is assumed an approach of linear cumulative damage. Thus, the amplitude tension only constitutes a proportionally small amount of damage, and a large amplitude tension constitutes major damage. The long-term stress range distribution is expressed by a stress histogram, consisting of stress range blocks, with several stress repetitions:

$$D = \sum_{i=1}^{k} \frac{n_i}{N_i} = \frac{1}{a_D} \sum_{i=1}^{k} n_i \cdot (\Delta\sigma_i)^m \leq \eta \tag{4.6}$$

where:

- D: Accumulated fatigue damage.
- a_D: Intercept of the design S-N curve with the log N axis.
- m: Negative inverse slope of the S-N curve.
- k: Number of stress blocks.
- n_i: Number of stress cycles in stress block i.
- N_i: Number of cycles to failure at constant stress range $\Delta\sigma_i$
- η: Usage factor = 1/DFF from design fatigue factor.

Using the Miner-Palmgren rule is relatively easy and straightforward, however, in offshore structures, the number of load cycles below the fatigue limit also occur [48].

4.1.3 Stress Concentration Factors

Stress formulas are based on structural members having a constant or a gradually changing cross-section. However, such conditions are hardly ever attained as the presence of corrosion, marine growth, holes, and threads result in modifications of the stress distribution. The stress concentration factors are used to estimate the stresses at critical local hot spots in mooring chains and are described as the ratio between the maximal principal stress and the nominal stress. In terms of mooring chains, stress concentration factors amplify the principal stresses due to chain geometry and contact conditions between chain links [12]. A straight chain link subjected to tension is depicted in Figure 4.2.

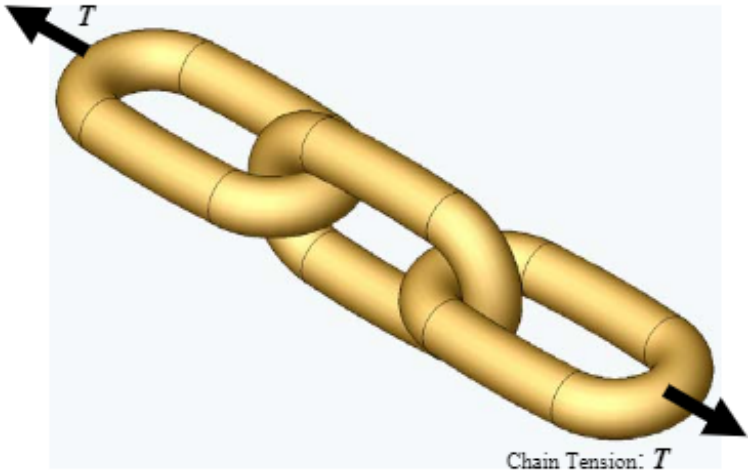

Figure 4.2: A straight chain link in 3D under tension [12].

The nominal tensile stress in the chain is given as:

$$\sigma_{nominal} = \frac{T}{A_{link}} = \frac{T}{2 \cdot \left(\frac{\pi}{4} \cdot d_{nom}^2\right)} \tag{4.7}$$

where T is the tension and A_{link} describes the link cross sectional area, given as two round cross sections of the nominal chain diameter. The stress concentration factor is then defined as:

$$SCF = \frac{\sigma_{max}}{\sigma_{nominal}} \tag{4.8}$$

Stress concentration factors differ greatly depending on the hot spots of the mooring chains. Appropriate values can be obtained using finite element analysis and independent verification on a case by case may be necessary, according to DNVGL-OS-E301 [11]. Values typically range between 2.0-5.0 depending on their orientation [1]. The largest SCFs are measured in the crown region, followed by the bend region.

4.1.4 Intercept parameter, a_D

When performing a fatigue damage calculation, it is necessary to count the stress cycles and classify them into proper sets. By deriving S-N curves for different mean loads, a regression analysis was performed by Fernandez et al. [1], that linearized the logarithmic form of stress and cycle number. This was based on tests showing that the SWT-correction model was preferred over Goodman and Gerber. In addition, a finite element analysis was performed to verify realistic chain dimensions for the tests, in which stress concentration factors were measured and computed both at the crown, bend, and straight parts. The SCFs derived were considered to be representative for the local stress states and the values were given as such:

Table 4.1: Stress concentration factors derived from [1].

Crown	**Inner bend**	**Straight**
4.1	3.6	3.1

Furthermore, they converted this data to different mean loads expressed in terms of a percentage of the MBL of the tested chains. All chains were new and had not been in use, ultimately affecting the S-N design curve as corrosion and surface pits may reduce the fatigue capacity. The regression analysis yielded a latter design curve based on a polynomial fit to fourth order for the intercept parameter up to 40 % MBL:

$$a_D = 4.521 \cdot 10^5 \cdot x^4 - 6.173 \cdot 10^7 \cdot x^3 + 3.174 \cdot 10^9 \cdot x^2 - 7.435 \cdot 10^{10} \cdot x + 6.989 \cdot 10^{11} \tag{4.9}$$

Here, x denotes the mean load expressed in % of MBL and the intercept parameter obtained relates to stress ranges in MPa. In comparison to the value given in DNVGL-OS-E301 [11] for an intercept parameter of a studless chain, it is possible to detect a point of intersection at 20 % MBL in Figure 4.3. For mean loads lower than 20 %, the curve yields a higher intercept parameter, hence a higher fatigue capacity is predicted. At mean loads higher than 20 %, the SWT curve predicts a lower fatigue capacity. Above the mean tension intersect point, only one test has been carried out on a 76 mm R3 chain grade. The test showed that the stress cycles achieved were above the average number of cycles of five Joint Industry Study (ND) tests, hence the expected detrimental effect of the increased mean tension was not captured. Therefore, more tests must be carried out in this regime, to validate if the new intercept parameter is valid in a high mean load regime [1].

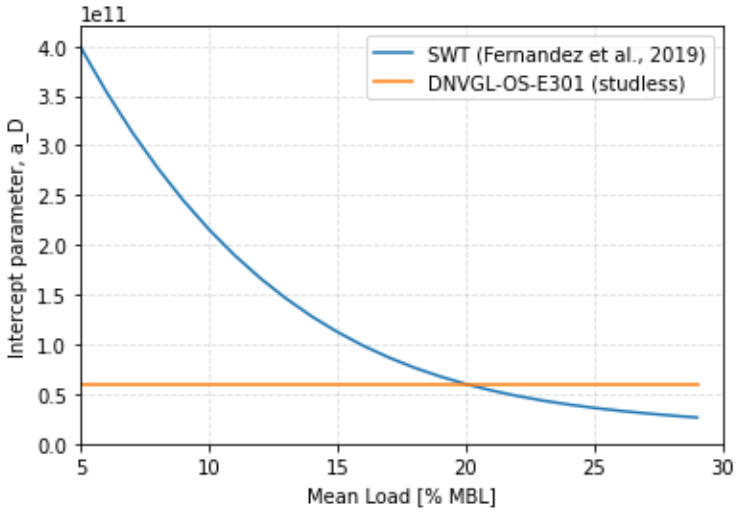

Figure 4.3: S-N curve intercept parameter, a_D

4.2 Mean load consideration

Previous work has shown that the mean tension does have a significant influence on the fatigue life of steel constructions. When the mean tension in the stress direction increases and the stress amplitude is constant, the fatigue life becomes reduced. The effect varies from different materials and with the stress amplitude, as shown in Figure 4.4. To determine how the fatigue strength depends on the mean tension, costly tests have to be performed. Normally, the effect of the mean tension is determined through empirical estimations between the fatigue limit on fluctuating load and the fatigue limit with a specified mean tension.

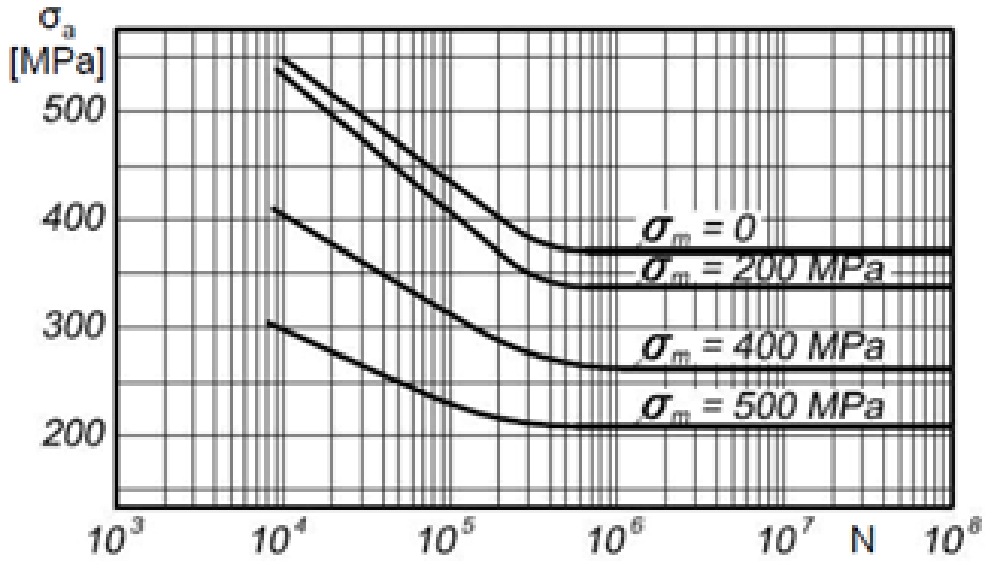

Figure 4.4: Fatigue strength at different values of the mean tension [13].

Compression of mechanical elements contribute to reduced crack initiation, and ultimately an increased lifetime. Thus, when the opposite occurs, the fatigue life is reduced. This effect can be seen in Figure 4.5. For zero mean stress, the effect is seen on the green curve. When the same test is performed under tension, the number of cycles to failure is reduced (yellow curve). Under compression, the number of cycles until failure is increased (orange curve).

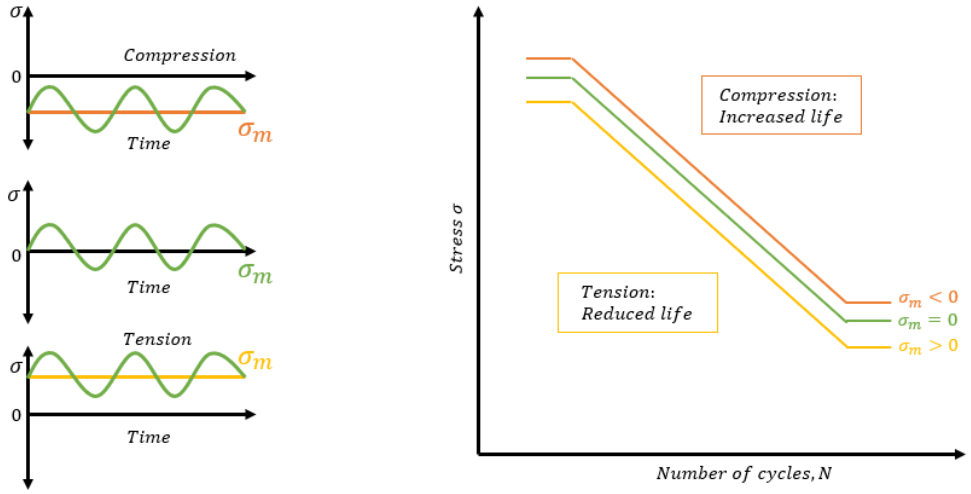

Figure 4.5: Mean stress effects on S-N curves [14].

4.2.1 Mean stress correction methods

Mean stress correction factors are used to transform the stress state of tested chains into different stress states associated with different mean tensions. Several methods have previously been used, such as Soderberg, Goodman, Gerber, Morrow, and Smith-Watson-Topper (SWT), and are presented in Table 4.2. The correction methods are generally applicable to long fatigue life cases (10^6-10^8 cycles), as well as stress causing elastic-strain amplitudes.

Table 4.2: Mean stress correction models.

Correction model	Formula
Soderberg	$\frac{\sigma_a}{\sigma_D} + \frac{\sigma_m}{R_e} = 1$
Goodman	$\frac{\sigma_a}{\sigma_D} + \frac{\sigma_m}{R_m} = 1$
Gerber	$\frac{\sigma_a}{\sigma_D} + \left(\frac{\sigma_m}{R_m}\right)^2 = 1$
Morrow	$\frac{\sigma_a}{\sigma_D} + \frac{\sigma_m}{\sigma_f} = 1$
SWT	$\sigma_D = \sqrt{\sigma_{max}\sigma_a} = \sigma_{max}\sqrt{\frac{1-R}{2}} = \sigma_a\sqrt{\frac{2}{1-R}}$

The nomenclature describes the following: σ_a is the fatigue limit at a given mean tension σ_m and σ_D is the known fatigue limit at cyclic loading. R_m is the tensile strength and R_e is the yield strength and lastly, σ_f is the true fracture strength.

Engineering practice tends to use the SWT-method, as research has shown that it gives nonconservative predictions under compressive mean stress loading conditions and satisfying results for all mean loads [49]. The method is advantageous as it does not depend on hot spot tensions and does not rely on any material constants [1]. Further, it has been shown that correction with SWT has

resulted in 3.5 times extended fatigue lifetime at 10 % MBL compared to 20 % MBL. The method of Goodman seems less conservative than SWT for lower mean loads and correspondingly longer life at 10 % MBL [1].

4.2.2 Single Correction Factor

Lone et al. [19] found a negligible difference in basing the correction on 3-hour mean load compared to mean load of individual stress cycles and proposed to allow for mean load correction based on a single correction factor on results available from a standard fatigue analysis for a semi-submersible unit. The intercept parameter, a_D, of the parametrized S-N curve is constant within each sea state when the mean load is represented by a 3-hour mean value. The mean load correction factor for a single sea state may be expressed as:

$$\frac{\hat{d}_i}{d_i} = \frac{a_D}{\hat{a}_D(\bar{T}_i)} \tag{4.10}$$

where $\hat{d}_i$ is the accumulated fatigue damage with mean load correction for sea state number i. Further, d_i is the corresponding accumulated fatigue damage by applying a standard design curve, and a_D is the standard design curve intercept parameter. Lastly, $\bar{T}_i$ describes the 1-hour mean load in the correlating sea state. Total accumulated fatigue damage with mean load correction may be obtained by a summation of all partial fatigue damages accumulated by each sea state:

$$\hat{D} = \sum_i d_i \frac{a_D}{\hat{a}_D(\bar{T}_i)} \tag{4.11}$$

A single correction factor for total fatigue damage may then be expressed as:

$$\frac{\hat{D}}{D} = \frac{1}{D} \sum_i d_i \frac{a_D}{\hat{a}_D(\bar{T}_i)} \tag{4.12}$$

where D is the total accumulated fatigue damage by standard design curve. As the single correction factor in Equation (4.12) relies solely on results available from standard fatigue damage calculations, the mean load correction may be calculated without the need for additional processing.

If pre-tension is used for approximate estimates, Equation (4.12) simplifies to:

$$\frac{\hat{D}}{D} = \frac{a_D}{\hat{a}_D(\bar{T}_0)} \tag{4.13}$$

where T_0 is the pre-tension expressed in terms of % MBL. Since the level of pre-tension is the same for all mooring lines, the result does not vary and the value remains constant for each line.

4.3 Rainflow counting

To predict the fatigue life for characteristic stress range history, it is necessary to use a counting method that accounts for mean stress with a cycle counting method. Average mean stress can be defined, but it would require that the damage is equally distributed above and below the average assumption. Further, it has been suggested that the average mean stress can be defined for sections of a stress cycle. For irregular cycles with sudden changes, one would have to create arbitrary divisions of the cycles into sections, resulting in fatigue life predictions to vary [50]. However, none of these difficulties are encountered if the mean stress of each cycle is determined, which can be done using the rainflow counting method.

The method of rainflow counting is used to reduce the measured stress intervals into a smaller set of time history to a minimal amount of data required to preserve the fatigue damage. In this procedure, the load spectrum is turned 90°, as seen in Figure 4.6, such that the time axis points vertically downwards.

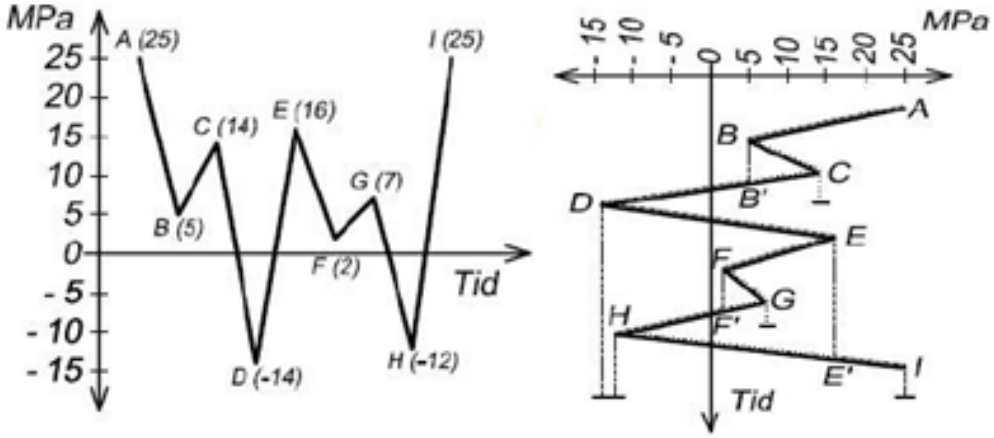

Figure 4.6: Rainflow counting method [13].

A flow of rain starts at each extremal point and is followed by allowing the flow to drip down onto the next roof. However, the flow stops when it drips opposite a larger maximum, or a smaller minimum point, it meets a previous flow falling from above (C-B'), or if it falls below the roof [51]. Each terminated flow is assigned a value that equals the length it has traveled on the horizontal axis and refers to the difference between the starting point and the ending point. A terminated flow represents a half cycle of stress with the assigned magnitude [52]. The rainflow counting method follows standard practices for cycle counting in fatigue analysis in ASTM E1049-85 [53]. It consists of reducing the time history to a sequence of tensile peaks and valleys, closely related to a pagoda roof. This roof or template is then turned clockwise 90° [53].

5 Analysis of Damage

In this chapter a complete model description is provided, together with a description of the environmental conditions. Further, a description of the utilized software and limit states is given.

5.1 Software

SIMA Workbench is software that offers a complete solution and analysis of marine operations and floating systems. It supports the entire process from the definition of the simulation and its execution to the interpretation and documentation of the results. SIMA uses software such as SIMO and RIFLEX as the underlying analysis tool. SIMA is developed and owned by SINTEF Ocean and is available from DNV GL Digital Solutions [54]. The applicability of SIMA has had the highest relevance for this thesis, as all simulations are performed accordingly. Validation of the turbine performance showed some discrepancy between the base case and the provided turbine in the early research phase. Therefore, controllers were updated and corrected throughout the work with the thesis. The specified controller for the thesis was adopted from ROSCO [15], using a variable-speed-variable-pitch (VSVP) control approach. The result gave a satisfying performance, as described in chapter 6.1.

The main program used for post-processing of result files from SIMA was Python. It is an object-oriented programming language, with a special focus on readability. Relevant codes and functions were provided by my main supervisor M.I. Kvittem. Some of these functions were modified to work correctly for my thesis and were mainly applied to retrieve attributes from the .h5-files. The modifications include an implementation of a new rainflow counting algorithm that included mean tensions from Pypi [55]. Further, E. Lone provided helpful functions regarding filtering of time series to detect low-frequency variations in the data and performing a spectral analysis with the Qats-package [56].

5.2 Limit states

When determining the mooring system properties, several regulations and guidelines have to be followed. Mooring systems are generally designed for serviceability and safety and their primary task is to prevent drift off due to wind, wave, and current. The serviceability requirement is to ensure that the motion of the platform does not exceed limits imposed by adjacent floating structures, or the power cable, usually adjusted by line pre-tension, elasticity, weight, and the number of lines. All limit states must still be satisfied after changing any of these parameters. According to DNVGL-OS-E301 [11], a mooring line system shall be analyzed in terms of some design criteria. Their

objective is to ensure a level of safety for mooring systems, consisting of chains, wire ropes, and fiber ropes [11] where the limit states are differentiated as:

- **Ultimate Limit State (ULS)**: An ultimate limit state that ensures the individual mooring lines have enough strength to endure extreme weather conditions.
- **Fatigue Limit State (FLS)**: A limit state that investigates the cyclic loading and the resulting cumulative damage and ensures that the individual mooring lines have adequate capacity to withstand cyclic loading. This limit state is used where fatigue endurance may limit the design of steel components, such as chains.
- **Accidental Limit State (ALS)**: A limit state to ensure the mooring system has adequate capacity to withstand the failure of one mooring line for unknown reasons in extreme weather conditions.

The focus in this thesis relies on an analysis for FLS and to investigate the effect of mean tension in the mooring lines with different sea states. When designing a FOWT, the main concern is safety. The structural safety of the platform is ensured through a methodology of consequence classes based on the failure consequences. Each class is associated with a target safety level related to the structural design and their station-keeping systems. Two consequence classes exist:

- Class 1: Indicates where failure is unlikely to lead to unacceptable consequences, i.e. life-threatening consequences, collision with adjacent structures, or environmental impacts.
- Class 2: Indicates where failure is likely to lead to unacceptable consequences.

For FOWT, which are mainly unmanned during severe conditions, the consequences are mostly related to economic matters, thus the floating structure and the mooring structure are designed to consequence class 1. The target safety level for class 1 indicates a nominal annual probability of failure of 10^{-4}, aiming for ductile failures and to have some reserve capacity. Mooring lines are governed by a design fatigue factor (DFF) multiplied by the total design cumulative fatigue damage. Requirements for DFF in consequence class 1 is DFF = 5. The design life of a mooring line will most likely be shorter than the required design life of the floating structure, thus it is imposed a possibility of replacing the line within the structure lifetime [57].

The total damage for an entire lifetime of a single mooring chain is calculated from the partial damage at each sea state including the probability of occurrence, the total number of occurrences per year, its lifetime, and DFF.

$$D_{tot} = DFF \cdot \text{years} \cdot \sum d_i \cdot p_i \tag{5.1}$$

5.3 Model design

In this section the floating platform is described, together with a description of the mooring system and its parameters. Additional design constraints are briefly explained.

5.3.1 Concept definition

"WINDMOOR: Advanced Wave and Wind Load Models for Floating Wind Turbine Mooring System Design" is a project funded by the Research Council of Norway and the offshore wind industry. The project started in 2019 and has a total budget of 16.6 MNOK. The main goal of the project is *to improve the understanding of loads and forces which affect the design of mooring systems of floating wind turbines. Further, validation of hydrodynamic load models for low-frequency excitation and damping of floating wind turbines is key knowledge that needs to be addressed. In addition, WINDMOOR seeks a better understanding of the consequences of atmospheric stability and aerodynamic interactions between turbines, and efficient analysis models for wind park formations. Lastly, including aerodynamic interactions with shared anchors, power cables, or mooring lines* [58].

The floating platform in the INO WINDMOOR-project is designed by Inocean and Equinor and consists of a semi-submersible platform with three columns comprised of pontoons and steel beams. The tower is located at the top of one of the columns, as seen in figure 5.1. The turbine in INO WINDMOOR 12 MW is a scaled-up model based on IEA's 10 MW wind turbine, combined with aspects from Haliade-X 12 MW turbine from GE [15].

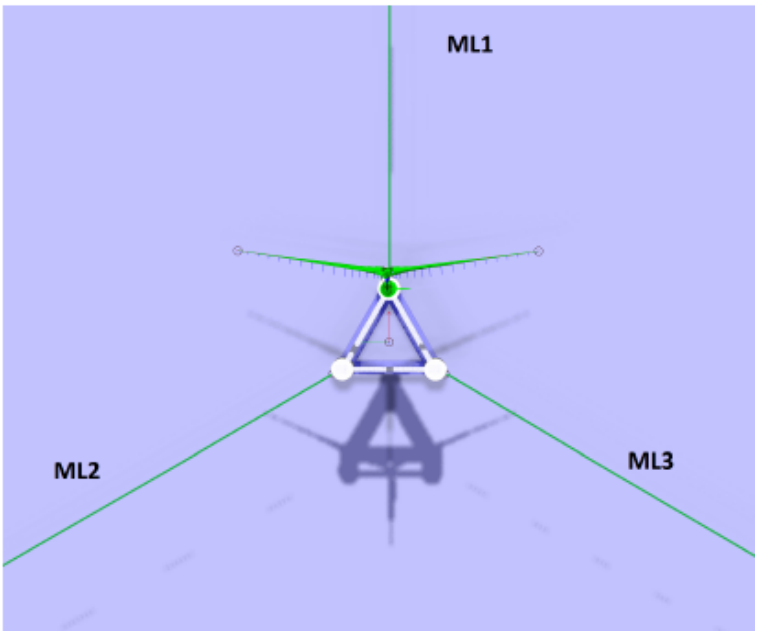

Figure 5.1: Bird's-eye view of the mooring system. Originally from [15].

The chosen site of the simulations was based on an area in the Gulf of Maine, USA, in which three different buoys collect data, as described in [39]. The site also contains open-source buoy data, which is advantageous. Moreover, the mooring system was not specifically designed for the current site, however, it is very similar relative to medium met-ocean conditions. A total of eight years of measurements are available in terms of wind and waves and forms the basis for all the FLS sea states. All simulations are based on a water depth of 150 m, corresponding to the maximum depth in the area. The Gulf of Maine is localized in the north Atlantic ocean, approximately 65 km east of Portland, on the continental shelf. The seabed is relatively flat, with a gentle slope between northern and eastern areas.

The mooring system of INO WINDMOOR 12 MW consists of three catenary mooring lines making an angle of 120° with each other, as shown in Figure 5.1. The mooring line itself is a hybrid between studless chains and polyester, with a total length of 694.8 m at a finite water depth of 150.0 m providing a required pre-tension of 1 050 kN. In addition, it is assumed that the seabed is flat. Each chain is divided into two segments, where the upper part is connected to the fairlead, while the lower part to an anchor. The mass/length of the first two segments accounts for an additional 100 mm of marine growth, while the two last accounts for an additional 50 mm [15]. Theoretical scaling of wind turbines may lead to weight and size becoming too dominating concerning the material costs. An optimal design of wind turbines is based on a concept that minimizes total expected costs per MWh. INO WINDMOOR uses a scaling factor of: $s = \sqrt{\frac{12}{10}} \approx 1.095$. Table 5.1 displays an overview of the main properties of INO WINDMOOR 12 MW wind turbine, compared with IEAs 10 MW wind turbine.

Table 5.1: Main properties of the IEA 10 MW wind turbine and WINDMOOR 12 MW wind turbine, originally from [15].

Parameter	**IEA 10 MW**	**WINDMOOR 12 MW**
Rated electrical power (MW)	10.0	12.0
Specific power (W/m^2)	324.8	324.8
Number of blades	3	3
Rotor diameter (m)	198.0	216.9
Hub diameter (m)	4.6	5.0
Blade length (m)	96.2	105.4
Hub height (m)	119.0	131.7
Generator efficiency (%)	94.4	94.4
Maximum Tip Speed (m/s)	90.2	88.6
Blade mass (kg)	3 x 47 700	3 x 63 024
Hub mass (kg)	81 707	60 000
Nacelle mass (kg)	621 494	600 000

The platform in this thesis, has its own local coordinate system, where the origin is located at MWL, above its horizontal geometric center, as shown in Figure 5.2.

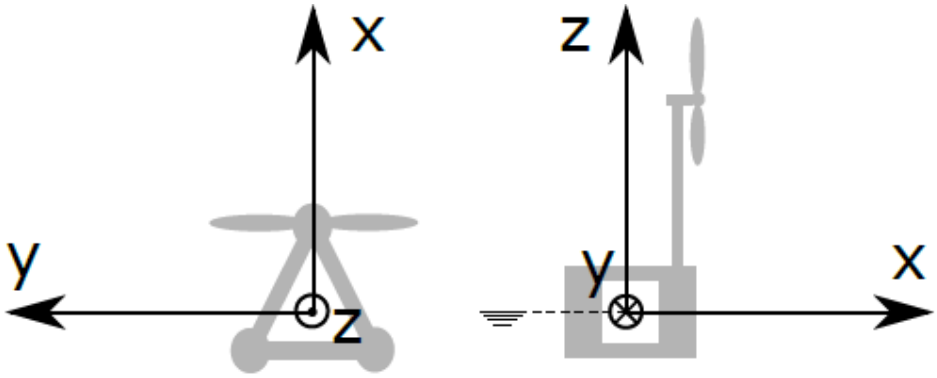

Figure 5.2: Local coordinate system, originally from [15].

The geometry of the floating wind turbine is modeled in SIMA, with the mooring system being parametrized. As mentioned in chapter 5.3.1, the INO WINDMOOR 12 MW turbine is based on an upscaling of the IEA 10 MW wind turbine. The input mass matrix is the total mass of the floating wind turbine and the values are summarized in Table 5.2.

Table 5.2: Total mass properties and inertia forces of INO WINDMOOR FWT.

Property	**Unit**	**Value**
Mass	kg	$14\ 176 \cdot 10^3$
I_{xx}	kg m^2	$2.7292 \cdot 10^{10}$
I_{yy}	kg m^2	$2.7295 \cdot 10^{10}$
I_{zz}	kg m^2	$1.2985 \cdot 10^{10}$

During the analysis of the motions, it is assumed that the connection between the platform and the slender structure is coupled. In essence, it means that the analysis can capture environmental loads and damping contributions from mooring lines accurately. A complete interaction between the mooring lines and the semi-submersible platform is taken into account. The rigid-body FWT natural periods are shown in Table 5.3. Free decay simulations were obtained from the SIMA model and will be useful to verify motion response. Furthermore, a complete full-scale model of the wind turbine is shown in Figure 5.3.

Table 5.3: FWT rigid-body natural periods.

	Surge	**Sway**	**Heave**	**Roll**	**Pitch**	**Yaw**
Nat. periods (s)	97.3	98.0	16.3	29.5	31.4	88.0
Nat. periods (Hz)	0.010	0.010	0.061	0.034	0.032	0.011

Figure 5.3: Full-scale model of INO WINDMOOR 12 MW wind turbine, obtained from [15].

5.3.2 Mooring line properties

The floating platform is connected to the seabed through anchors from the fairlead, and the related coordinates are given in Table 5.4.

Table 5.4: Mooring line coordinates.

	Fairlead			**Anchor**			
Mooring line	**x (m)**	**y (m)**	**z (m)**	**x (m)**	**y (m)**	**z (m)**	**Azimuth (deg)**
ML1	42.7	0.0	0.0	700.0	0.0	-150.0	180
ML2	-21.4	37.0	0.0	-350.0	606.2	-150.0	300
ML3	-21.4	-37.0	0.0	-350.0	-606.2	-150.0	60

The initial design of the mooring line in the INO WINDMOOR base case is based on a hybrid between studless chain link and polyester rope. An overview of the mooring line segment description is shown in Table 5.5, whereas the total accumulated length of one line is 694.8 m. The chain has a catenary shape and the restoring force is mainly achieved through a change in the suspended weight of lines, with a top angle change and chain lifting off the seabed when the wind turbine is moving. Conversely, the polyester rope is more of a semi-taut system where the restoring forces are generated merely as a result of the polyester elastic stiffness properties. Since polyester ropes are highly susceptible to wear, abrasion, and marine growth when positioned improperly, it is common to use top and bottom chains to avoid polyester being exposed to the seabed and splash zone.

Table 5.5: Mooring line segment description.

Number	**Cross Section**	**Type**	**Length (m)**	**Acc. length (m)**	**Num. of elem.**
1	Chain 1	Studless chain	25.0	25.0	5
2	Polyester 1	Polyester	85.0	110.0	17
3	Polyester 2	Polyester	85.0	195.0	9
4	Chain 2	Studless chain	499.8	694.8	45

Furthermore, mooring line properties follows the guidelines specified in [27], where the MBL is a function of the nominal chain diameter, representing the bar diameter, while the axial stiffness depends on Young's modulus, deduced from the stress-strain relationship with the cross-sectional area of the bar used as the load-bearing area. The properties are shown in Table 5.6. Lastly, the equivalent diameter is a measure for a line with constant volume along its length, mainly associated with the mooring chain buoyancy.

Table 5.6: Mooring line properties in INO WINDMOOR 12 MW wind turbine.

Grade	**MBL (kN)**	**Nom. diam. (m)**	**Equiv. diam. (kg/m)**	**Mass/length (kN)**	**Ax. Stiff.**
R3	$1.266 \cdot 10^4$	0.130	0.234	338.0	$1.443 \cdot 10^6$
Polyester	$1.14 \cdot 10^4$	0.190	0.190	35.6	$2.28 \cdot 10^5$

Mooring lines are highly susceptible to marine growth at the specified depths in this thesis. Marine growth is merely site-dependent and affects mass and hydrodynamic properties of slender structures, and is accounted for by increasing the weight and drag coefficients of the mooring line segments. For the chain connected to the fairlead, located in the highly exposed splash zone area, a thickness of 100 mm is added. For depths below 40 m MWL, a growth thickness of 50 mm is added.

Marine corrosion for mooring chains, more specifically corrosion allowance, is defined as an increase in the diameter of the chain. Combined with mechanical loading, it is regarded as one of the main contributors to chain failure [59]. To mitigate these effects, a recommended minimum corrosion allowance is added to the chain diameter of 0.4 (mm/year) [57], and by using half of the fatigue life capacity, it becomes 4.0 (mm/year) = 10 years.

5.3.3 Case study assumptions

The design constraints presented in the following were imposed to simplify the outline of the thesis.

- The governing mooring line parameters were pre-determined.
- Only a single water depth of 150 m was assessed.
- Mooring line orientation and shape were set.
- A limited number of random seeds.
- A single wind/wave alignment was applied, hence the entire wind/wave contribution acted in the same direction on the mooring lines.
- As swell was not available in the buoy data, it has not been included in the analysis.
- A limited, pre-determined set of design load conditions have been considered.

As this is a simplified chain-fairlead system, the nodes at the fairlead will not be simulated by coming out from a pocket, but rather a supernode, which is a branching point with specified boundary conditions. This will ultimately affect the complexity of the structure and also the fatigue analysis,

meaning links at the line terminations that are subjected to extra loads, such as twist and out-of-plane bending (OPB) [60], are not considered.

5.4 Met-ocean conditions

The specifications for the environmental conditions also referred to as the met-ocean conditions, which are utilized to perform the fatigue analysis require three input values. That is a significant wave height H_s, peak wave period T_p and wind speed W_s. The met-ocean conditions greatly influence the design of mooring lines, and to ensure realistic and coherent results between parameters, specific data from site B was chosen [39].

When assessing accurate and appropriate sea states for the offshore wind turbine, the correlation of wind- and wave conditions shall be considered in terms of the long-term joint probability distribution. A proper simulation length aims to reflect the experienced fatigue damage in the mooring lines with an acceptable level of uncertainty in the data. Research has shown that the effect of simulation length of short-term conditions does not differ greatly when the simulation time is more than 1 800 s. By estimating a 20 year fatigue life based on 1-hour simulation length, a relative difference of less than 4 % appeared in a time-domain analysis [33]. Therefore, the simulation length of 4 000 s was considered sufficient to provide accurate analysis in the time-domain analysis, where the first 400 s was neglected due to start-up transient effects.

Uniqueness is ensured by varying the seeds; a specified random number used to generate wind and wave variations. IEC 61400-3 [61] specifies a random number of seeds to be six. However, the structural response of a FOWT differs from a fixed structure, so the seed number was set to one for all simulations.

Wind climate data are assumed from a 1-hour steady mean value of wind speed, direction, and gust, consisting of measurements from 2003 to July 2015 [39]. Wave height climate data is measured in half-hour continuous periods. Then, the mean of those values is provided as significant wave height for 1-hour. The wave period corresponds to the peak period of the time series recorded during the wind height 30 min interval. A Weibull distribution was selected to represent the long-term probability distributions of wind speed in the Gulf of Maine [37]. As the wind speeds in Table 5.7 are based on one hourly mean values at a hub height of 131.7 m, they may be transferred into appropriate values at height 10 m above sea level, using Equation (3.3).

Studying the frequency spectrum is a key tool for the monitoring of dynamic phenomena. For

developing waves created by wind friction, a modified Pierson-Moskowitz spectrum is used, namely the JONSWAP spectrum. Figure 5.4 describes the JONSWAP spectra of the derived sea state parameters from Table 6.2, namely the significant wave height and the mean wave period. It depicts the distribution of wave energy among the different wave frequencies of wave-lengths on the sea surface, hence the distribution of the variance of the sea surface height, meaning the height of the sea surface if there were no waves. An increased significant wave height results in a correspondingly larger peak, as depicted in the figures below.

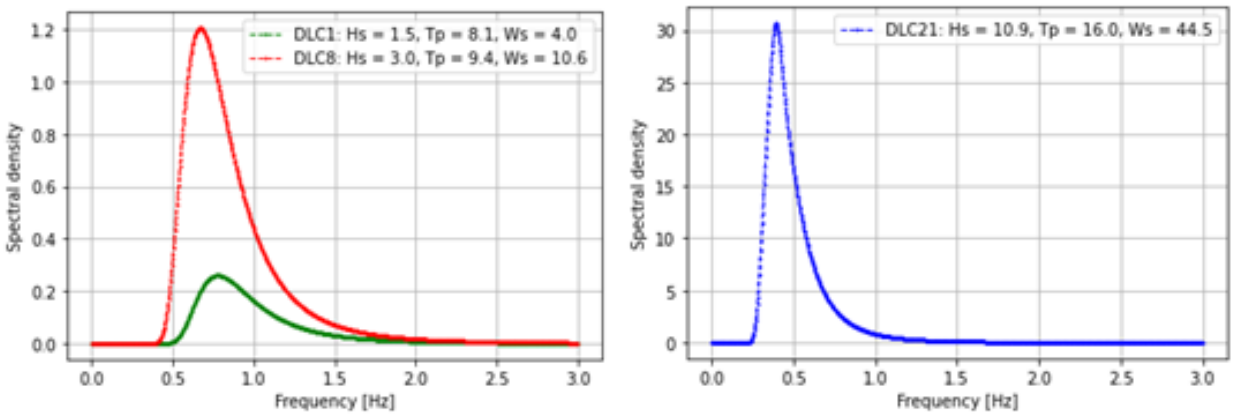

Figure 5.4: JONSWAP spectrum for (a) DLC 1 and DLC 8 (b) DLC 21.

The spatial, stochastic turbulence model applied is the Kaimal wind spectrum and exponential coherence model. The coherence model describes the spatial correlation of the longitudinal velocity component [33]. Further, for accurate modeling of wind turbulence obtained at offshore sites in FLS conditions, the Normal Turbulence Model (NTM) from IEC 61400-1 [34] is used, with a reference turbulence intensity of $I_{ref} = 0.12$ from wind turbine class IC.

Current characteristics are based on mean values for the hourly surface current speed and its associated direction. As mentioned in chapter 3.4, the current is comprised of two parts; current induced by wind and current induced by the tide. For the estimation of the wind component of the current speed, winds influence the climate in the current direction, thus k = 0.021. Further, mean wind speed at 10 m height is used as a reference. Since measurements are done at a hub height of 131.7 m, a wind speed profile, or more precisely a power-law profile, is assumed. The terrain roughness, α, is set to 0.14. The currents induced by tides have been estimated at the sea surface as the difference between the total mean current speed and the wind component of that current, thus $v_{c,tide} = 0.016$ [39]. The current induced by speed profile for wind utilizes a value of $d_0 = 75$ m, taken as half of the water depth of the simulation, with MWL $z = 0$. The current induced by the tide profile is represented by a potential profile.

Met-ocean data is separated into bins, giving reasonably accurate estimates of the related oceanic states. Based on this, several rules apply, given in [17]. Table 5.7 displays met-ocean conditions for all FLS cases, and it is assumed uni-directional wind, waves, and current. Swell was not available in buoy data, and therefore not considered.

Table 5.7: Met-ocean conditions for FLS of mooring lines [17].

Number	**Hs (m)**	**Tp (s)**	**Ws (m/s)**	**Probability (%)**
1	1.5	8.1	4.0	13.764718
2	1.5	7.9	8.0	27.069097
3	1.5	7.5	10.6	11.397941
4	1.5	6.8	14.0	15.752486
5	1.5	6.2	17.0	5.725809
6	1.5	5.7	23.5	2.407441
7	3.0	9.9	8.0	2.963756
8	3.0	9.4	10.6	1.556702
9	3.0	8.6	14.0	4.683125
10	3.0	7.8	17.0	4.694512
11	3.0	7.3	23.5	6.195911
12	5.5	10.4	8.0	0.055303
13	5.5	9.9	10.6	0.079703
14	5.5	10.4	14.0	0.309061
15	5.5	10.2	17.0	0.408286
16	5.5	9.3	23.5	1.244385
17	5.5	8.9	38.0	1.629901
18	7.5	10.0	10.6	0.001624
19	7.5	9.8	23.5	0.019517
20	7.5	10.4	38.0	0.040663
21	10.9	16.0	44.5	0.000055

As seen in Figure 5.5, the probability of occurrence for a significant wave height of 1.5 m accounts for more than 75 % of the load cases. An increasingly larger wave height is less likely, thus the probability of more extreme sea states is seemingly lower.

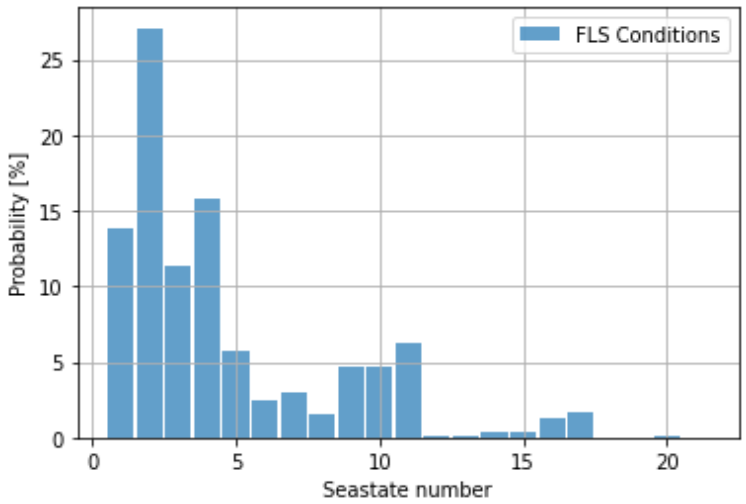

Figure 5.5: Probability of occurrence for every seastate.

5.5 Case study

To describe the mean load tension associated with each stress cycle, three alternative ways are presented:

- Cycle mean: An average of the maximum and minimum load in each individual cycle.
- 1-hour mean: A 1-hour mean load for the sea state the cycle is encountered in.
- Pre-tension: A representation of the specified mooring line pre-tension.

Pre-tension is usually not represented as a mean load, however, due to its simplicity, it is a well-defined operational parameter that yields a constant S-N curve intercept parameter for all cycles and conditions. Furthermore, the INO WINDMOOR base case does not differentiate the level of pre-tension in the mooring lines, even simplifying the process additionally.

5.5.1 Post-processing set-up

In order to obtain the mean loads and stress ranges from the simulated DLCs, a method of post-processing is applied in Python. A simple function based on ASTM-E1049-85 [53] rainflow cycle counting algorithm for fatigue analysis, returned a list of stress ranges, mean tensions, and cycle counts of the accumulated fairlead axial forces [55]. This leads to the basis for all damage results.

The rainflow counting algorithm proceeds by matching peaks and valleys to form a closed hysteresis loop. However, when the algorithm reaches the end of the axial force time series, some unmatched peaks remain unclosed, hence not counted by the algorithm. These half-cycles typically include large peaks and valleys and potentially the highest stress values, contributing to the highest fatigue

damage. In this thesis, the treatment of these half-cycles was not done in the most conservative manner, which is counting them as one complete cycle. However, all unclosed cycles were counted as half-cycles and multiplying the accumulated damage with its respective cycle count to provide its true weight. As a result of this, high mean loads are also accounted for, providing a wide range of values, being very influential for FOWT [62]. In addition, a brief evaluation of the half cycles was performed, to check their influence on the mean tension. Applicable standards [63], recommend that "*all unclosed cycles are avoided by adopting an appropriate algorithm*". As a result, important information may be lost.

The fatigue damage calculations applied a standard S-N design curve as a basis, with an intercept parameter of $a_D = 6.0 \cdot 10^{10}$, $t_{ref} = 0.25$ mm, $m = 3.0$ and $k = 0.25$. For mooring chains, the S-N design slope is fixed, thus a breaking point on the curve do not appear.

6 Model verification study

The objective of this section is to verify the performance results obtained numerically by post-processing in Python. This includes control of the motion response of the turbine and low-pass filtering of the fairlead tensions. Further, base case results are discussed and compared to the obtained simulation results.

6.1 Verification of turbine performance

In order to verify the controller performance and the behavior of the floating wind turbine, checks are undertaken. This includes the rotor speed, blade pitch, and thrust force. The verification is performed by utilizing a signal output file in SIMA, together with post-processing in Python. It is important to understand the relationship between power and wind speed to determine the required control type and do proper optimization. Ideally, a wind power curve is limited by a cut-in speed, ensuring that the available energy is above a set minimum threshold value, while the cut-out speed ensures a discontinuity to prevent damage. All result files from SIMA are based on the met-ocean conditions in Table 5.7 and will therefore limit the number of points generated on the curve.

A method of weighted means is applied to each performance parameter to account for the probability of occurrence of each sea state, in which it calculates the average by multiplying the weights with its respective mean and taking its sum [64]. It is given as:

$$\bar{x}_w = \frac{\sum_{i=1}^{n}(w_i \cdot x_i)}{\sum_{i=1}^{n} w_i} \tag{6.1}$$

where $\bar{x}_w$ is the weighted mean variable, w_i is the allocated weighted value and x_i is the probability described by Table 5.7. The reason for this is to account for the probability of occurrence for each sea state, and its influence on the performance. However, by application of regular mean, the results do not deviate, as depicted in appendix A. This detailed view shows the complete time series plotted against turbine performance parameters. The detailed view was implemented to visually assess the stationary values of the parameters, and validate that the mean values correlate to the calculations.

The primary objective of a wind turbine's control system is to ensure a safe and stable operation while maximizing the overall energy output. A method of peak shaving was utilized on the base case performance curves, where the objective was to limit aerodynamic loads, at the cost of reducing power capture in the transition from below-rated to the rated region. The technique includes an imposing of a blade-pitch angle before the rotor reaches its rated speed [15]. This is a

load mitigation strategy and changes the turbine controls, employed to limit ultimate loads on the turbine.

For a given wind velocity, it exists an optimum rotor speed where the power generated by the turbine reaches a maximum. The wind direction is normal to the plane of rotation of the turbine blades, and all blades experience turbulent wind, thus it varies along each blade. The model uses a variable-speed-variable-pitch control (VSVP) approach, meaning that below the rated rotor speed, the torque is set to optimize power capture, while zero-blade pitch angle is maintained. Above rated speed, the generator torque may be kept constant at rated torque or vary with generator speed to keep a constant power [15].

Figure 6.1 compares the complete wind turbine performance curves for different parameters of the INO WINDMOOR 12 MW wind turbine (red line), and the case study turbine (blue dotted line), generated with aero-elastic simulations in SIMA. A small difference can be seen in the rotor thrust force of about 100 kN at rated speed. When wind speeds between cut-in and rated speed occurs, the blade pitch is kept at a constant and the generator torque varies such that the turbine operates close to the optimal tip speed ratio ($\frac{blade\ tip\ speed}{wind\ speed}$) [43]. As the wind turbine reaches rated wind speed, it also reaches rated power, rotational speed, and thrust, thus a flattened top of the curve. Due to a lack of measurements around rated speed, and an imposed yaw angle, slight deviance can be found. Furthermore, the generator power tends to be slightly above rated power. This can be explained by the controller's generator efficiency parameter of 94.4 %, meaning that the blue dotted line depicts the rotor power and not the actual generator power. However, by multiplying the efficiency parameter with the rotor power, the two curves would be closer. It is important to mention that the case study performance curves were generated on an assumption of the tower base being cantilevered to the ground. Since the simulated INO WINDMOOR 12 MW turbine was installed on a floating platform, including irregular waves, motion instability occurs, hence slight deviance.

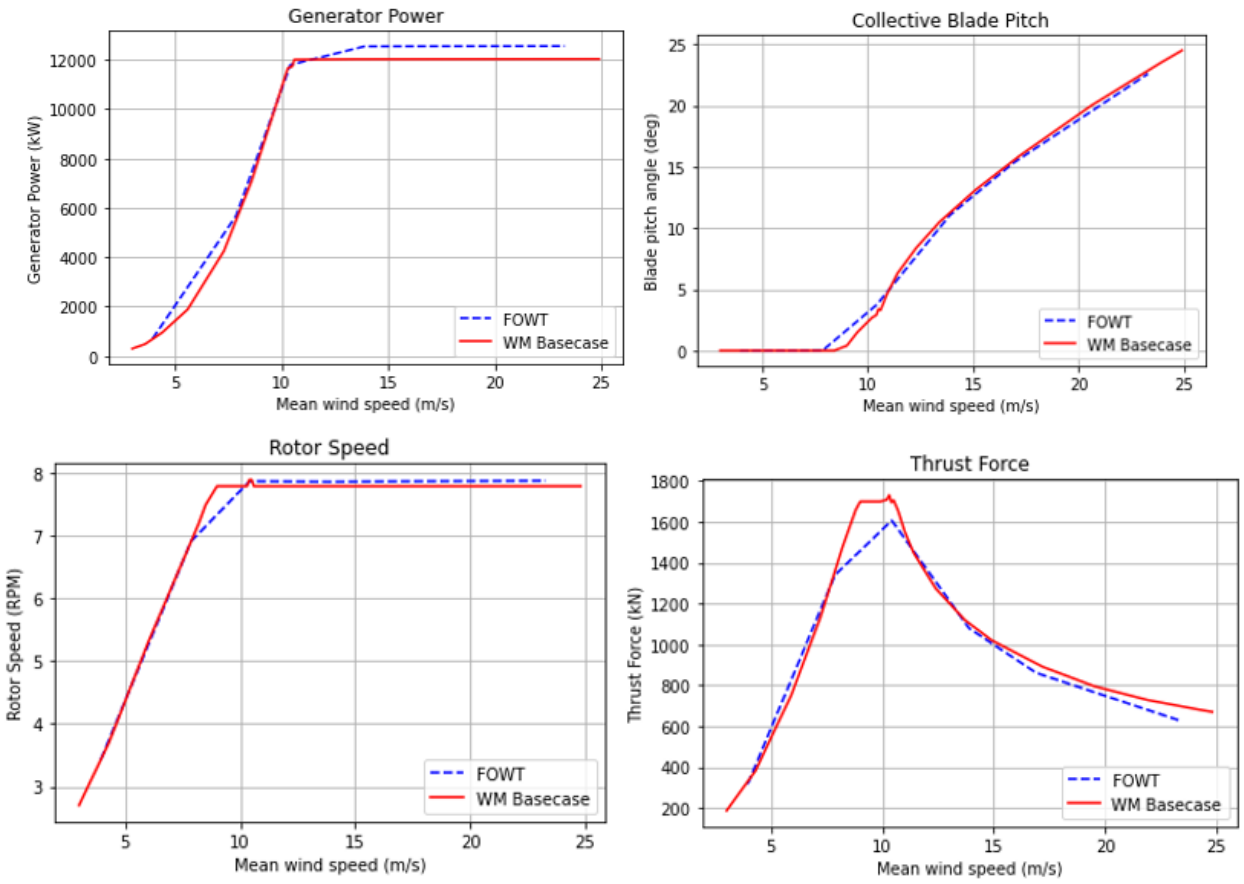

Figure 6.1: WINDMOOR 12 MW turbine performance curves.

6.2 Verification of extreme turbine performance

The FOWT used in this thesis is not able to operate at all wind speeds due to physical limitations. High wind speeds can cause overheating of the generator, resulting in a decrease of life of the control system and a loss in electricity production. As wind speeds exceed the cut-out speed of 25 m/s, the FOWT enters a mode of survival or an idling operation mode. When the wind turbine is idling, the rotor is approximately at a stand-still, and the blades pitch to a feather of 88°. A load mitigation concept allows the rotor to rotate at low speeds and minimizes the aerodynamic loading of the rotor.

Start-up and shutdown situations are assumed to have a small contribution to fatigue life and damage since the probability of occurrence is very small. A total of three design load cases (DLCs) are considered for the verification of extreme performance in the wind turbine, shown in Table 6.1.

Table 6.1: DLCs for verification of extreme performance curves.

DLC number	**Hs (m)**	**Tp (s)**	**Ws (m/s)**
17	5.5	8.9	38.0
20	7.5	10.4	38.0
21	10.9	16.0	44.5

It is important to inspect the performance of extreme wind speeds to validate the controller and motion behavior of the floating wind turbine. As seen in appendix B, the rotor speed fluctuates between 0-2 RPM, disregarding the transitional start-up phase. The blade pitch angle instantly stabilizes at 88°, as expected for all extreme load cases. For the thrust force, mean values are seen to be negative in this state. This is mainly due to the shape of the blade and the lift/drag characteristics of the turbine airfoils giving a negative lift, thus a negative thrust. In other words, the turbine may work as a blower rather than an actual turbine. In addition, the drag forces exerted on the tower dominates in this state, so a negative thrust force does not affect the motion of the platform.

6.3 Verification of motion response

For the inspection of motion response, a method of post-processing in Python is applied. This includes the application of the package Qats [56]. Offshore wind turbines are regularly subjected to wind, waves, current, and other loads with a wide range of excitation frequencies [43]. Since a catenary mooring system affects the low-frequency excitation due to environmental loads, it does not significantly influence the magnitude of the first-order wave-induced motions.

Application of low-pass filter to a time series removes high-frequency fluctuations from the time series. This results in a smoother version of the original data and dampens higher frequencies in the data and allows lower frequencies to pass through. By applying a low pass filter on the resulting catenary axial force of the load cases, all signals with a frequency lower than a set cutoff frequency pass and attenuates signals with frequencies higher than the cutoff.

The assessment of the spectrum peak frequency, f_p, can be performed using different algorithms [42], mainly by basing it on the 5^{th} order spectral moment of the reconstructed wave spectrum. However, since many peak periods would occur if all sea states were printed, and basing it on the largest value of the reconstructed spectra could lead to the variability of the peak frequency, a brief visual observation is done. Furthermore, this frequency leads the basis for the cutoff frequency applied in

the low pass filter. The examined load conditions presented in the following represents a range of possible operating conditions according to relevant sea conditions, from Table 5.7. Three different DLCs are chosen to represent calm, intermediate, and extreme environmental conditions, shown in Table 6.2.

Table 6.2: Design load cases for analysis

DLC number	**Hs (m)**	**Tp (s)**	**Ws (m/s)**
1	1.5	8.1	4.0
8	3.0	9.4	10.6
21	10.9	16.0	44.5

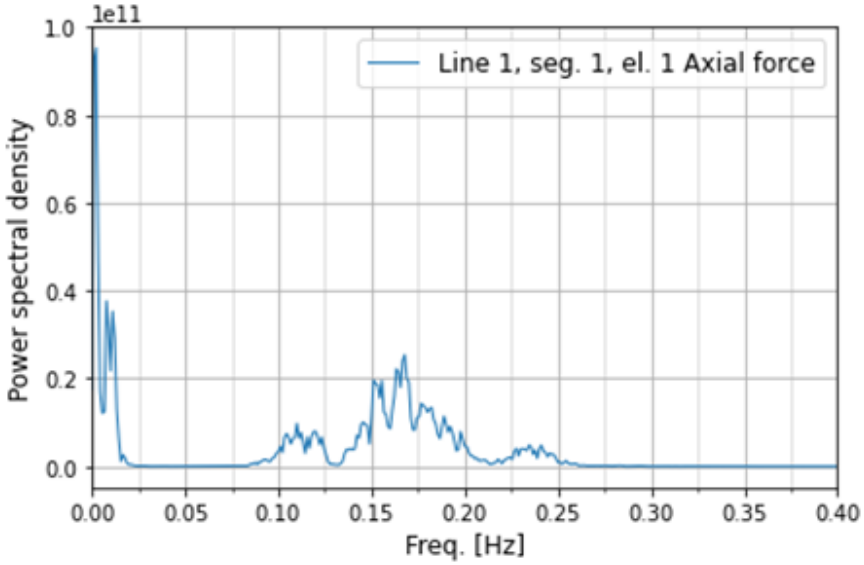

Figure 6.2: PSD of line tension, ML1 - DLC 1.

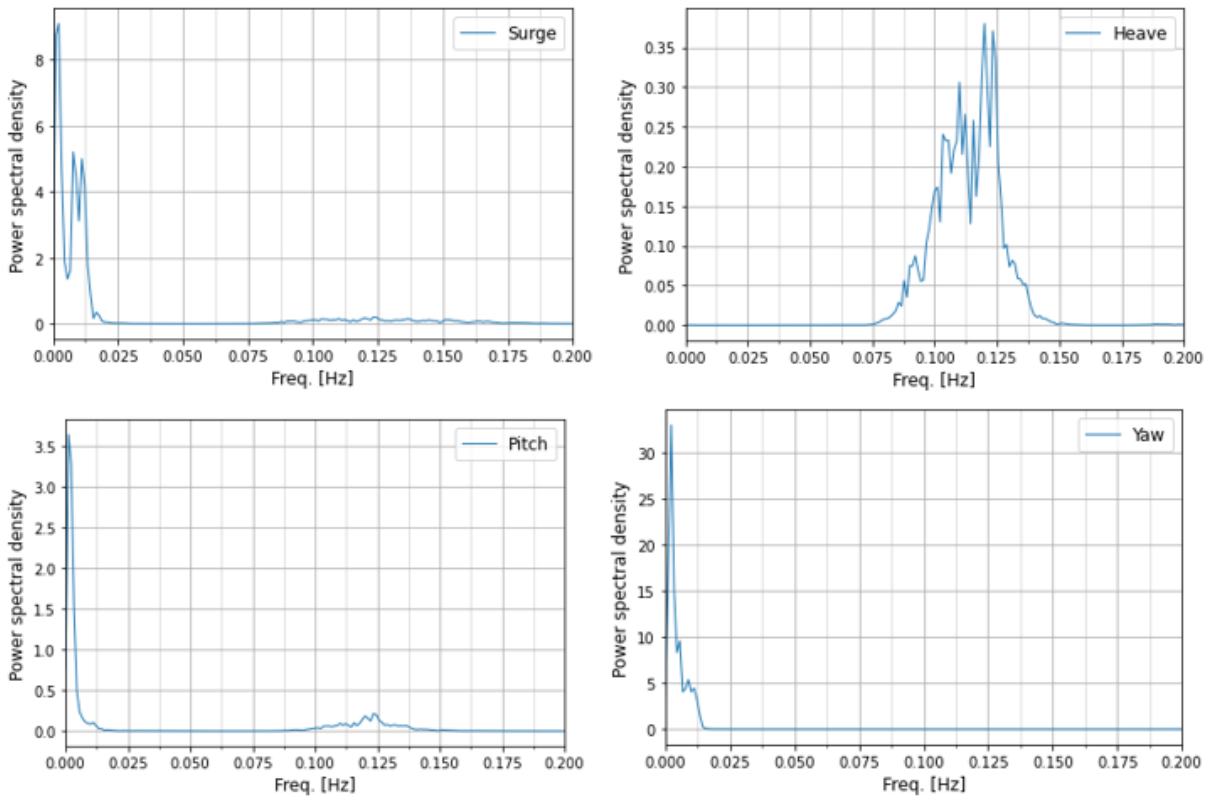

Figure 6.3: Motion response spectrum, DLC 1.

The power spectral density for ML1, DLC 1 is shown in Figure 6.2. It must be noted that the presented results are examined through a simulation time of 4 000 s, where the first 400 s is neglected due to startup transient effects. ML1 is the most exposed line to wind and waves and is characterized by wave-frequency from 0.085-0.25 Hz, and a low-frequency wind-induced response from 0.0-0.02 Hz. DLC 1 has a low significant wave height, and it is seen that the largest peak occurs in the low-frequency area. This corresponds to dominating wind, including a dominant wind-induced surge resonance, as seen in Figure 6.3, further confirmed by surge natural period in Table 5.3. Objectively assessing an optimum cut-off value for low-pass filtering may be done by regression equations or residual analysis [65]. However, by visually examining the PSD of the line tension in Figure 6.2, 12 s (0.083 Hz) is chosen as an appropriate value located between the low-frequency and wave-frequency area.

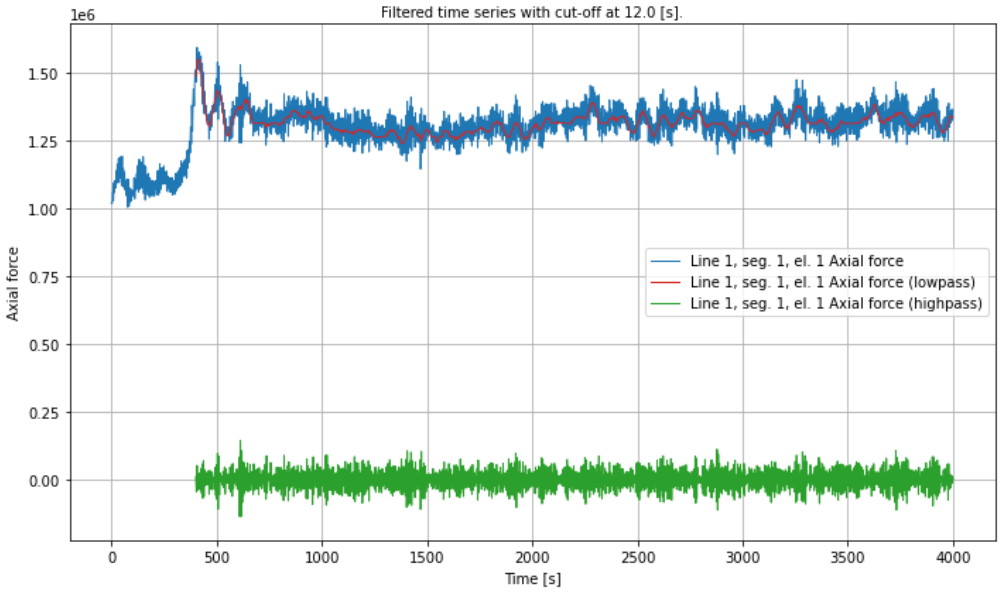

Figure 6.4: Filtered time series for axial force of ML1 - DLC 1.

As seen in figure 6.4, the low-pass filtering line is smoother than the axial force line. Furthermore, this is applied when assessing the low-frequency standard deviation of tension in the ML to detect a variation of the 1-hour mean.

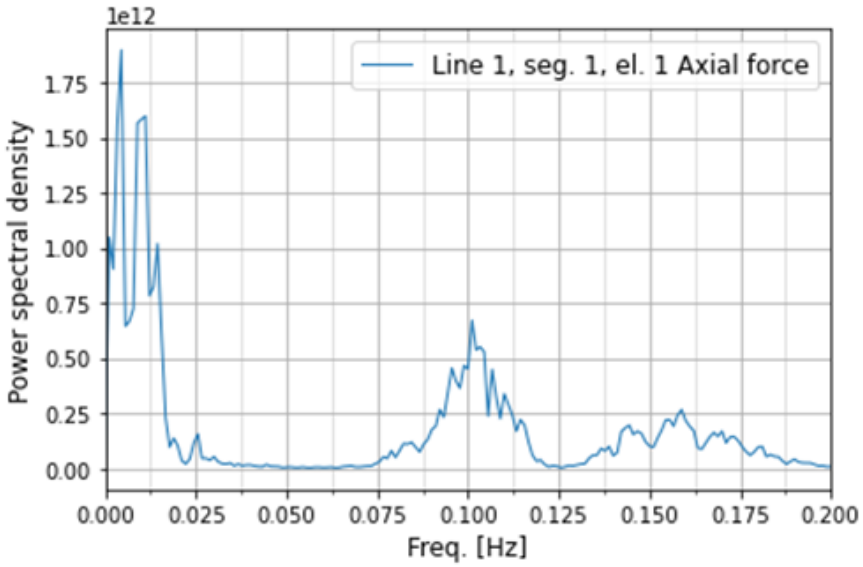

Figure 6.5: PSD of line tension, ML1 - DLC 8.

A moderate sea state is considered in DLC 8, corresponding to rated wind speed and subject to moderate environmental conditions. The motion response spectra are rather similar to DLC 1, as seen in Figure C.4, but exhibits a larger increase in total response due to wind load and waves. For surge motion, the contribution from the surge resonant motion dominates the low-frequency region with two distinct peaks occurring at 0.004 Hz and 0.01 Hz. A third peak is seen at 0.014 Hz,

corresponding to yaw motion. An increase in pitch resonant motion can also be found, due to an increase in wind speed. The presented ML tension spectrum in Figure 6.5 shows a dominating wave-frequency response from 0.075-0.200 Hz, where heave motion is the most significant contributor. Both ML2 and ML3 are highly dominated by low-frequency energy as seen in Figure C.5.

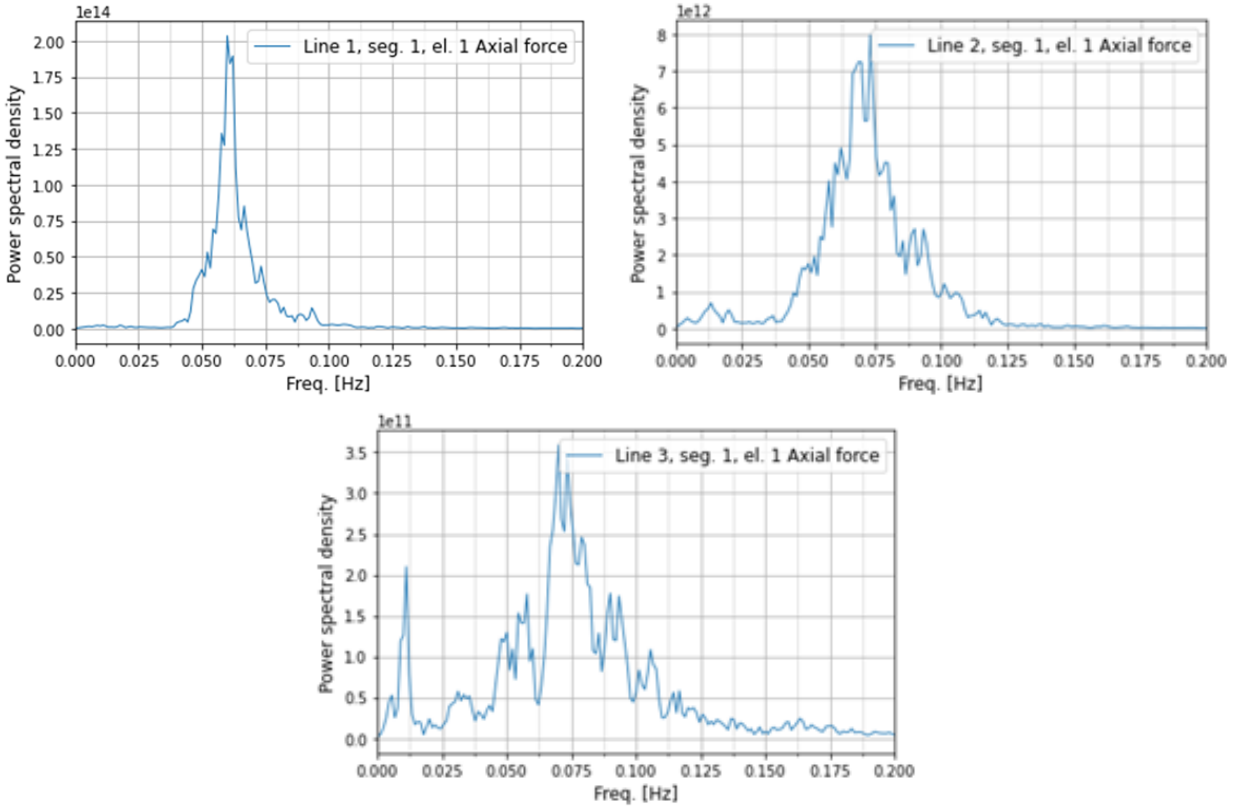

Figure 6.6: PSD of line tension in DLC 21 for (a) ML1 (b) ML2 (c) ML3.

The last DLC is subjected to extreme environmental conditions and reflects a wind speed of 44.5 m/s and wave period of 16.0 s. The mooring line tension spectra are shown in Figure 6.6. It is seen that wave-frequency motion for ML1 dominates the range between 0.038-0.1 Hz, corresponding to heave response. Further, a definite peak can be found at 0.011 Hz (88 s) for ML3 in the low-frequency range, due to a dominating yaw resonant response.

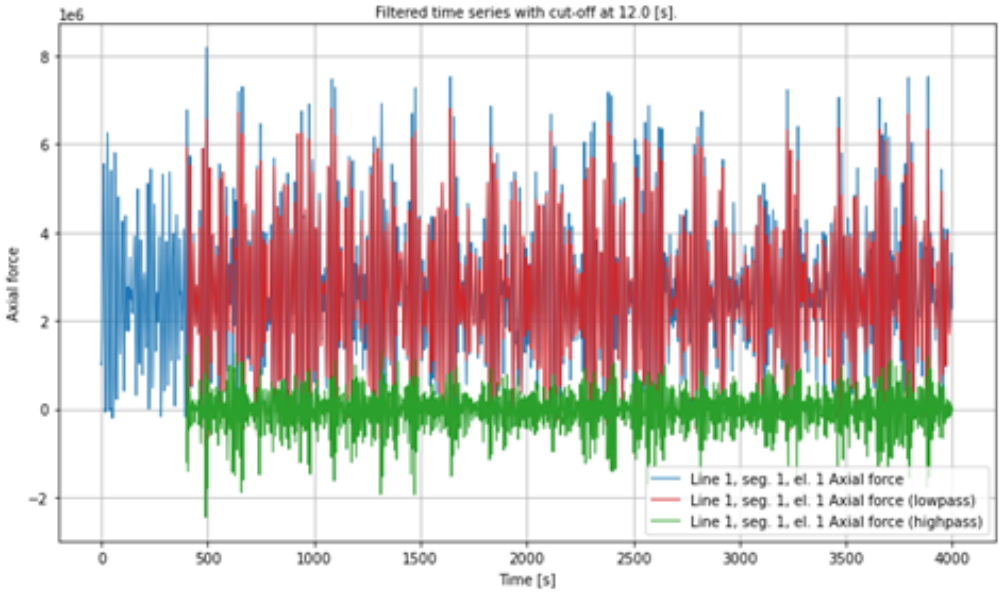

Figure 6.7: Filtered time series for axial force of ML1 - DLC 21.

The resulting filtered time series of the axial force in the fairlead of ML1 is shown in Figure 6.7. Definite separation of low-frequency and wave-frequency range do not exist, as it is mainly wave-frequency dominated. Therefore, it becomes difficult to find an optimal cut-off value for low-pass filtering, hence the resulting filtered time series are overlapping slightly.

7 Results and discussion

A quasi-static time-domain analysis has been performed in this thesis. This involves looking into the influence of mean tension in mooring line fatigue life. The results of the conducted case study are presented and discussed in this chapter, and subdivided into two main sections; Mean load distribution and accumulated fatigue damage. In the first section, mean tension dependency is shown in different forms and evaluated. The second section deals with the accumulated fatigue damage and presents the damage contribution in terms of sea states and mean tension. A detailed overview of the total accumulated damage for all sea states can be found in appendix E.1.

7.1 Mean load distribution

The following chapter contains results from frequency histograms used to show the mean load variation in the accumulated sea states. Further, cumulative histograms are used to explain the percentage of the total number of accumulated cases of the % MBL.

7.1.1 Frequency histogram

Histograms of cycle mean and 1-hour mean loads are shown in figure 7.1 and 7.3 respectively, for 18 sea states, where the three most extreme sea states are excluded. Histograms including all 21 sea states are shown in Figure 7.2 and 7.4. A simplified set of design conditions was given for this thesis, and the separation of the three most extreme sea states were performed to detect a large likelihood of occurrence in the data, as these sea states account for more than 98 % of the total probability.

The cycle mean histograms are described by a bin size number of 50 and 1-hour mean applies a bin size number of 18, corresponding to the number of sea states. For ML1, in Figure 7.1, the cycle mean shows two distinct peaks, one at around 10 % MBL and another at 15 % MBL. As most of the mean tension is seen to be below the 20 % mark, the current engineering standard approach is seen to overestimate mean load dependency. Cycle means for ML2 are concentrated between 4-7 % MBL with little variation in the results. A significant peak is seen at around 5.5 % MBL, likewise for ML3.

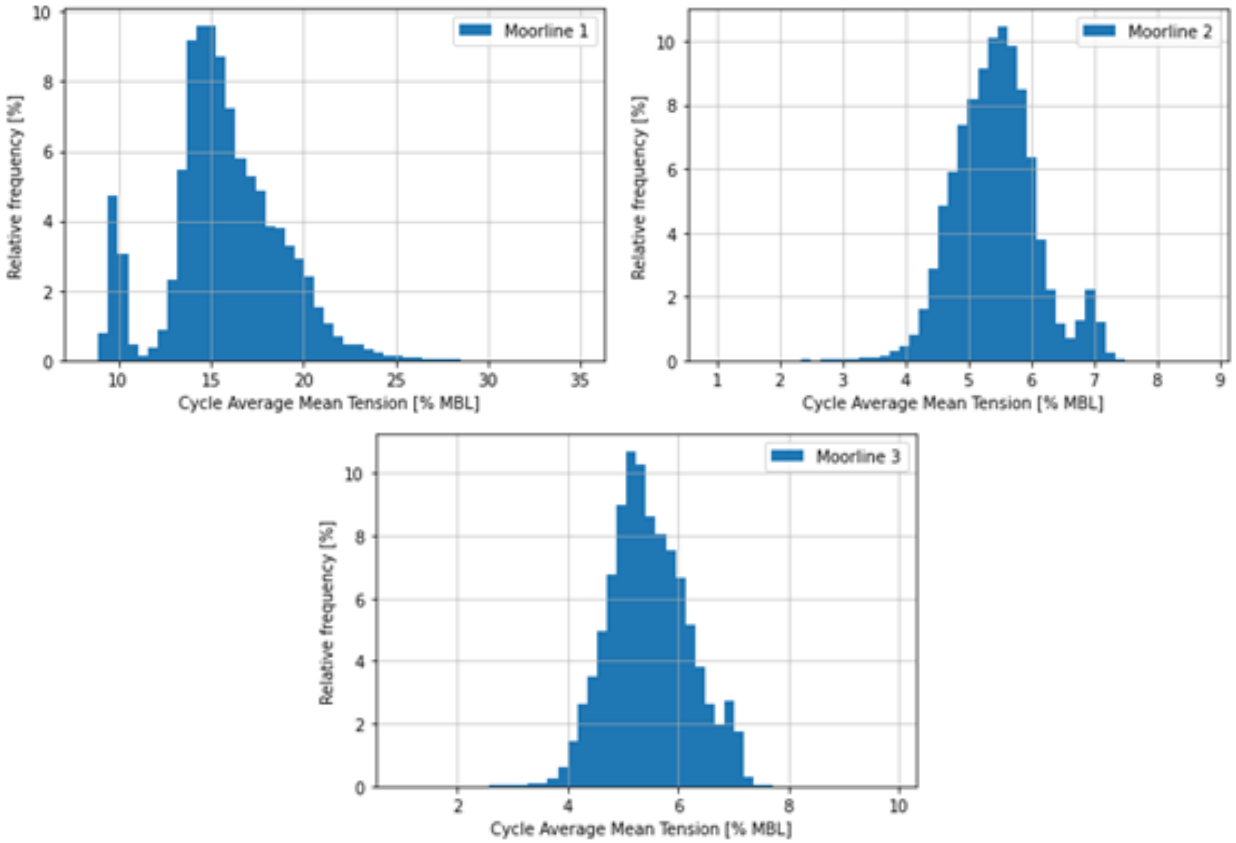

Figure 7.1: Mean tension relative frequency histogram for cycle mean without the three roughest sea states in (a) ML1 (b) ML2 (c) ML3.

When the severe DLCs are included in the histograms, the cycle mean tension range is increased slightly, and a tendency of occurrences can be detected around 0 % MBL for ML1. This may imply a compression of the mooring line, causing negative stress. However, the mooring lines are pre-stressed to prevent slack during the expected range of platform motion. It does not necessarily mean that the mooring line goes into compression, but rather losing its pre-tension and hence stiffness characteristics. Since heave motions in extreme sea states are the primary motion for tendon tensions, it may help to explain the negative mean loads. However, extreme surge and pitch motions may also lead to slack events, being very detrimental to fatigue life. Moreover, the event of tendon slack does not necessarily take place during extreme storm events, but may also occur during operation, in the event of an emergency stop. This may imply faults in the optimization process of the mooring lines, and the first step to resolve this issue would be to increase pre-tensioning.

Variations in mean tension are considerable and the extreme DLCs contribute to results in the high mean load regime. However, it is recalled that on the upper side of the mean load regime, only one chain test has been carried out, with unexpected results. Therefore more tests were recommended to be performed in that range to validate the model. Thus, it becomes difficult to recognize

the results obtained from the simulations in that range. Extreme results for ML2 show a small trend of values between 10-17.5 % MBL, differing from Figure 7.1 (b). Considering ML3, most of the cases still occur in the same range as without the extreme DLCs. As mentioned in chapter 5.5.1, the rainflow counting method in Python does not neglect half cycles. Therefore, high mean loads also occur and may help to explain the wide range of results.

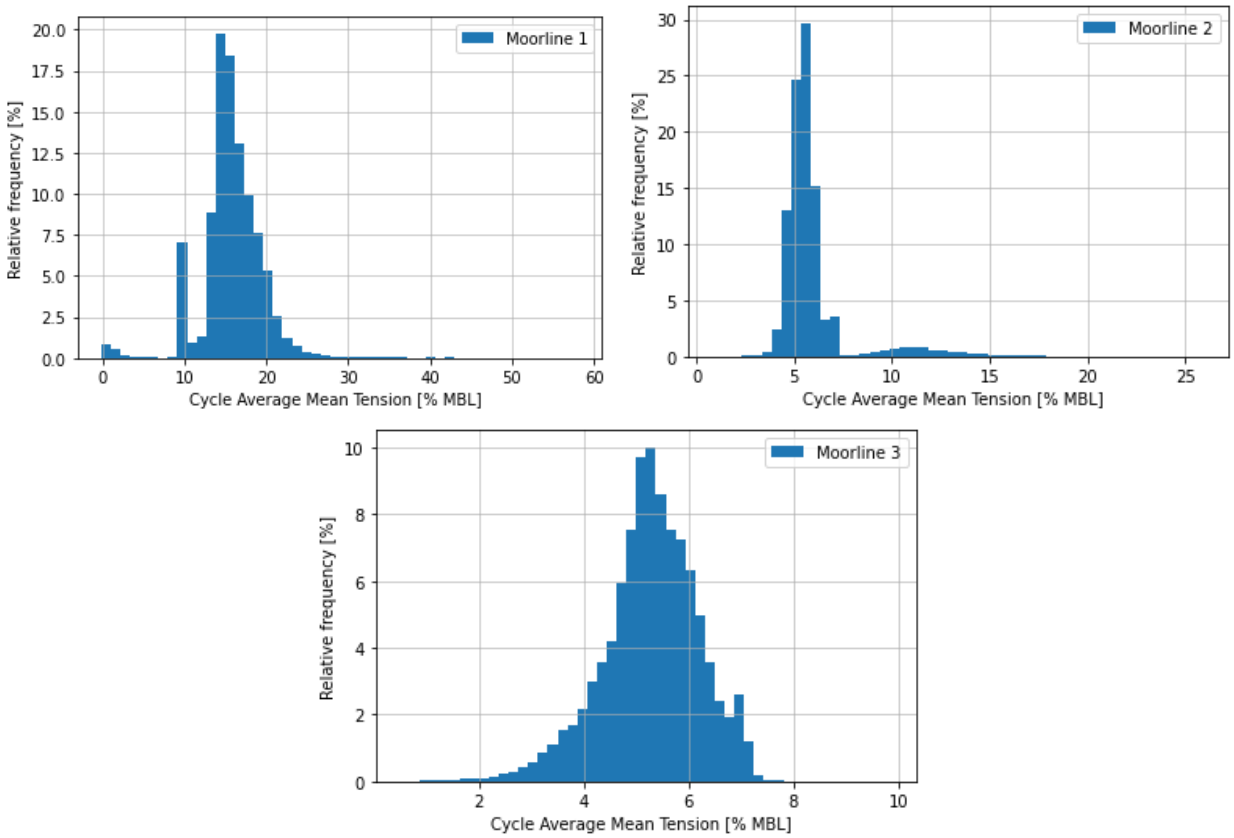

Figure 7.2: Mean tension relative frequency histogram for cycle mean for all sea states in (a) ML1 (b) ML2 (c) ML3.

Similar peak trends can be recognized in the histograms of 1-hour mean load depicted in Figure 7.4, even though the sample size is a lot smaller. As a result, extreme outliers and bars filling the entire load range are missing. It can be observed that three significant peaks occur in ML2. the reason for this lies upon the three extreme DLCs, contributing to a higher mean load range than the other DLCs. By neglecting them, the plots are similar to ML3.

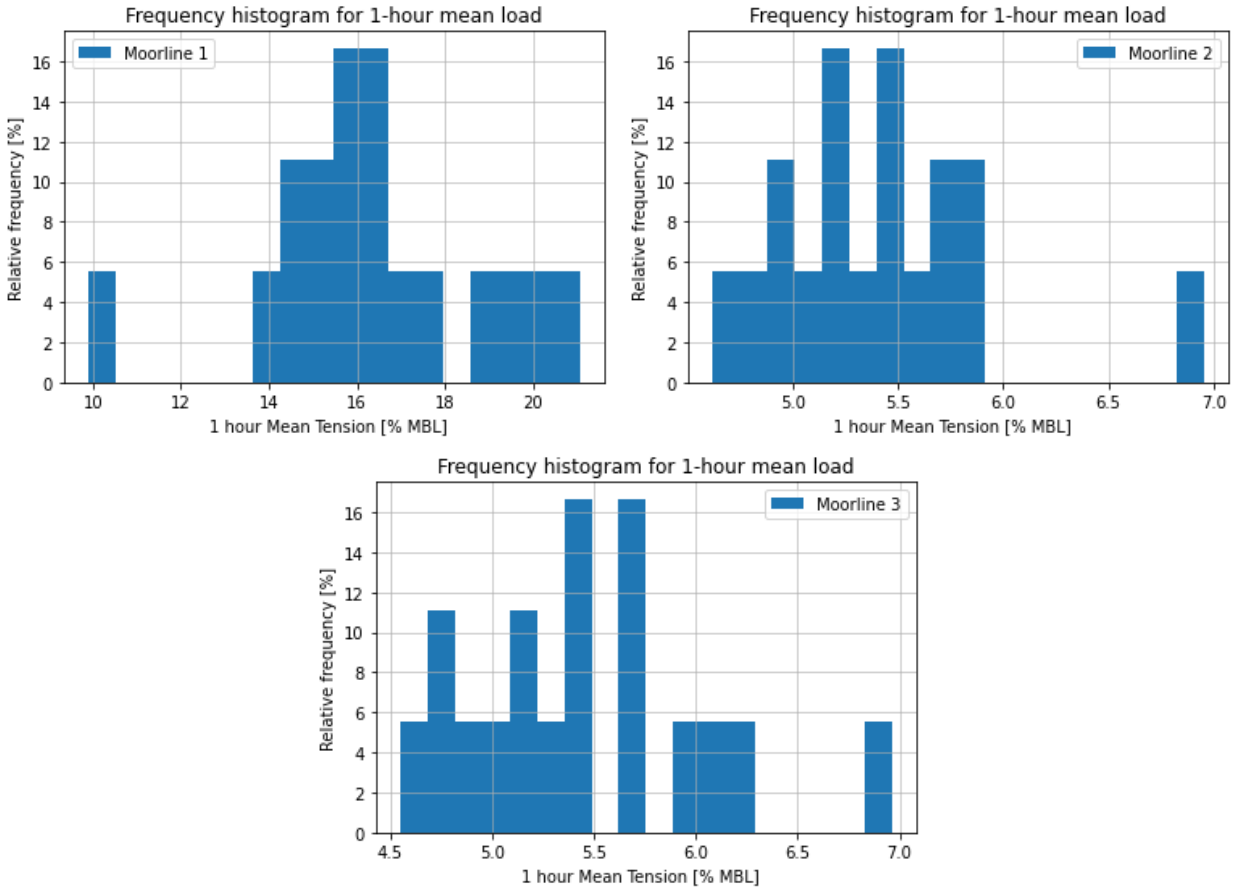

Figure 7.3: Mean tension relative frequency histogram for 1-hour mean without the three roughest sea states in (a) ML1 (b) ML2 (c) ML3.

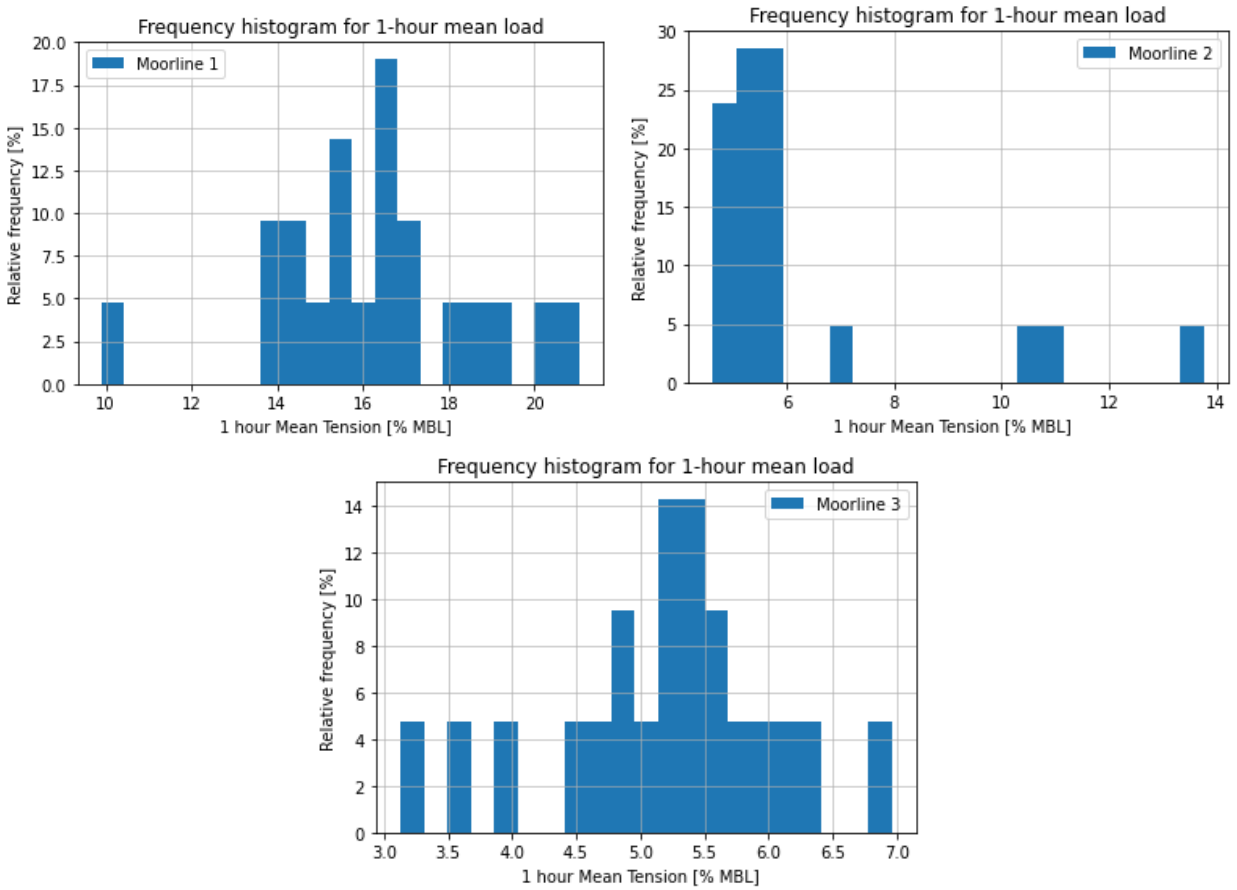

Figure 7.4: Mean tension relative frequency histogram for 1-hour mean for all sea states in (a) ML1 (b) ML2 (c) ML3.

As mentioned in chapter 5.5.1, the rainflow counting algorithm counts all cycles, regardless of them being unclosed. Figure 7.5 shows the mean tension histogram for all unclosed cycles in the mooring lines. Similar trends can be seen in Figure 7.2, however, the sample size is significantly smaller. Interestingly, the unclosed cycles do not contribute much to the high mean load regime for ML1, contrary to ML2, as smaller peaks are found there.

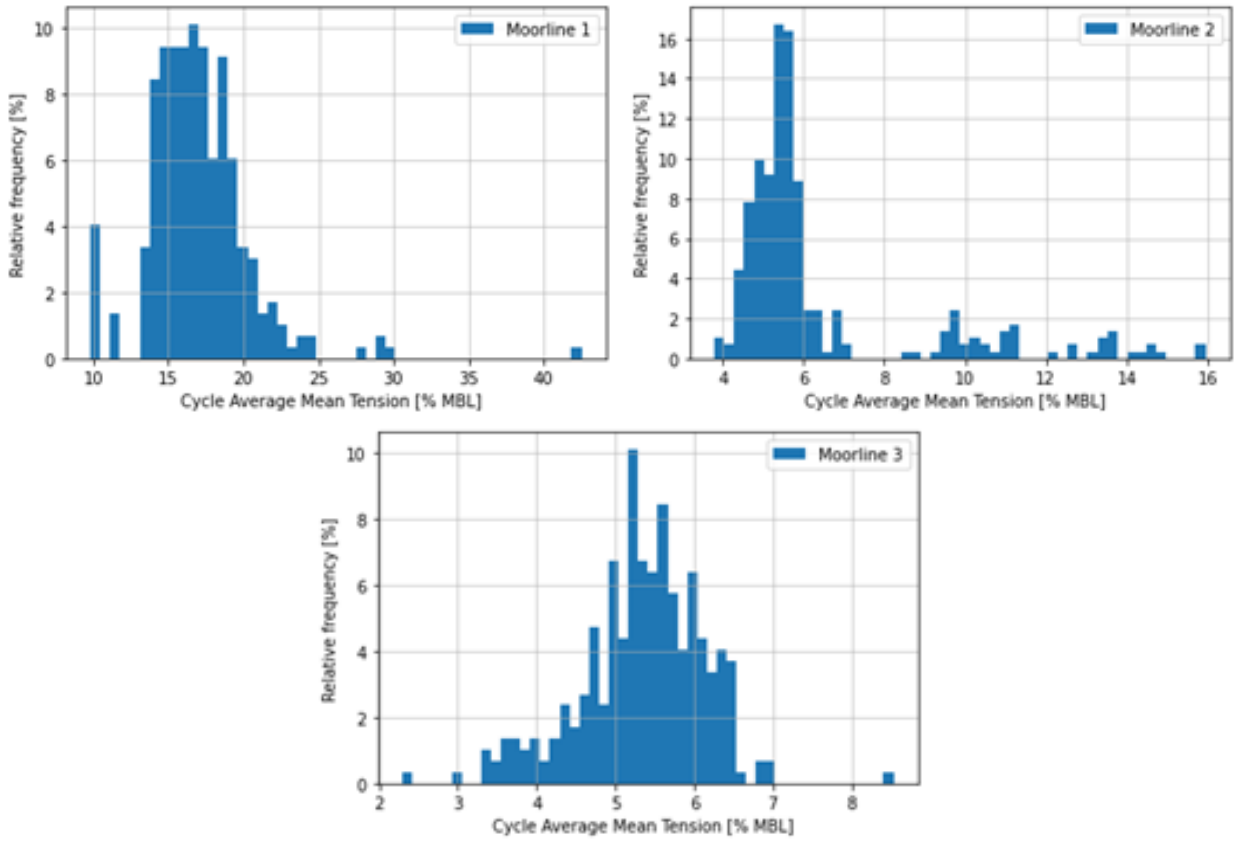

Figure 7.5: Mean tension relative frequency histogram for cycle mean only for unclosed cycles in (a) ML1 (b) ML2 (c) ML3.

Figure 7.6 relates the wind speeds to 1-hour mean tensions for each mooring line. The red dots indicate the wind speed corresponding to the mean load. Wind speeds between 10-15 m/s are seen to accumulate high mean tensions in ML1, mainly due to high thrust force. For ML2 it is seen that higher wind speeds accumulate significantly deviating results, compared to the rest of the data, contrary to ML1. Lower mean values are seen for high wind speeds in ML3. This may come as a result of the yawing mechanisms due to the incoming turbulent wind. The aerodynamic lateral force and yaw moment causes a yaw rotation and thus a yaw angle of the platform. This yaw angle gives the thrust force an arm and causes a driving yaw moment.

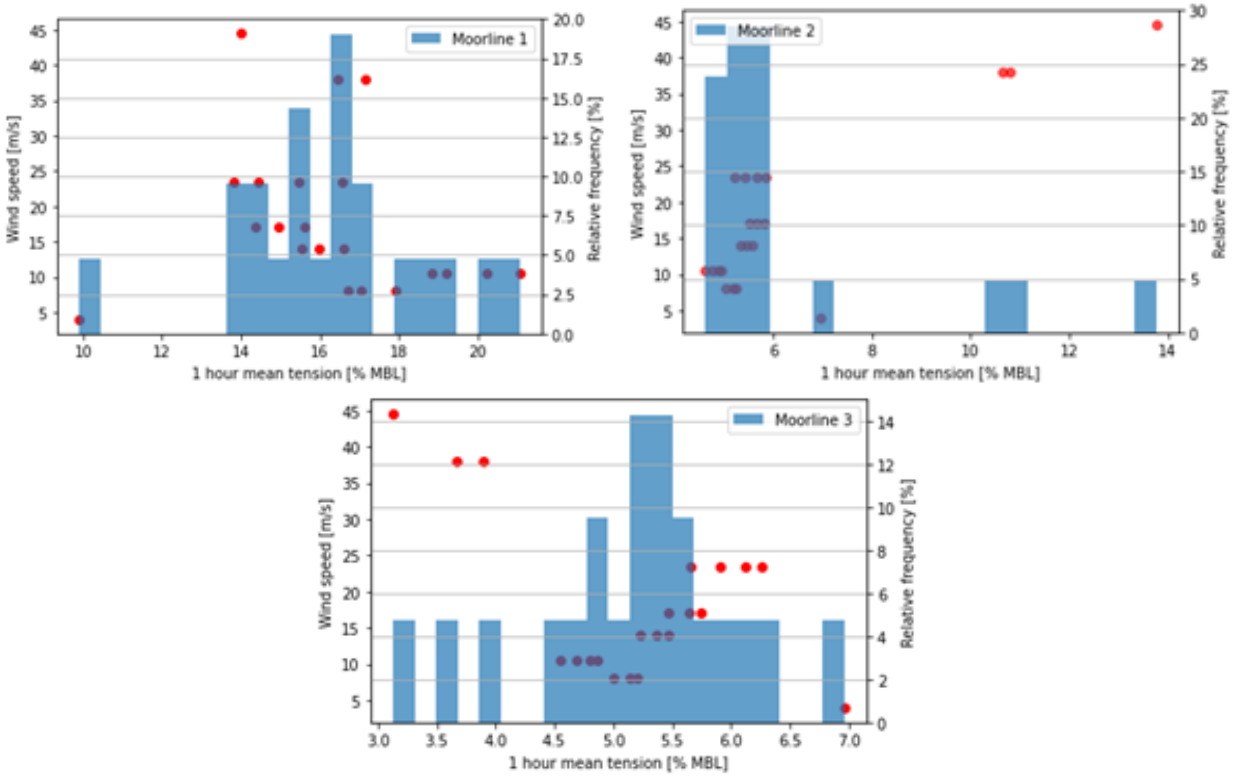

Figure 7.6: Wind speed vs 1-hour mean tension for (a) ML1 (b) ML2 (c) ML3.

7.1.2 Cumulative frequency histograms

Cumulative histogram plots show the counts not only for a single bin but rather give the counts for the exact bin with all smaller bins added. This then explains the percentage of the total number of accumulated cases. Cumulative histograms of cycle mean loads for the respective mooring lines are shown in Figure 7.7 below. The figure depicts a relative cumulative frequency distribution and is used to classify the frequency of the occurrence of the mean load tensions, both for the cycle mean and the 1-hour mean. As expected, ML2 and ML3 are not subjected to dominating wave directions, and most of the mean tensions correspond to values ranging from 4-8 % MBL. This is significantly less than the 20 % MBL typically used in mooring line fatigue analysis. Conversely, most of the mean tension for ML1 ranges from 9-23 % MBL. It can be observed that about 90 % of the mean loads are explained by loads less than 19 % MBL, both for cycle mean and 1-hour mean. By comparing the cycle mean and the 1-hour mean, the results seem to deviate more in ML1 than in ML2 and ML3. It should be noted that the sample size of the 1-hour mean is significantly smaller than the cycle means since it is the average stress of the entire range within one sea state. Hence a lower statistical power in which it is more difficult to detect the statistical variability.

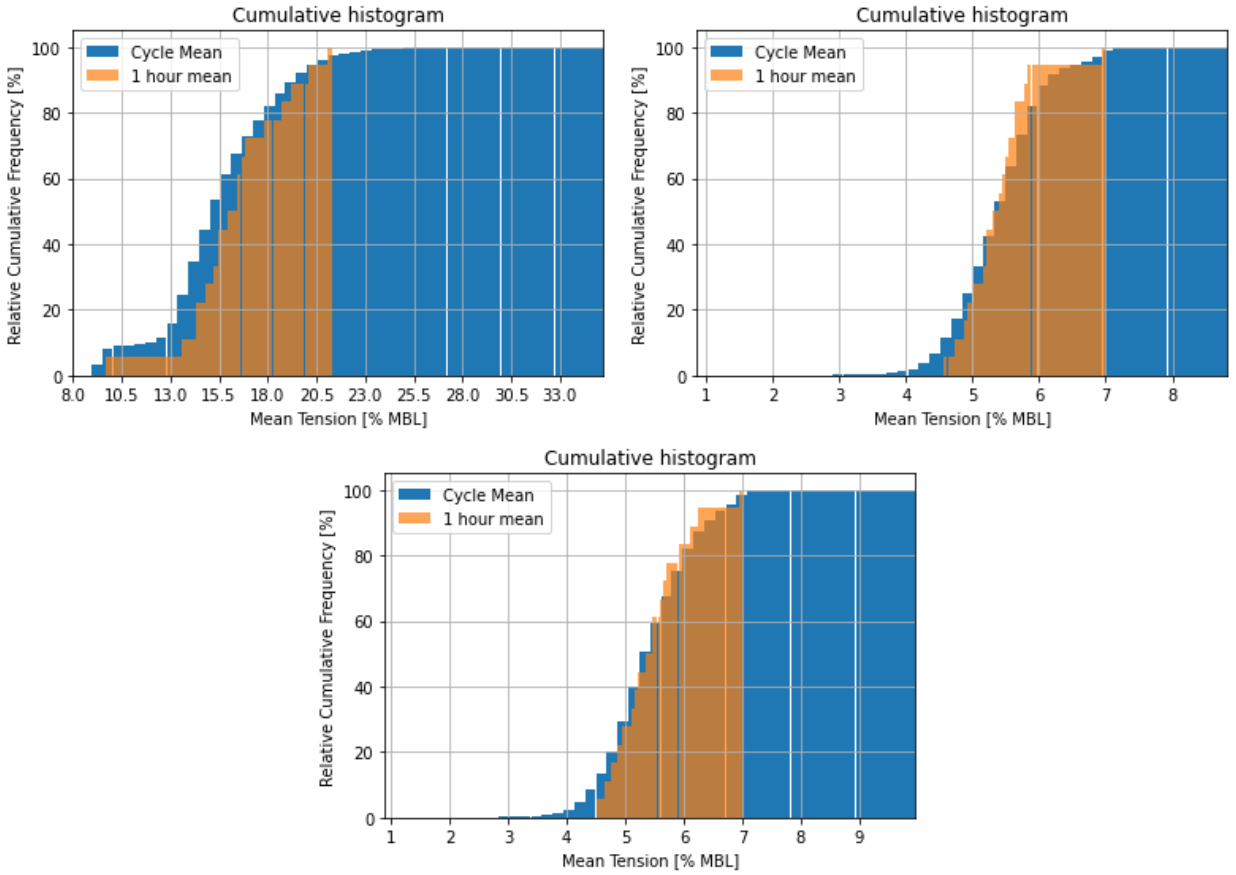

Figure 7.7: Cumulative frequency histogram for 1-hour mean load vs. cycle mean without three extreme sea states for (a) ML1 (b) ML2 (c) ML3.

When accounting for DLC 17, DLC 20, and DLC 21 from Table 5.7, which correspond to the three most extreme sea states, the cumulative frequency histograms tend to be similar to those without the extreme sea states. This can be seen in Figure 7.8. However, the range is extended for the cycle mean, especially for ML1. Values can even be seen below 0 % MBL and are discussed in chapter 7.1.1. In addition, the total relative frequency reaches 100 % at around 54 % MBL, indicating extreme outliers in the data and values above the 20 % MBL mark. As mentioned in chapter 4.1.4, the parametrized S-N curve intercept parameter developed by Fernandez et al. [1] is yet to be validated for the high mean load regime. Therefore, it is difficult to verify this result and its reliability.

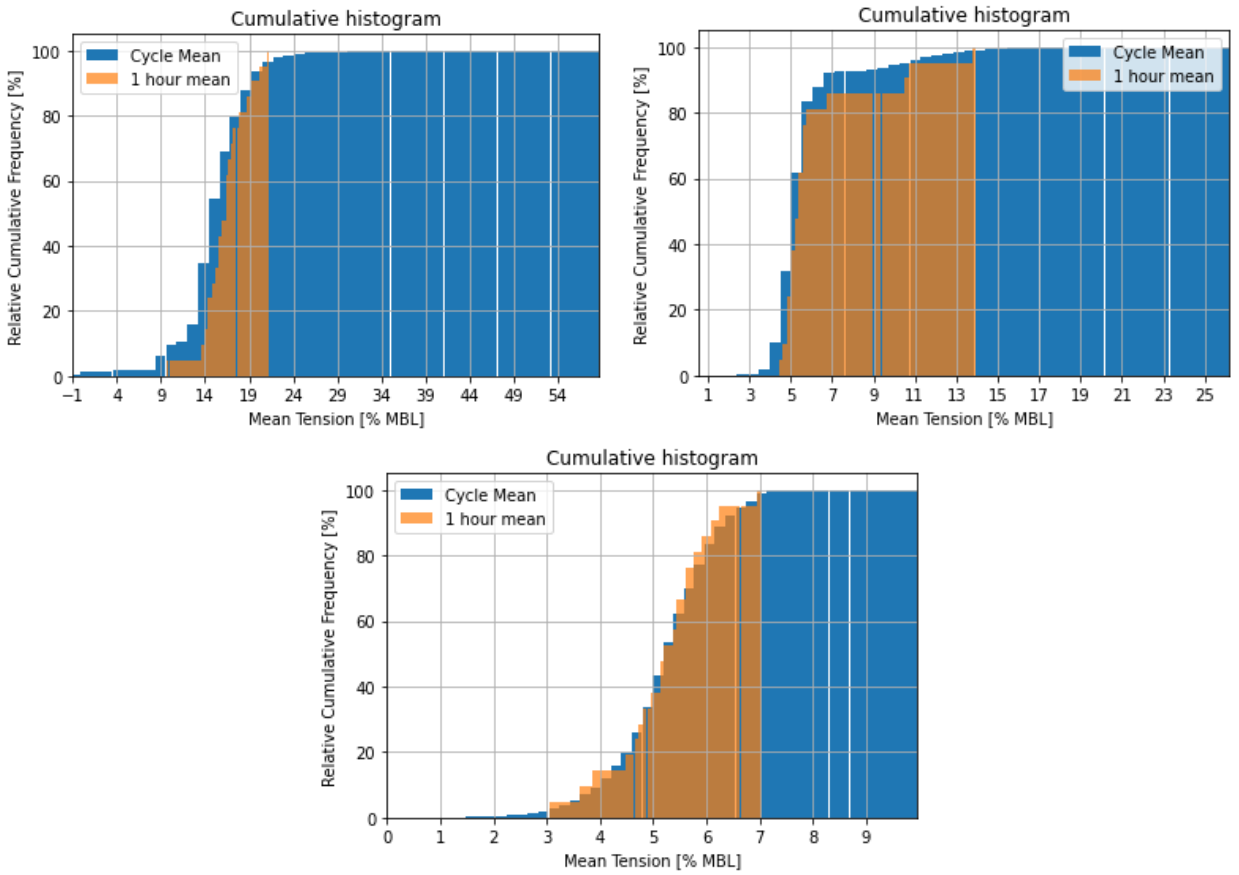

Figure 7.8: Cumulative frequency histogram for 1-hour mean load vs. cycle mean with all sea states accounted for in (a) ML1 (b) ML2 (c) ML3.

7.1.3 Standard deviation and outliers

Contrary to a semi-submersible O&G unit where low frequency tension variations are small compared to a 3-hour mean [19], the low frequency tensions seem to vary more for exposed mooring lines on a FOWT.

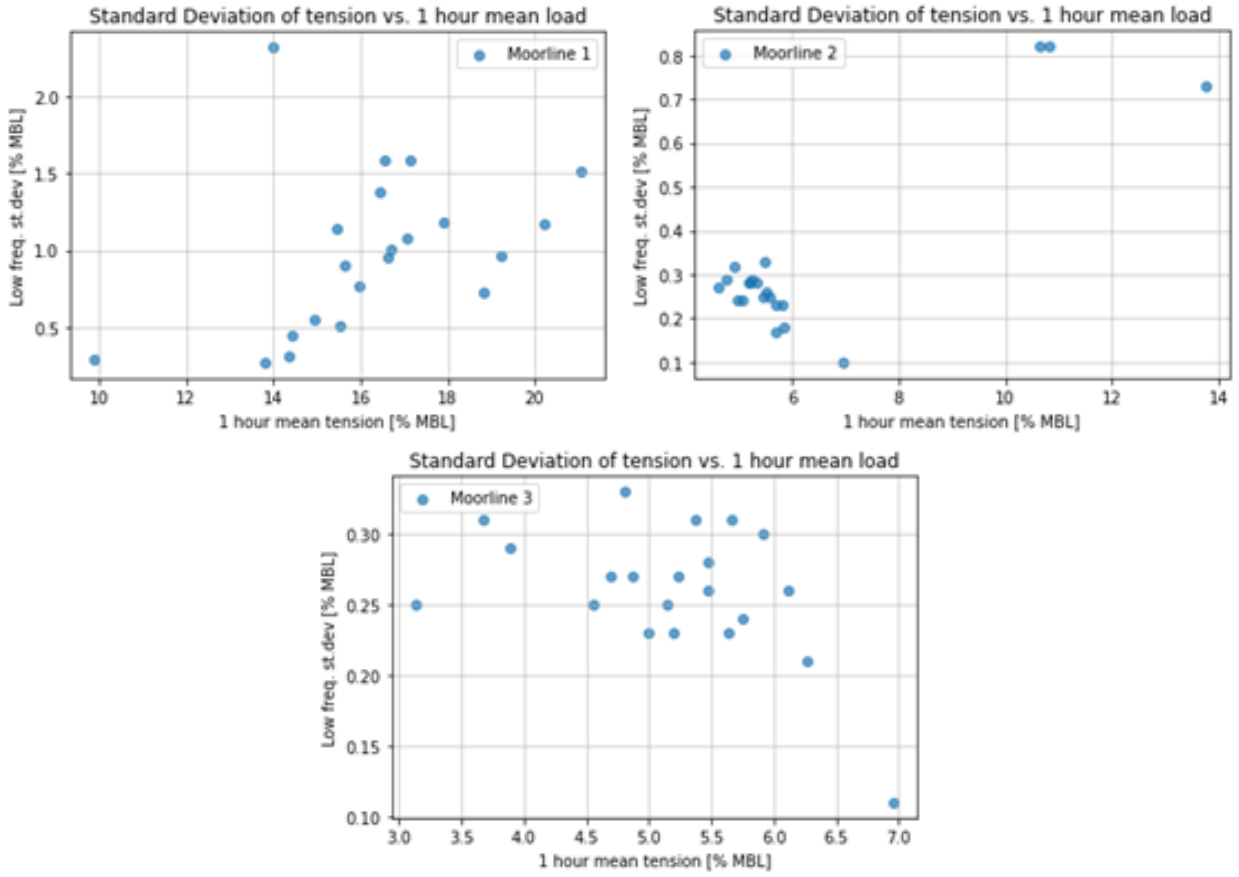

Figure 7.9: Low frequency standard deviation of tension vs. 1-hr mean load for (a) ML1 (b) ML2 (c) ML3.

For ML1 the standard deviation plot in Figure 7.9 shows a greater dispersion of the set of data, compared to the other two lines. The greater dispersion of data, the greater the magnitude of the deviation is, thus a higher deviation from their means. This can also be seen for ML2 for higher % MBL, where the points correspond to extreme sea states, initially indicating that those sea states are predominately influenced by wave-frequent energy. This is further supported by Figure 6.6, which shows the energy distribution for DLC 21. Deviation can also be found for lower mean tensions in ML3. Due to the wind turbine's eccentric locating on the platform and application of turbulent winds, a yaw-moment is created resulting in torsion of the mooring system. As a result, higher mean values can be seen for ML2 in severe sea states, and correspondingly lower mean tensions for ML3.

7.2 Accumulated fatigue damage

The accumulated fatigue damage presented in this thesis is based on the three methods presented in chapter 5.5. An overview of numerical results is presented in appendix E.1 and depicts the mean loads, accumulated fatigue damage both with and without the probability of occurrence, based on each sea state. As expected, the mooring line fatigue damage increases with an increase in significant wave height. However, the highest accumulated damage occurs for sea states with higher wind speeds.

7.2.1 Accumulated fatigue damage ratio

Accumulated fatigue damage for all design load cases based on the standard design curve (DNVGL-OS-E301) is shown in Figure 7.10, where the ratio describes the % of damage summed up for all load cases for ML1. ML1 points towards the dominating environmental direction and is highly exposed to large motions, thus it is the most critical line to fatigue damage. A softer tension characteristic can be seen for ML2 and ML3, positioned 120° opposite the incoming environment. Furthermore, ML2 accumulates 5.3 % and ML3 accumulates 2.6 %, respectively, compared to the total damage in ML1.

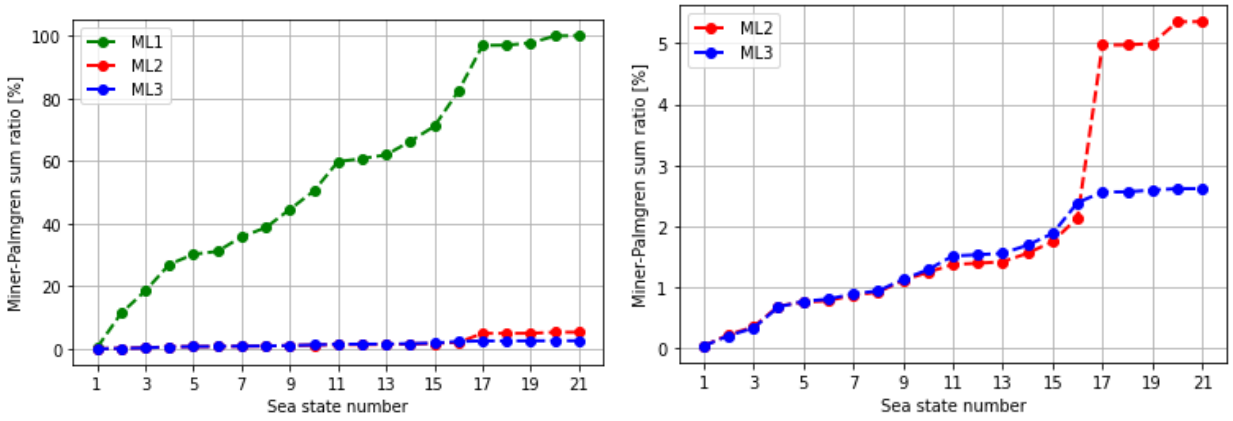

Figure 7.10: Accumulated fatigue damage ratio using design curve from DNVGL-OS-E301 [11], in % of damage at the end of period for ML1 (a). Right figure is zoomed in at ML2 and ML3 (b).

Accumulated fatigue damage ratio obtained with cycle mean load correction for the different mooring lines is shown in Figure 7.11. As expected, ML1 yields the highest fatigue damage being positioned directly towards the dominating wave direction. With this method, ML2 and ML3 are seen to accumulate less than 2 % of the total damage compared to ML1.

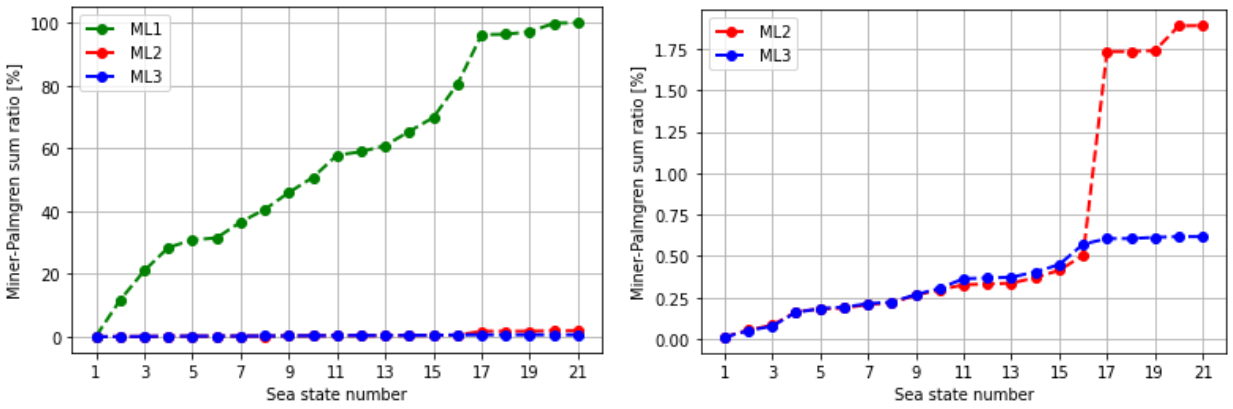

Figure 7.11: Accumulated fatigue damage ratio using SWT-curve with cycle mean, in % of damage at the end of period for ML1 (a). Right figure is zoomed in at ML2 and ML3 (b).

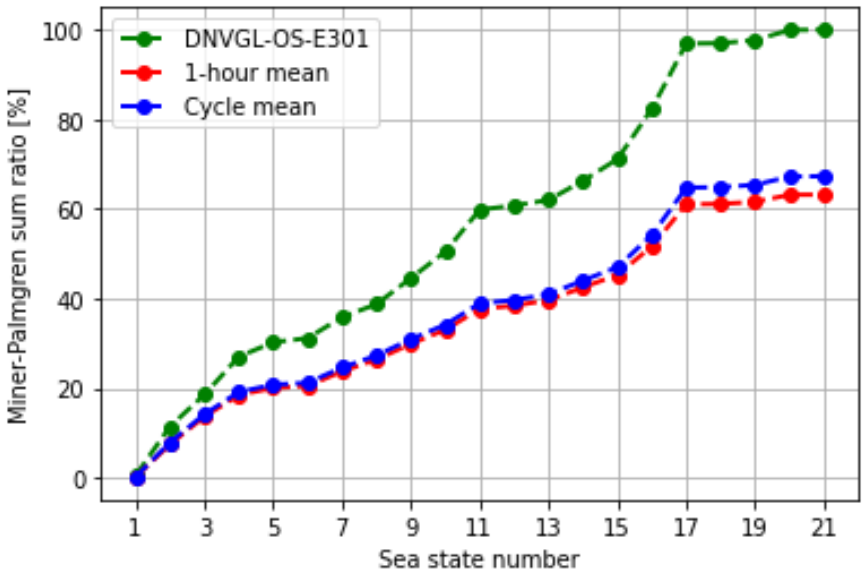

Figure 7.12: Accumulated fatigue damage ratio with and without mean load correction for ML1.

Accumulated fatigue damage ratio obtained with standard design curve (DNVGL-OS-E301) is compared to those based on 1-hour mean load and cycle mean load in Figure 7.12. The fatigue damage is highest without mean load correction, and damage with a mean load correction is close to 60 % of the accumulated fatigue damage for the standard design curve. As expected from the cumulative frequency histograms in chapter 7.1.2, mean load correction based on 1-hour mean load yield similar results as correction based on cycle mean. However, the cycle mean seems to be slightly above the 1-hour mean. The differences between the approaches are discussed in chapter 7.2.3. Nonetheless, the two correction methods seem to agree quite well throughout the sea states, with a noticeable discrepancy starting at sea state number 17. This is the first extreme sea state where high wind loads characterize the environment, together with larger fluctuations in the mean tensions and an

increased yaw angle. The 1-hour mean does not account for this, hence the slight difference. Similar figures are shown for ML2 and ML3 in E.2.

The requirements for DFF for the mooring lines follow consequence class 1. If a proposed safety factor of DFF = 5 is applied, the expected fatigue life becomes:

Table 7.1: Expected fatigue life (years).

ML number	**DNVGL-OS-E301**	**1-hour mean**	**Cycle mean**
ML1	1.2	1.9	1.8
ML2	22.3	90.0	93.8
ML3	45.6	287.0	287.3

It is possible to detect a significant reduction of expected fatigue lifetime when using mean stress correction methods, as seen in Table 7.1. The difference between ML2 and ML3 is explained in chapter 7.1.3. Moreover, it is seen that ML1 yields less than 20 year fatigue life, which is notably less the recommended design fatigue life of 20 years [57]. As mentioned in chapter 5.5.1, standards are recommending to avoid counting all unclosed cycles. By applying this method to the stress range and mean tension, the fatigue life is increased, as seen in Table 7.2. Still, the fatigue life for ML1 is lower than 20 years for all proposed mean counting methods.

Table 7.2: Expected fatigue life (years), without unclosed cycles.

ML number	**DNVGL-OS-E301**	**1-hour mean**	**Cycle mean**
ML1	1.4	2.2	2.1
ML2	26.2	104.7	108.6
ML3	55.0	345.8	346.0

Evaluation of preliminary calculations on an increased chain diameter without unclosed cycles gives increased fatigue life, shown in Table 7.3. By application of 1-hour mean or cycle mean, the requirement of 20 year service life is satisfied, however, the standard design curve does not.

Table 7.3: Expected fatigue life (years), without unclosed cycles with a diameter $d = 200$ mm.

ML number	**DNVGL-OS-E301**	**1-hour mean**	**Cycle mean**
ML1	19.2	26.8	27.4
ML2	347.8	1 387.7	1 439.6
ML3	729.8	4 584.9	4 587.8

7.2.2 Cumulative histograms and damage contribution

Figure 7.13 shows accumulated fatigue damage for 1-hour mean compared with the corresponding 1-hour mean tension.

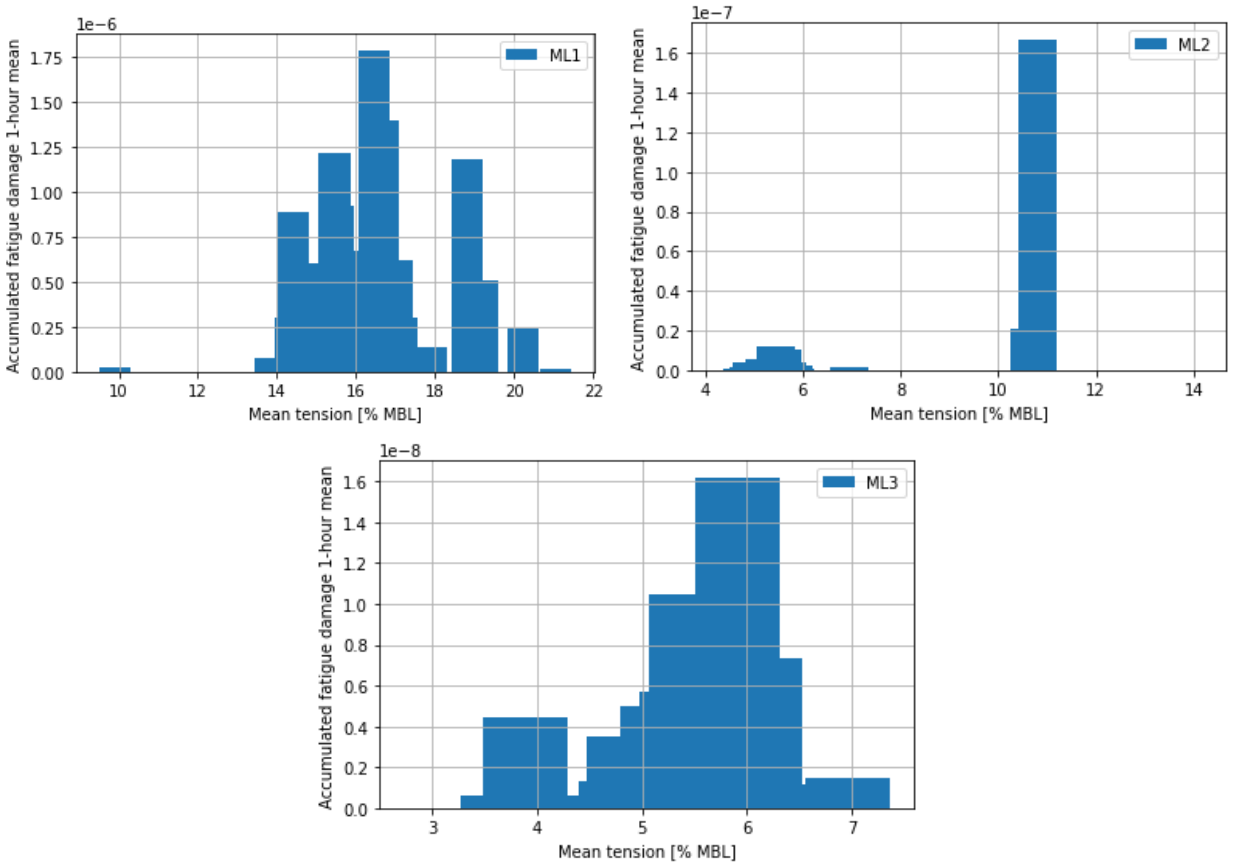

Figure 7.13: Accumulated fatigue damage vs. 1-hour mean tension for (a) ML1 (b) ML2 (c) ML3.

Cumulative histograms for 1-hour mean loads are shown in Figure 7.14, where the frequency of occurrence is compared to the fatigue damage contribution from associated cycles. For ML3, damage contribution is shifted towards mean loads located around 6 % MBL, meaning that fatigue is mostly accumulated in sea states with mean loads above average. This is confirmed by Figure 7.13, where most of the fatigue damage is accumulated around 6 % MBL. The opposite effect is seen for ML2, as damage accumulation is shifted towards cycles associated with a 1-hour mean below average. In addition, it is seen that most of the fatigue damage for ML1 is explained by mean loads less than 18 % MBL.

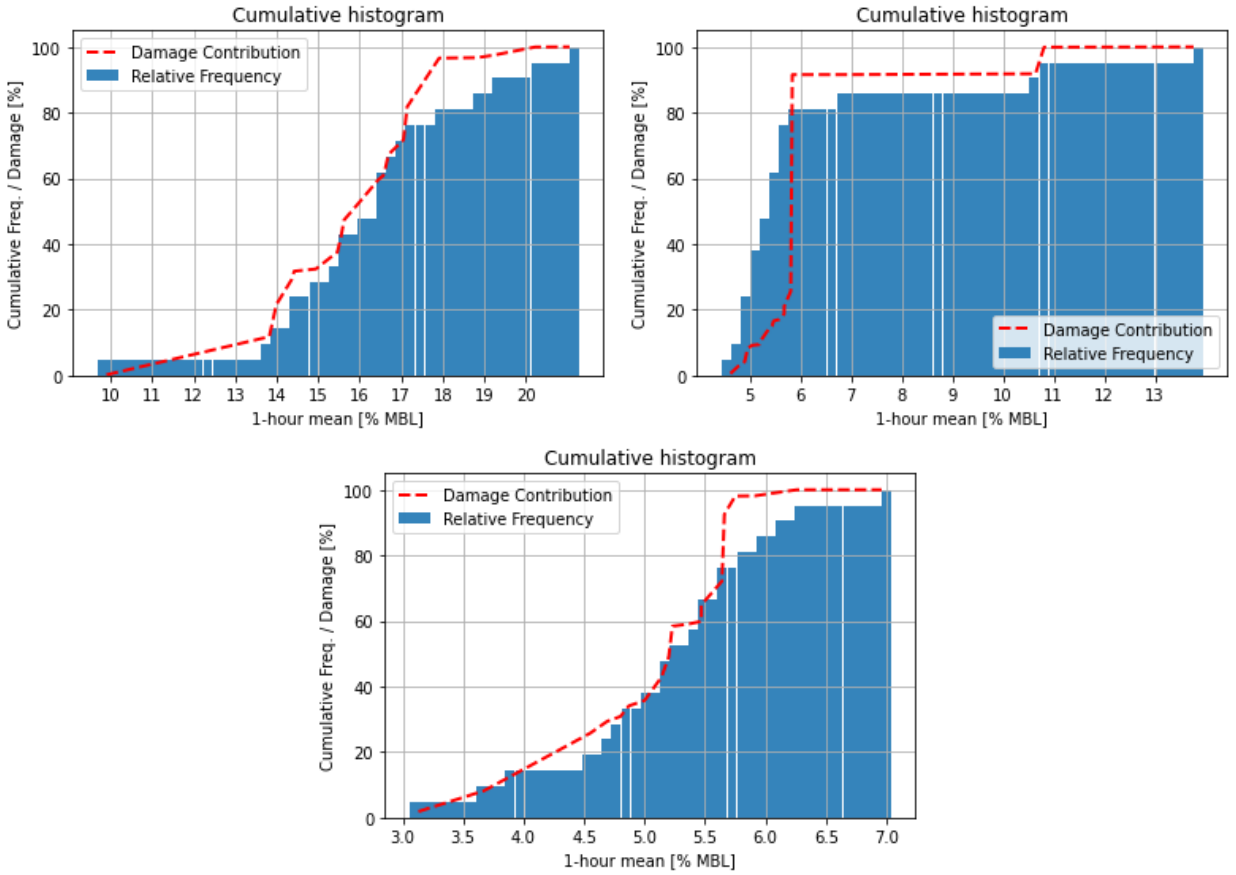

Figure 7.14: Cumulative histograms for 1-hour mean load: Relative frequency and damage contribution for (a) ML1 (b) ML2 (c) ML3.

7.2.3 Single Correction Factor

In this section, the obtained results from the single correction factor method presented in chapter 4.2.2 are discussed. Results with and without the three roughest sea states are also presented. Table 7.4 describes a comparison of the results between the total accumulated fatigue damage based on the standard design curve and with mean load correction. As expected, ML1 experiences the highest mean and accumulated fatigue damage loads due to its location facing the winds and waves during power production. Thus, the ratio is a lot higher than ML2 and ML3.

Table 7.4: Ratio of fatigue damage obtained with mean load correction to damage with standard design curve.

Mooring line	Cycle mean	1-hour mean	Pre-tension
1	0.6728	0.6318	0.2243
2	0.2377	0.2480	0.2243
3	0.1588	0.1589	0.2243

Interestingly, both cycle mean and 1-hour mean for ML2 are seen to be higher than ML3. However, by investigating Table 7.5, which does not contain the three roughest sea states, the ratios are fairly close to each other. ML2 experiences a dominating heave resonance in this state due to an extreme wave period, that will affect the fatigue life. Conversely, ML3 experiences lower mean loads for the extreme sea states accumulate less fatigue damage. Nevertheless, ML2 and ML3 have almost the same ratio, slightly lower than the pre-tension as overall mean load levels are below the pre-tension mean load.

Table 7.5: Ratio of fatigue damage obtained with mean load correction to damage with standard design curve without the three roughest sea states.

Mooring line	**Cycle mean**	**1-hour mean**	**Pre-tension**
1	0.6591	0.6277	0.2243
2	0.1587	0.1588	0.2243
3	0.1611	0.1612	0.2243

Table 7.6: Ratio of mean load correction by 1-hour mean and pre-tension to mean load correction using cycle mean.

Mooring line	**1-hour mean**	**Pre-tension**
1	1.0649	2.9996
2	0.9586	1.0599
3	0.9989	0.7078

Table 7.6 explains the difference between the approaches as a ratio of mean load correction by 1-hour mean and pre-tension to cycle mean loads. It depicts that the cycle mean and the 1-hour mean agree fairly well for all lines, with less than 6.5 % underestimation of fatigue damage as the most deviating results, corresponding to ML1. Further, it shows that the mooring lines with the highest accumulated fatigue damage and % MBL experience the most deviation from the cycle mean results, explained by the small sample size. Moreover, correction based on pre-tension gives largely deviating results as the effect of environmental loads is not considered, especially for ML1. In addition, the pre-tension for all lines is the same and does not consider environmental impact, reducing the responses of the platform to an acceptable level. For ML1, fatigue damage is extremely underestimated by close to 200 % compared to correction based on actual mean loads. For ML2 and ML3, fatigue damage is correspondingly overestimated by 30 % in Table 7.7.

Table 7.7: Ratio of mean load correction by 1-hour mean and pre-tension to mean load correction using cycle mean without the three roughest sea states.

Mooring line	**1-hour mean**	**Pre-tension**
1	1.0500	2.9384
2	0.9994	0.7074
3	0.9995	0.7183

8 Conclusion

The objective of this thesis was to investigate the mean tension dependency for the mooring lines of a semi-submersible floating offshore wind turbine. By application of different mean load corrections based on 1-hour mean loads, cycle mean loads, and pre-tensioning, a significant reduction of calculated damage has been observed for a floating offshore wind turbine. For ML1, a potential of 37 % reduction is observed, with the use of a parametrized intercept parameter. ML2 and ML3 have a potential reduction of 75 % and 84 % respectively.

It is important to not account for mean load alone when assessing the remaining fatigue capacity of mooring chains. This is due to the complexity of the phenomena, and other external influences, such as corrosion pits and OPB contributing negatively to the fatigue life.

Further, it has been shown that environmental loads influencing the mooring lines and their orientation towards wind and waves are of great importance. ML1 is the most exposed line, thus the highest fatigue damage is accumulated in this line, compared to ML2 and ML3. Since unidirectional wind and the same level of pre-tension for all lines are equal, the accumulated damage in the lines opposite of the main wave direction yields significantly lower fatigue damage, and at the same time a longer fatigue life. Accumulated fatigue damage in ML2 and ML3 is less than 6 % and 3 %, compared to total accumulated damage for ML1. If multi-directional wind and wave loads would have been considered, the differences between the mooring lines may even out. To design the mooring system for a 20 year lifetime at this particular site, a second mooring line could be added in the wind direction, if the unidirectional wind is applied. Additionally, the mooring lines may be split into two separate lines, forming a bridle, attached to the fairlead. This will ultimately provide increased yaw stiffness. Otherwise, it is recommended to include wind from several directions to reduce the fatigue damage on ML1. Another factor could be to increase the chain diameter, as this will increase the fatigue lifetime.

Results obtained from 1-hour mean load as a basis for the mean load correction, show a slight difference to the cycle mean load correction. However, it is seen that the higher accumulated damage yielded in the mooring line, the larger is the difference between the methods. This may be explained by the level of pre-tension being equal to all lines, neglecting environmental conditions. In addition, the low-frequency tensions seem to vary more for exposed mooring lines. The mean load correction methods are still within reasonable resemblance, even as the sample size of the 1-hour mean is significantly lower than the cycle mean. The utilized rainflow counting algorithm

in Python accounted for all cycles, despite being half-cycles. As a result, some high regime mean loads occurred in the data, inevitably increasing the cumulative histogram range for cycle means and causing deviations in the accumulated fatigue damage. Further, it has been found that by neglecting these unclosed cycles, the fatigue life is increased by an additional 15 % for ML1.

Using pre-tension as a preliminary evaluation method is quite risky, as the probability of yielding incorrect results is fairly high for a FOWT. It is fair to assume that the method does not provide a quick and simple estimate of the mean load correction. Compared to mean load correction based on cycle mean, fatigue damage is underestimated for ML1 and ML2 and overestimated for ML3.

The obtained results from all simulations clearly show that most of the mean load distribution is explained below the typical mean load of 20 % MBL. In addition, very little damage is accumulated above this value, indicating a need for a new design approach with mean tension correction. This would deliver more optimized S-N design curves with a more unified level of reliability for FOWT. Similar methods would also be applicable for all types of floating units with a need for mooring.

9 Recommendations for future work

Based on the findings of the work presented in this thesis, recommendations for future work are as follows:

- Line tension results presented for ML1 (windward line), have verified it to be the most loaded line for all sea states. However, alternative wind directions are not discussed, nor simulated. It is recommended to use multi-directional wind instead. That is due to realistic levels of wind, wave, and current being stochastic. If it would have been applied, a more distributed fatigue damage would be expected for the mooring lines, and ML1 would most likely not be as exposed.

- Application of different levels of pre-tensioning in the lines. Higher mean loads would still be expected on the windward side compared to the leeward side, however, with an optimized pre-tension in all lines, other values may occur. This should be done with multi-directional winds.

- The parametrized S-N design curve applied in this thesis has not been validated by fatigue tests on mooring chains in the high mean load regime. Therefore, more tests must be performed in that range. In addition, testing different chain grades and diameters under the same absolute mean tensions would be desirable. It may lead to different design curves for different grades.

- To have a more realistic assessment of the fatigue damage in the mooring lines, the effect of corrosion pits forming on the chain surface must also be accounted for as this is highly detrimental to fatigue life.

- In this thesis, a semi-submersible platform was analyzed. Since this procedure only has been done on a semi-submersible O&G unit previously,several floating concepts exist, as well as other mooring techniques. Other concepts may lead to different results, and a lot more work in this field is possible.

- A fatigue analysis on the polyester lines has not been considered in this thesis, since low tension fatigue is usually not considered an issue for such a material [11]. However, it would be interesting to see how the polyester part of the mooring lines would be affected if subjected to FLS or ULS.

- A larger statistical sample in seeds would increase the number of random phase angles in wave/wave realization. This may be influential to the fatigue damage calculations and their statistical significance thus may be evaluated at a later stage.

References

[1] J. Fernandez, A. Arredondo, W. Storesund, and J. J. Gonzalez, "The Influence of the Mean Tension on The Fatigue Performance of Mooring Chains," *Offshore Technology Conference*, Apr. 2019.

[2] D. Roddier and J. Weinstein, "Floating wind turbines," *mechanical engineering*, vol. 132, no. 04, pp. 28–32, 2010.

[3] M. K. Al-Solihat and M. Nahon, "Stiffness of slack and taut moorings," *Ships and Offshore Structures*, vol. 11, pp. 890–904, 10 2016.

[4] C. Krugerud, "Design and Automated Optimization of Mooring Systems for Shallow Water and Harsh Environments," Master's thesis, NTNU, 2016.

[5] J. F. Manwell, J. G. McGowan, and A. L. Rogers, *Wind energy explained: theory, design and application*. John Wiley & Sons, 2010.

[6] Y. Guo, R. Damiani, and W. Musial, "Simulating Turbulent Wind Fields for Offshore Turbines in Hurricane-Prone Regions (Poster)," Apr. 2014. https://www.osti.gov/biblio/1130129.

[7] L. Eliassen, *Aerodynamic loads on a wind turbine rotor in axial motion*. PhD thesis, University of Stavanger, Norway, 2015.

[8] "Random waves and wave statistics," H. E. Krogstad, Ø. A. Arntsen, NTNU, Trondheim, Feb. 2000.

[9] "Hydrodynamics of Offshore Structures," S. K. Chakrabarti, CBI Industries, Inc., Illinois, June 1987.

[10] H. K. H. Olafsen, "Control of Thruster Assisted Position Mooring System on Floating Production Storage and Offloading," Master's thesis, Institutt for marin teknikk, 2014.

[11] "Position Mooring," DNVGL-OS-E301, Offshore standards, Det Norske Veritas, Høvik, NO, July 2018.

[12] P. M. Vargas, T.-M. Hsu, and W. K. Lee, "Stress concentration factors for stud-less mooring chain links in fairleads," in *International Conference on Offshore Mechanics and Arctic Engineering*, vol. 37440, pp. 909–917, 2004.

[13] G. Terjesen, "Bok 2," in *Grunnleggende om utmatting av metaller*, ch. 2, pp. 1–65, REALTEK / NMBU, 2020.

[14] SIEMENS, "Mean stress corrections and stress ratios." From *SIEMENS*, https://community.sw.siemens.com/s/article/mean-stress-corrections-and-stress-ratios. Last accessed: 09.02.2021.

[15] C. E. Silva de Souza, P. A. Bertelsen, L. Eliassen, E. E. Bachynski, E. Engebretsen, and H. Haslum, "Definition of the INO WINDMOOR 12 MW base case floating wind turbine," 978-82-7174-407-6, SINTEF Ocean, 1.2 ed., January 2021.

[16] D. K. Spearman and S. Strivens, "Floating Wind Joint Industry Project-Phase II Summary Report," *Carbon Trust, Tech Rep*, vol. 19, pp. 02–20, 2018.

[17] M. I. Kvittem, "WINDMOOR: Optimization of FOWT mooring systems," SINTEF Ocean, A ed., December 2020.

[18] A. Eik, "Hywind tampen - Samfunnsmessige ringvirkninger," February 2019. Multiconsult.

[19] E. N. Lone, B. J. Leira, T. Sauder, V. Aksnes, Ø. Gabrielsen, and K. Larsen, "Influence of Mean Tension on Mooring Line Fatigue Life," in *ASME 2020 39th International Conference on Ocean, Offshore and Arctic Engineering*, American Society of Mechanical Engineers Digital Collection, 2020.

[20] T. Burton, D. Sharpe, N. Jenkins, and E. Bossanyi, "Wind Energy Handbook," John Wiley & Sons, Ltd, 2001.

[21] W. Europe, "Wind Energy in Europe in 2019—Trends and Statistics," *Wind Europe: Brussels, Belgium*, 2020.

[22] W. Europe, "The impact of COVID-19 on Europe's wind sector - Executive Summary," *Wind Europe: Brussels, Belgium*, 2020.

[23] D. Roddier, C. Cermelli, and A. Weinstein, "WindFloat: A Floating Foundation for Offshore Wind Turbines—Part I: Design Basis and Qualification Process," vol. 4, Jan. 2009.

[24] BW Ideol, "An Industry-transforming innovation - Technology." From *BW Ideol*, https://www.bw-ideol.com/en/technology. Last accessed: 10.05.2021.

[25] K.-T. Ma, Y. Luo, T. Kwan, and Y. Wu, "Chapter 15 - Mooring for floating wind turbines," in *Mooring System Engineering for Offshore Structures* (K.-T. Ma, Y. Luo, T. Kwan, and Y. Wu, eds.), pp. 299–315, Gulf Professional Publishing, 2019. From https://www.sciencedirect.com/science/article/pii/B9780128185513000156.

[26] I. Martinez Perez, A. Constantinescu, P. Bastid, Y.-H. Zhang, and V. Venugopal, "Computational fatigue assessment of mooring chains under tension loading," *Engineering Failure Analysis*, vol. 106, Dec. 2019.

[27] "Offshore mooring chain," DNVGL-OS-E302, Offshore standards, Det Norske Veritas, Høvik, NO, July 2018.

[28] Y.-H. Zhang and P. Smedley, "Fatigue Performance of High Strength and Large Diameter Mooring Chain in Seawater," *ASME 2019 38th International Conference on Ocean, Offshore and Arctic Engineering*.

[29] I. Martinez, P. Bastid, A. Constantinescu, and V. Venugopal, "Multiaxial fatigue analysis of mooring chain links under tension loading: Influence of mean load and simplified assessment," p. V003T02A026, Jun 2018.

[30] A. Ince and G. Glinka, "A modification of Morrow and Smith–Watson–Topper mean stress correction models," *Fatigue Fracture of Engineering Materials Structures*, vol. 34, pp. 854–867, Apr 2011.

[31] A. Kvitrud, "Lessons Learned From Norwegian Mooring Line Failures 2010–2013," vol. Volume 4A: Structures, Safety and Reliability of *International Conference on Offshore Mechanics and Arctic Engineering*, 06 2014. V04AT02A005.

[32] Gabrielsen, K. Larsen, O. Dalane, H. B. Lie, and S.-A. Reinholdtsen, "Mean Load Impact on Mooring Chain Fatigue Capacity: Lessons Learned From Full Scale Fatigue Testing of Used Chains," *ASME 2019 38th International Conference on Ocean, Offshore and Arctic Engineering*.

[33] M. I. Kvittem, *Modelling and response analysis for fatigue design of a semi-submersible wind turbine*. PhD thesis, NTNU, 2014. Skipnes Kommunikasjon AS.

[34] D. Quarton *et al.*, "Wind energy generation systems - Part 1: Design requirements," *Bristol, UK: Garrad Hassan and Partners, Ltd*, 2005.

[35] S. Mathew, *Wind energy: fundamentals, resource analysis and economics*. Springer, 2006.

[36] "Design of offshore wind turbine structures," DNV-OS-J101, Offshore standards, Det Norske Veritas, Høvik, NO, Oct. 2010.

[37] "Environmental Conditions and environmental loads," DNVGL-RP-C205, Offshore standards, Det Norske Veritas, Høvik, NO, Oct. 2010.

[38] A. Albani and M. Z. Ibrahim, "Wind Energy Potential and Power Law Indexes Assessment for Selected Near-Coastal Sites in Malaysia," *Energies*, vol. 10, no. 3, 2017.

[39] "Qualification of innovative floating substructures for 10 MW wind turbines and water depths greater than 50 m," LifeS50+, Det Norske Veritas, European Union Horizon 2020, June 2015.

[40] I. Udoh and J. Zou, "Wind spectral characteristics on strength design of floating offshore wind turbines," *Ocean Systems Engineering*, vol. 8, pp. 281–312, Sept. 2018.

[41] J. Twidell, *Renewable energy resources*. Routledge, 2006.

[42] G. B. Rossi, F. Crenna, V. Piscopo, and A. Scamardella, "Comparison of Spectrum Estimation Methods for the Accurate Evaluation of Sea State Parameters," *Sensors*, vol. 20, no. 5, p. 1416, 2020.

[43] T. Moan, Z. Gao, E. E. Bachynski, and A. R. Nejad, "Recent Advances in Response Analysis of Floating Wind Turbines in a Reliability Perspective," in *International Offshore Wind Technical Conference (IOWTC)*, 2018.

[44] O. Faltinsen, *Sea loads on ships and offshore structures*, vol. 1. Cambridge university press, 1993.

[45] NOAA, "What is a current?." From *National Ocean Service*, https://oceanservice.noaa.gov/about/welcome.html#cite. Last accessed: 08.02.2021.

[46] W. Cummins, "The impulse response function and ship motions," tech. rep., David Taylor Model Basin Washington DC, 1962.

[47] "Global performance analysis of deepwater floating structures," DNVGL-RP-F205, Offshore standards, Det Norske Veritas, Høvik, NO, Oct. 2010.

[48] I. Lotsberg, *Fatigue Design of Marine Structures*. Cambridge University Press, 2016.

[49] S.-P. Zhu, Q. Lei, H.-Z. Huang, Y.-J. Yang, and W. Peng, "Mean stress effect correction in strain energy-based fatigue life prediction of metals," *International Journal of Damage Mechanics*, vol. 26, no. 8, pp. 1219–1241, 2017.

[50] N. E. Dowling, "Fatigue Failure Predictions for Complicated Stress-Strain Histories," *National Technical Information Service*, vol. Department of Technical and Applied Mechanics, no. 337, 1971.

[51] Y.-L. Lee and T. Tjhung, "Chapter 3 - Rainflow Cycle Counting Techniques," in *Metal Fatigue Analysis Handbook* (Y.-L. Lee, M. E. Barkey, and H.-T. Kang, eds.), pp. 89–114, Boston: Butterworth-Heinemann, 2012. https://www.sciencedirect.com/science/article/pii/B9780123852045000033.

[52] A. Antonopoulos, S. DrArco, M. Hernes, and D. Peftitsis, "Challenges and Strategies for a Real-Time Implementation of a Rainflow-Counting Algorithm for Fatigue Assessment of Power Modules," pp. 2708–2713, Mar. 2019.

[53] American Society of Testing Materials (ASTM), "Standard practices for cycle counting in fatigue analysis," *ASTM E1049-85, West Conshohocken, PA*, 2005.

[54] O. A. Hermundstad, "SIMA." From https://www.sintef.no/en/software/sima/. Last accessed: 04.02.2021.

[55] "Rainflow project description." From https://pypi.org/project/rainflow/. Last accessed: 10.05.2021.

[56] "Welcome to QATS's documentation." From https://qats.readthedocs.io/en/latest/index.html. Last accessed: 19.04.2021.

[57] A. L. H. Hopstad, K. Argyriadis, A. Manjock, J. Goldsmith, and K. O. Ronold, "DNVGL Standard for Floating Wind Turbines, DNVGL-ST-0119," in *ASME 2018 1st International Offshore Wind Technical Conference*, American Society of Mechanical Engineers Digital Collection, 2018.

[58] SINTEF, "Advanced Wave and Wind Load Models for Floating Wind Turbine Mooring System Design." From https://www.sintef.no/projectweb/windmoor/. Last accessed: 04.02.2021.

[59] X. Zhang, N. Noel, G. Ferrari, and M. Hoogland, "Corrosion behaviour of mooring chain steel in seawater," in *The 67th annual meeting of the International Society of Electrochemistry, 21-26 August 2016, The Hague, The Netherlands, 1-15*, 2016.

[60] E. P. Zarandi, *Multiaxial fatigue analysis of offshore mooring chains, considering the effects of residual stresses and corrosion pits*. PhD thesis, NTNU, 2020.

[61] D. Quarton *et al.*, "An international design standard for offshore wind turbines: IEC 61400-3," *Bristol, UK: Garrad Hassan and Partners, Ltd*, 2005.

[62] G. Marsh, C. Wignall, P. R. Thies, N. Barltrop, A. Incecik, V. Venugopal, and L. Johanning, "Review and application of Rainflow residue processing techniques for accurate fatigue damage estimation," *International Journal of Fatigue*, vol. 82, pp. 757–765, 2016.

[63] "Coupled analysis of floating wind turbines," DNVGL-RP-0286, Offshore standards, Det Norske Veritas, Høvik, NO, 2019.

[64] T. Finch, "Incremental calculation of weighted mean and variance," *University of Cambridge*, vol. 4, no. 11-5, pp. 41–42, 2009.

[65] B. Yu, D. Gabriel, L. Noble, and K.-N. An, "Estimate of the Optimum Cutoff Frequency for the Butterworth Low-Pass Digital Filter," *Journal of applied biomechanics*, vol. 15, pp. 319–329, 08 1999.

A Wind Turbine Performance Curves

A.1 Rotor Speed

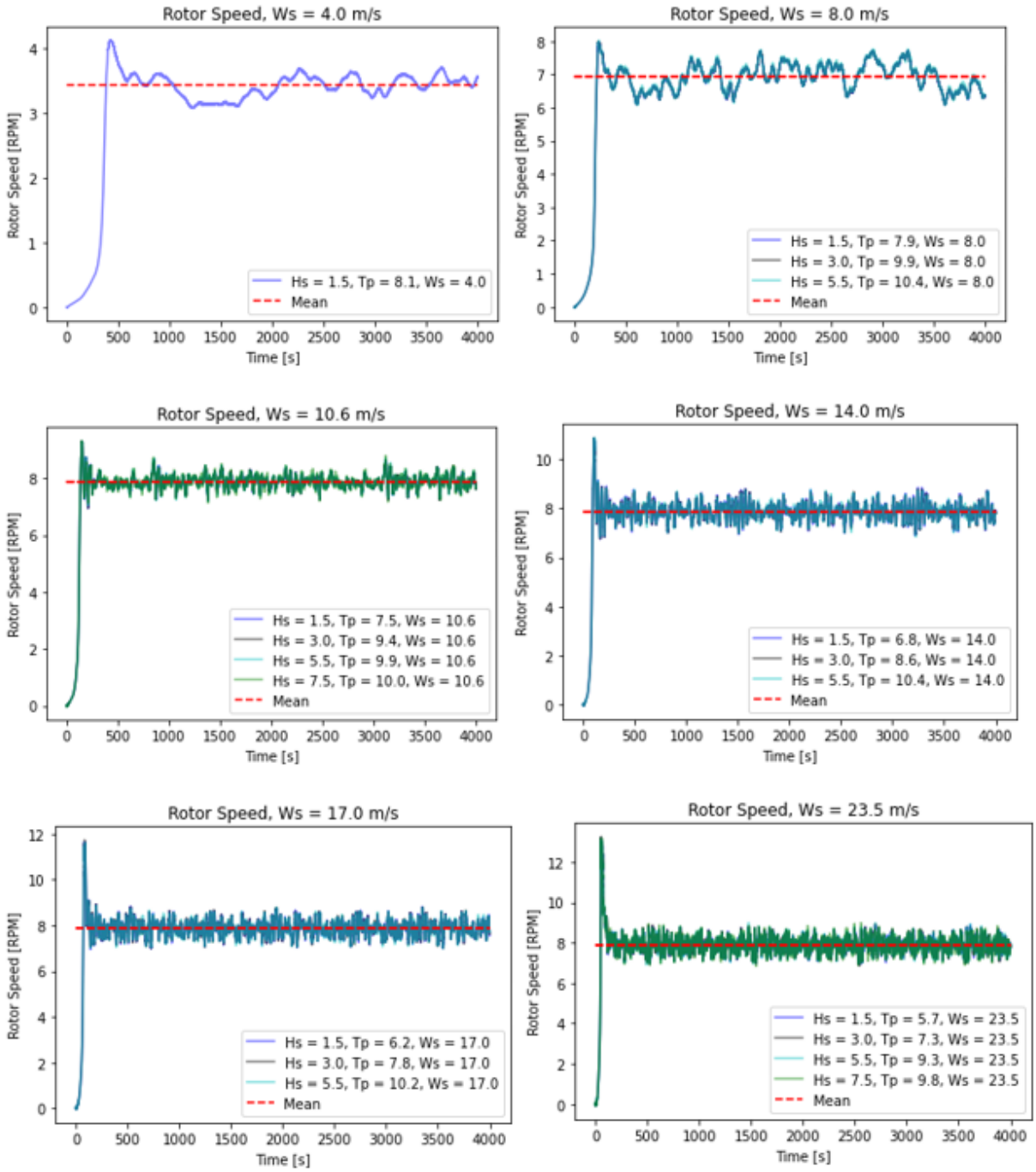

Figure A.1: Rotor Speed Performance time series.

A.2 Thrust Force

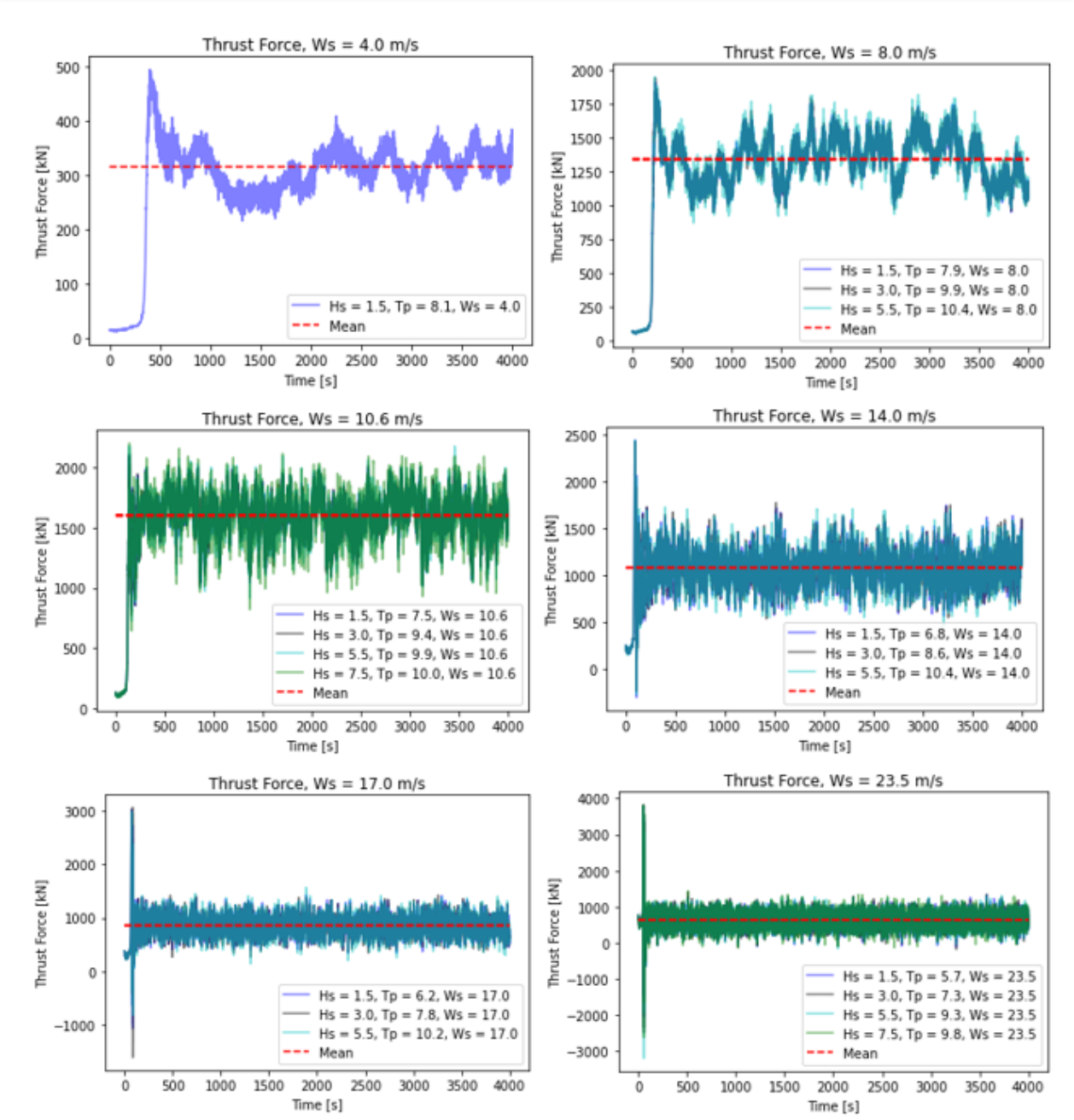

Figure A.2: Thrust Force Performance time series.

A.3 Collective Blade Pitch

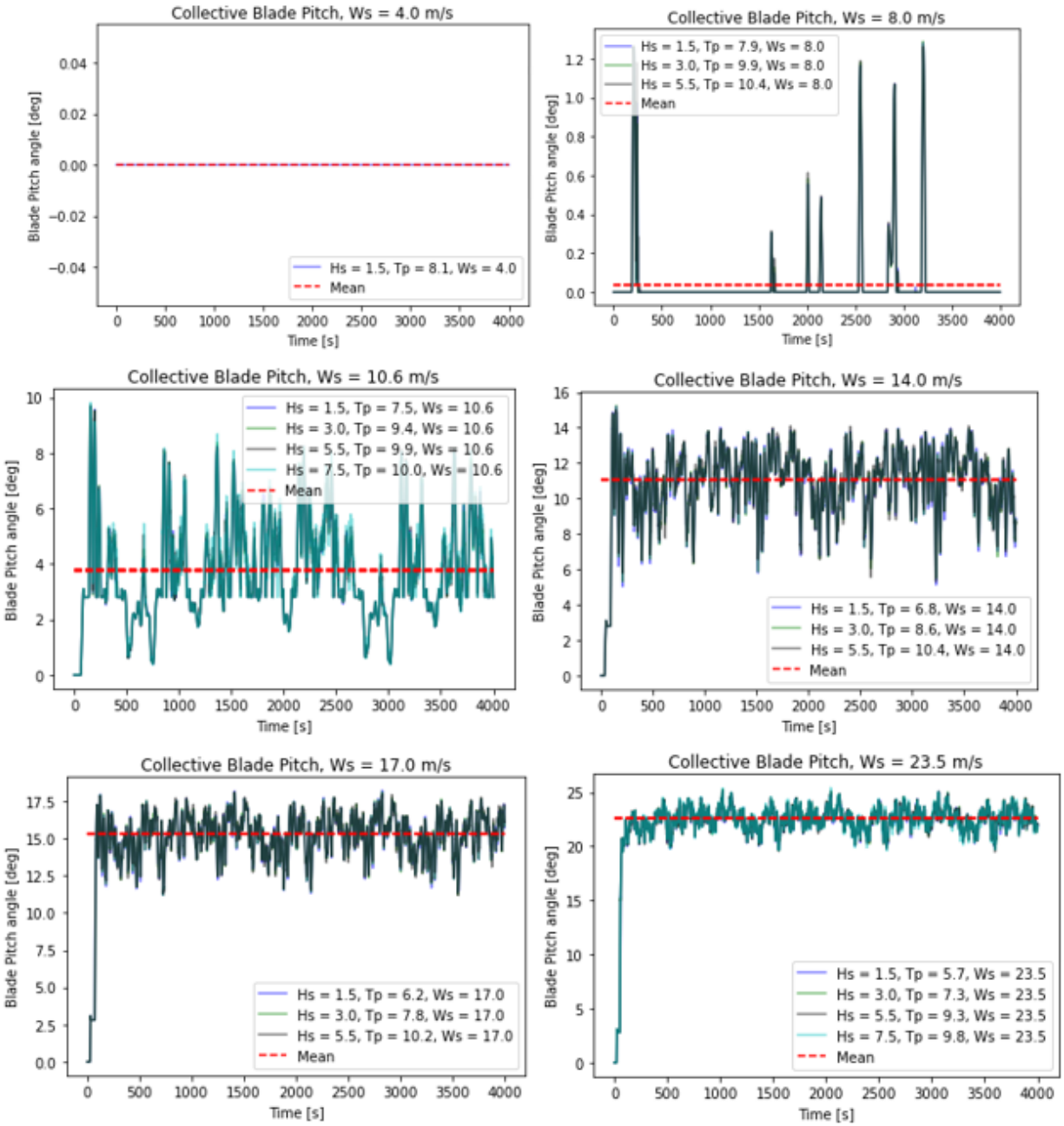

Figure A.3: Collective Blade Pitch Performance time series.

A.4 Generator Power Output

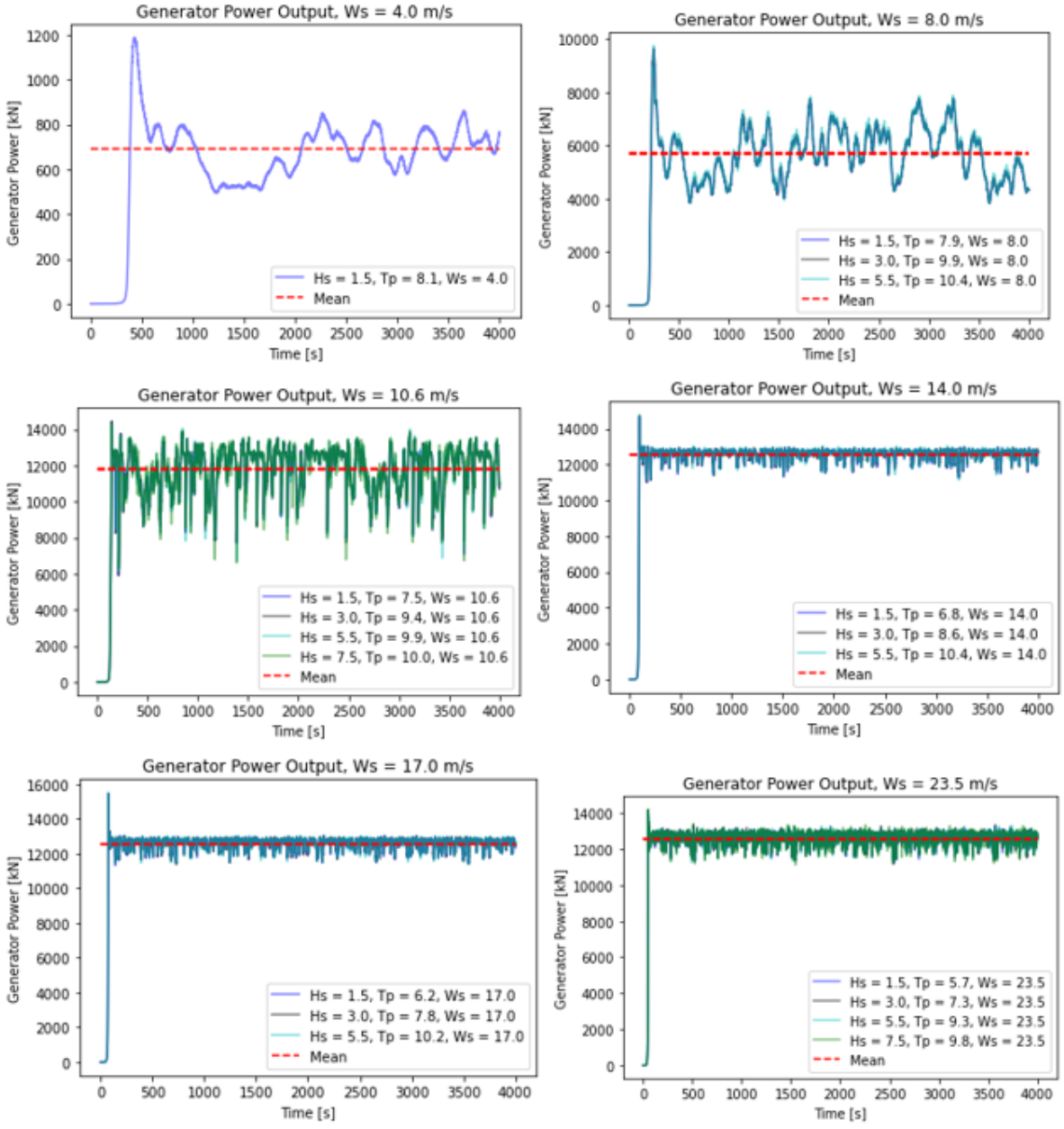

Figure A.4: Generator Power Performance time series.

B Wind Turbine Performance Curves - Extreme

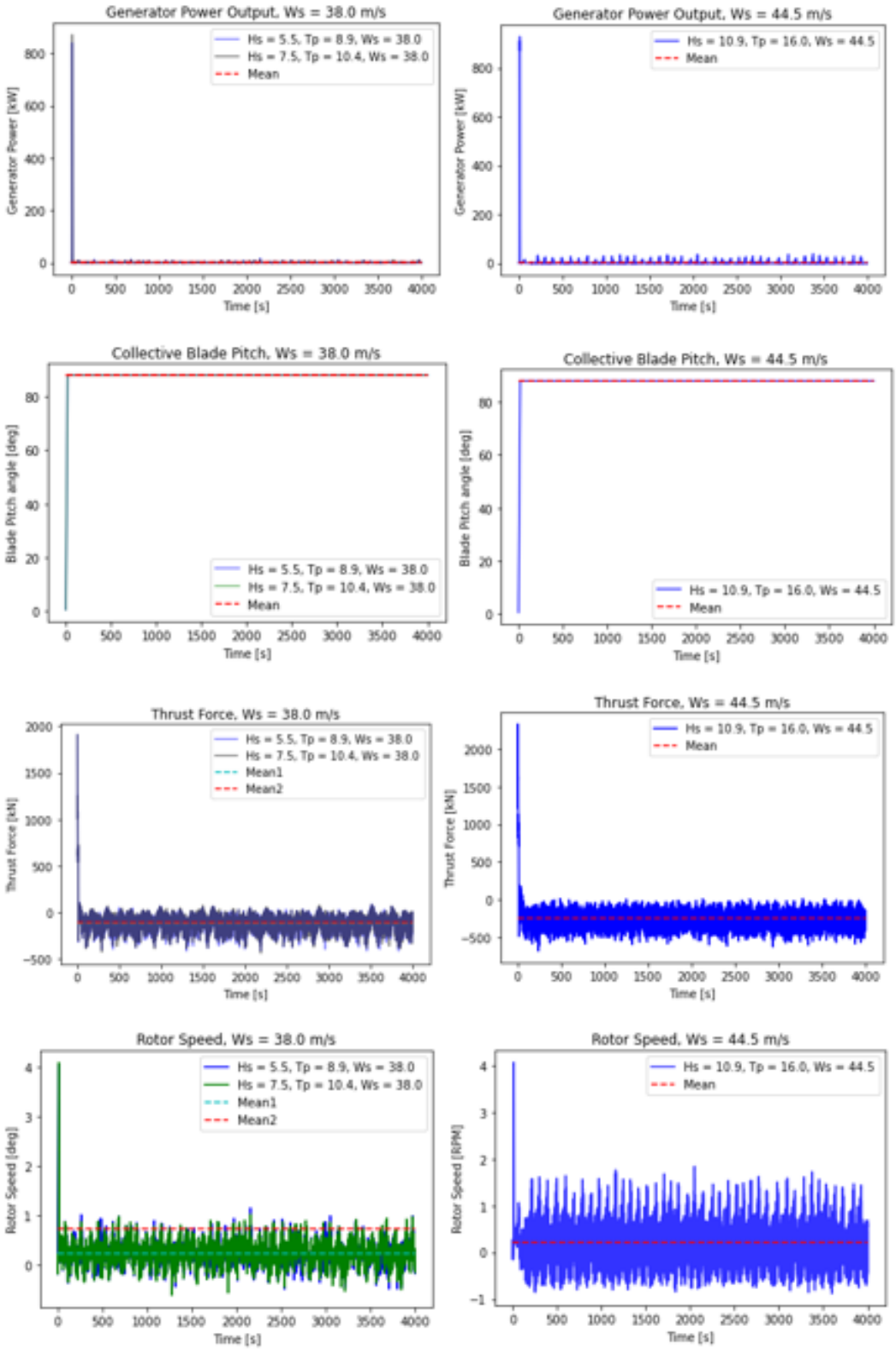

Figure B.1: Wind Turbine Performance curves for extreme response.

C Motion response spectrum

In the following, motion response spectra for four conditions are evaluated; surge, heave, pitch and yaw. That is for the three different design load cases chosen in chapter 6.3. In addition, filtered time series axial force plots in the fairlead and power spectral density plots of line tensions are shown.

C.1 Design Load Case 1

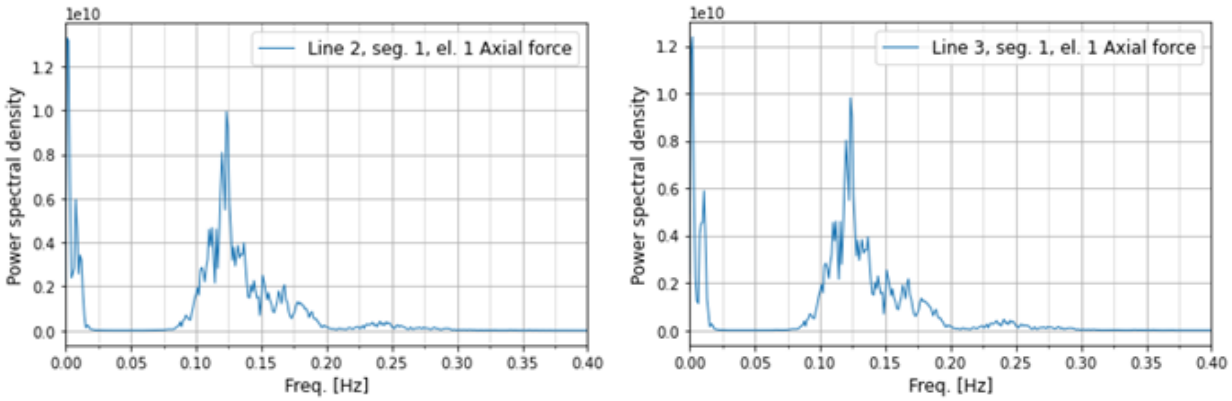

Figure C.1: PSD of line tension in DLC 1 for (a) ML2 (b) ML3.

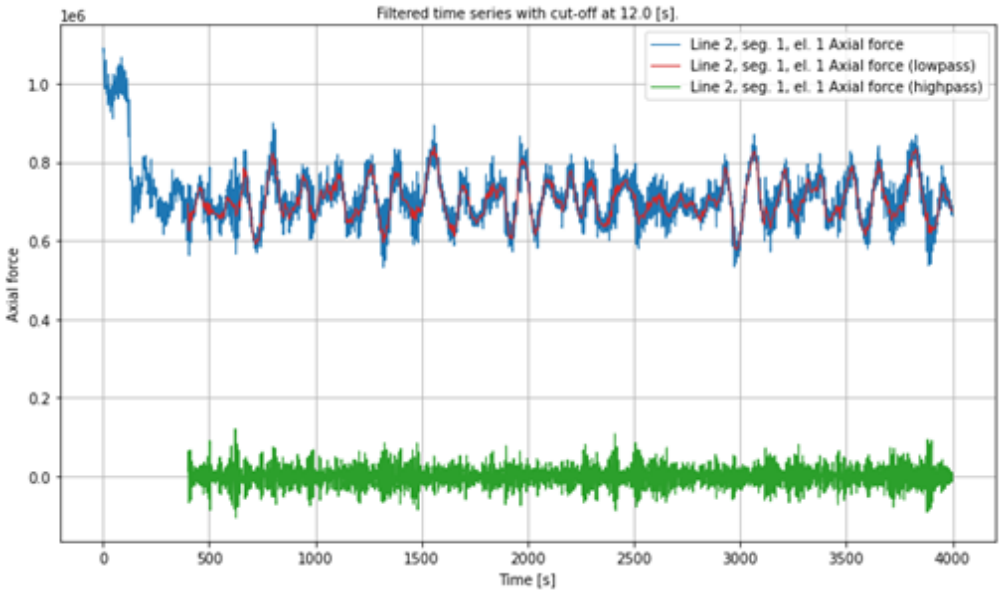

Figure C.2: Filtered time series for axial force of ML2 - DLC 1.

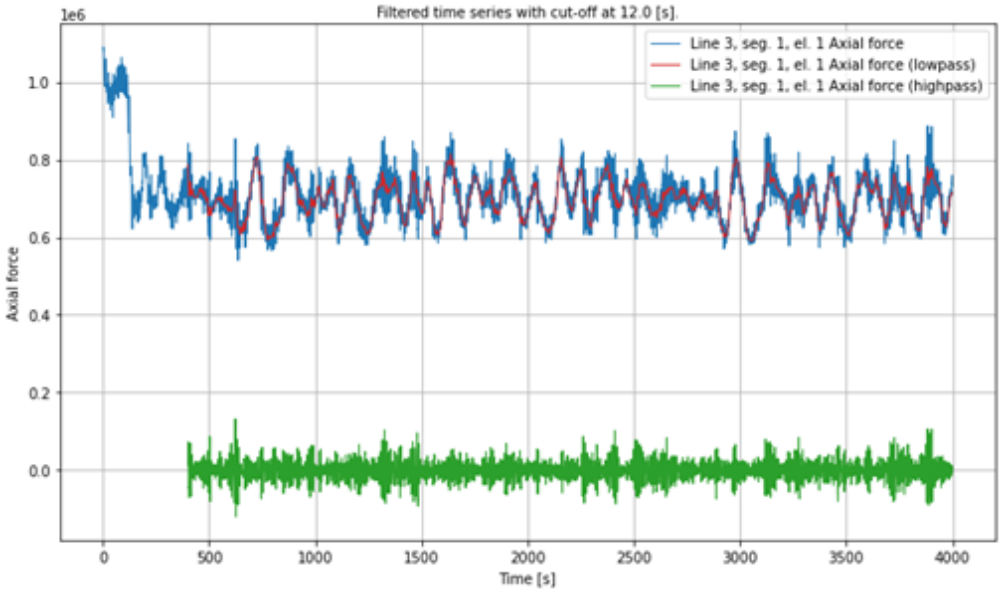

Figure C.3: Filtered time series for axial force of ML3 - DLC 1.

C.2 Design Load Case 8

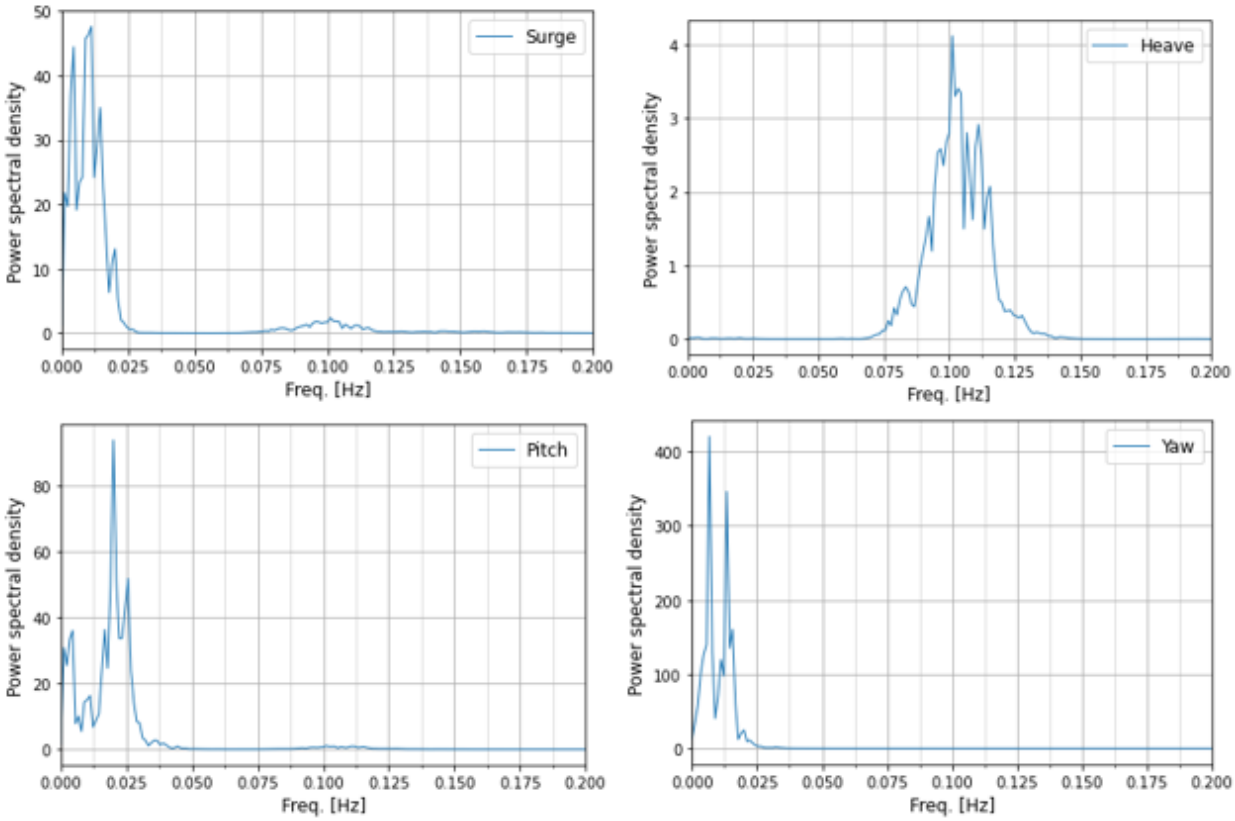

Figure C.4: Motion response spectrum, DLC 8.

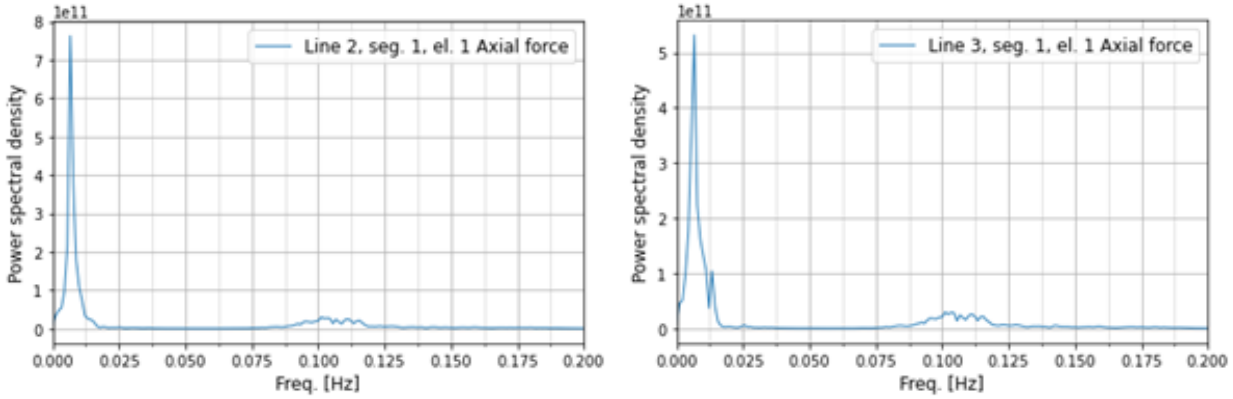

Figure C.5: PSD of line tension in DLC 8 for (a) ML2 (b) ML3.

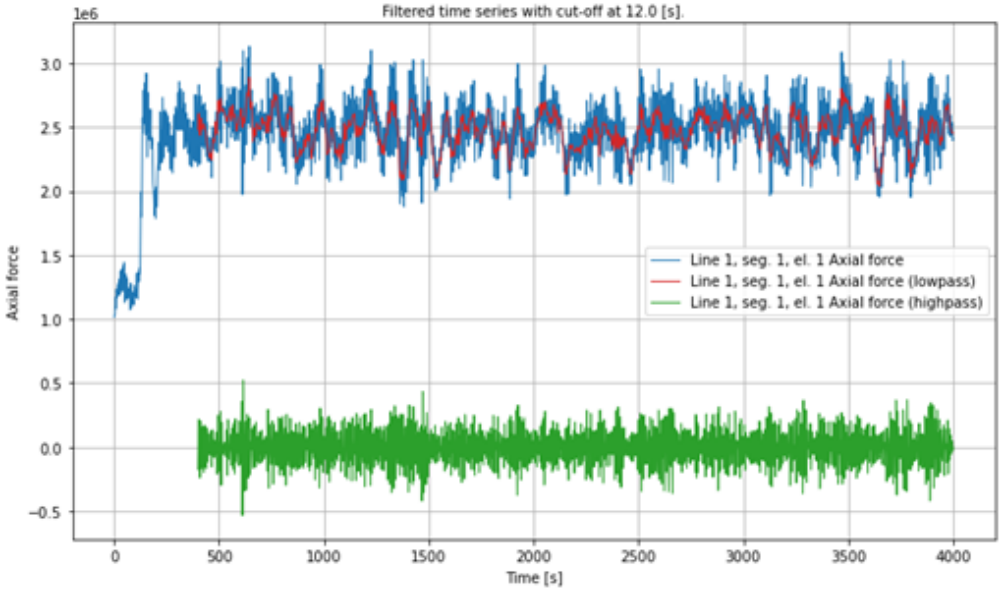

Figure C.6: Filtered time series for axial force of ML1 - DLC 8.

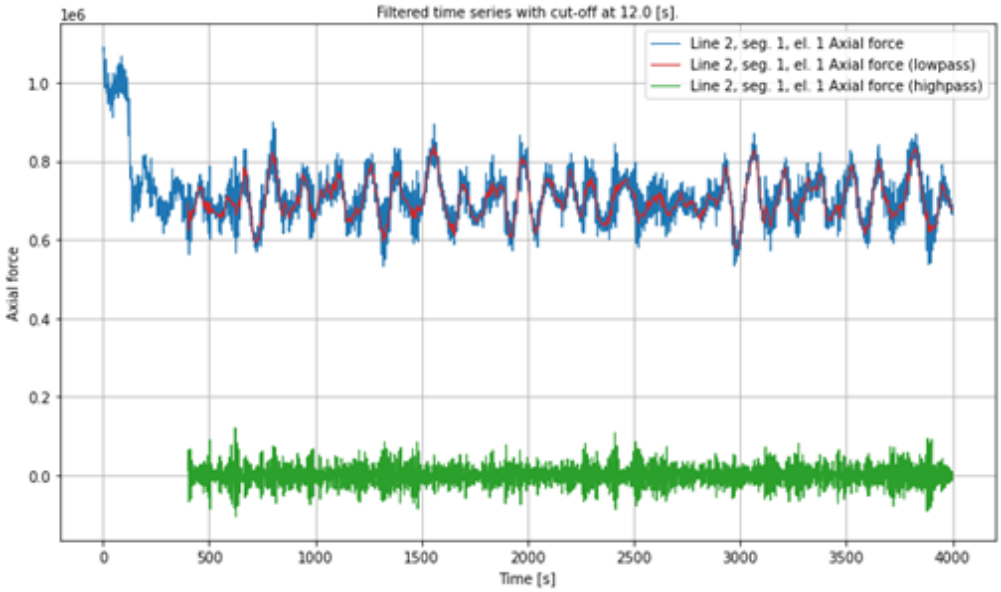

Figure C.7: Filtered time series for axial force of ML2 - DLC 8.

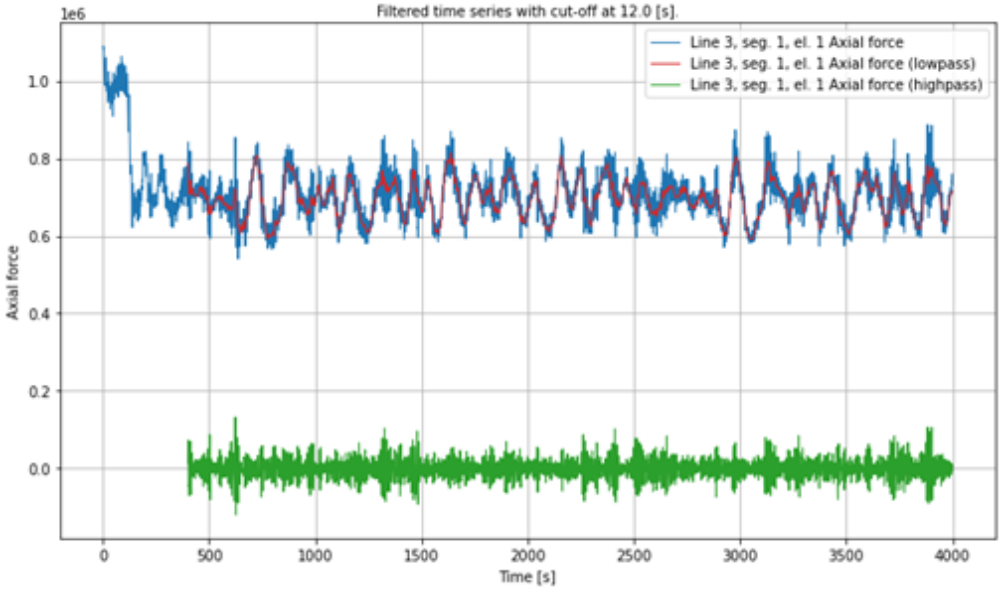

Figure C.8: Filtered time series for axial force of ML3 - DLC 8.

C.3 Design Load Case 21

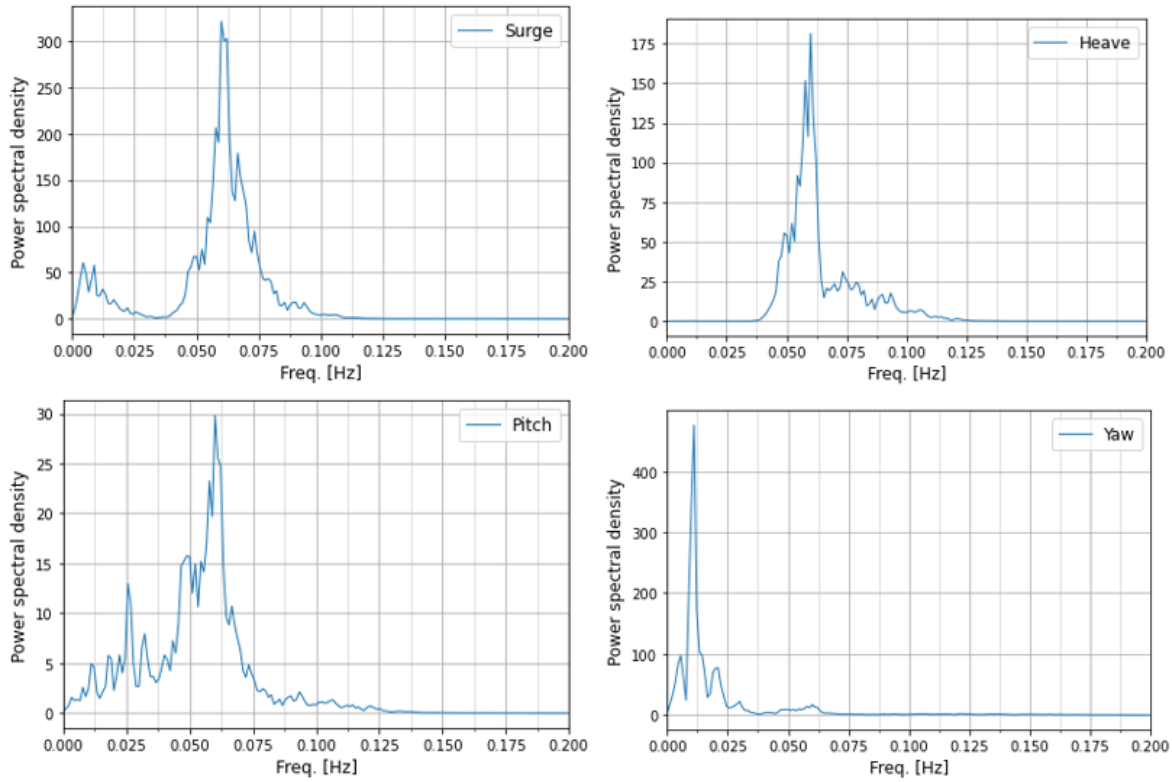

Figure C.9: Motion response spectrum, DLC 21.

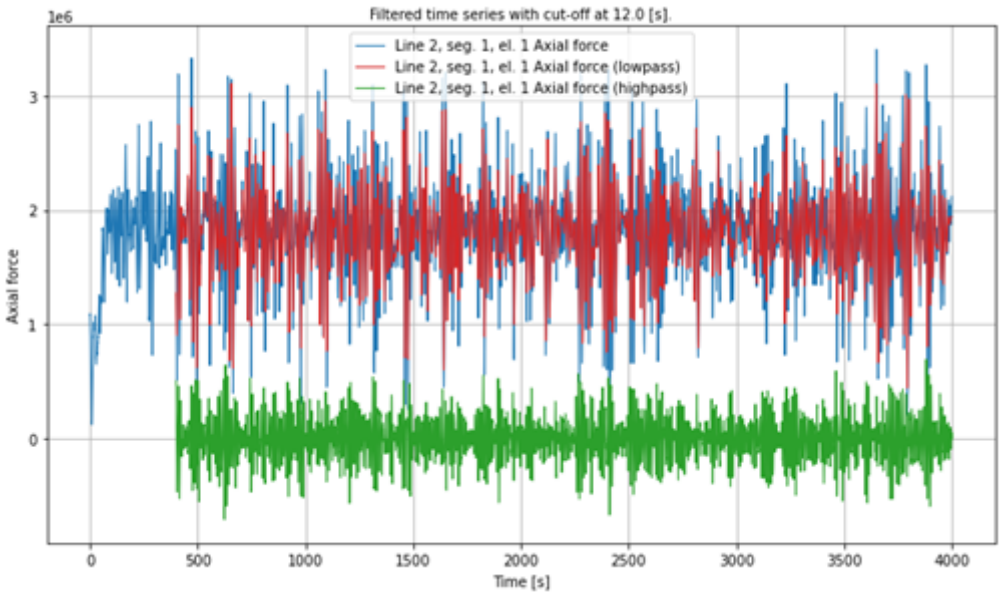

Figure C.10: Filtered time series for axial force of ML2 - DLC 21.

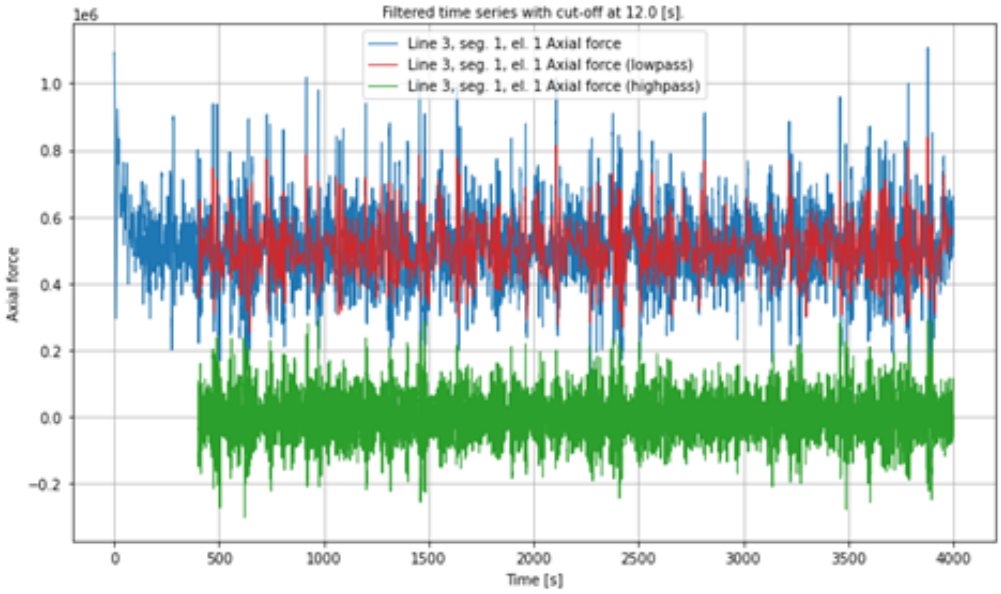

Figure C.11: Filtered time series for axial force of ML3 - DLC 21.

D Platform Motion response

D.1 Design Load Case 1

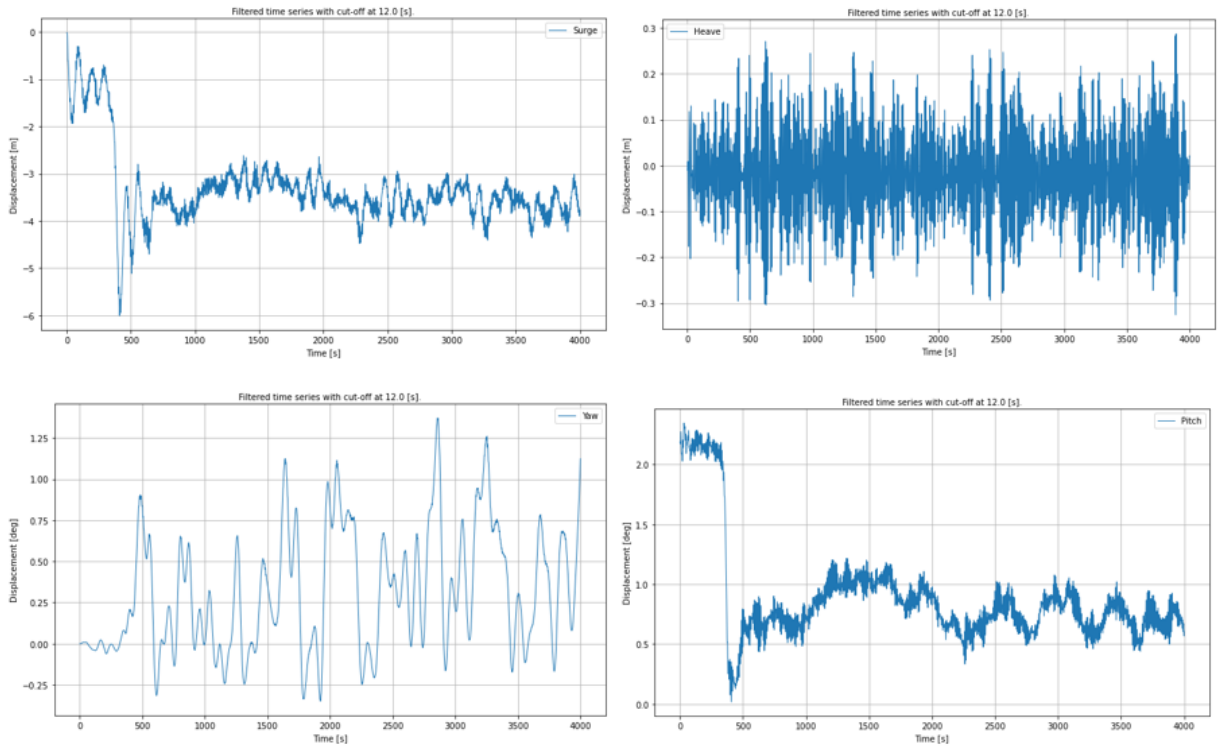

Figure D.1: Platform motion response - DLC 1.

D.2 Design Load Case 8

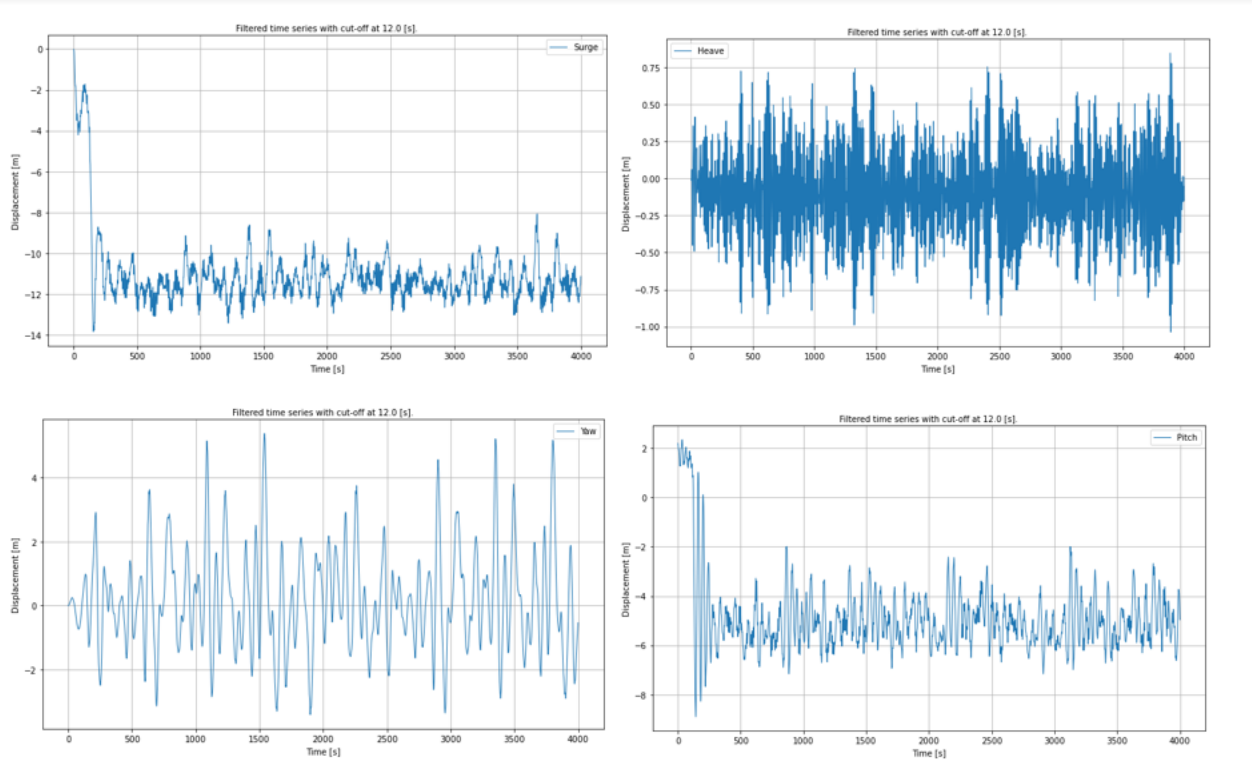

Figure D.2: Platform motion response - DLC 8.

D.3 Design Load Case 21

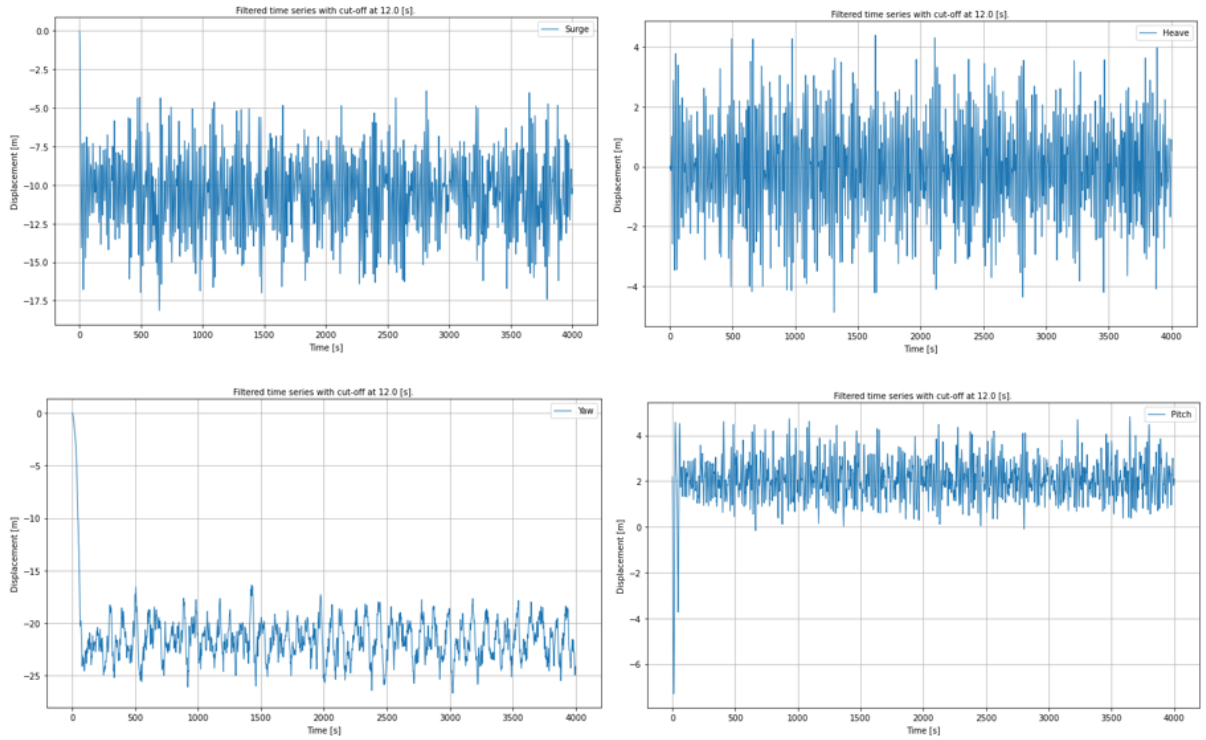

Figure D.3: Platform motion response - DLC 21.

E Accumulated Fatigue Damage

E.1 Miner Palmgren Sum - All sea states

For the following tables in appendix E.1, the accumulated fatigue damage is shown for three different cases; regular S-N design curve from DNVGL-OS-E301 [11], 1-hour mean and cycle means. The accompanying mean load is also shown, together with the sea state number. The probability of occurrence is accounted for in all cases.

Table E.1: Accumulated fatigue damage and associated damage for ML1.

Sea state	**Mean load [% MBL]**	**DNVGL-OS-E301**	**1-hour mean**	**Cycle mean**
1	9.90	7.89E-08	2.17E-08	2.19E-08
2	16.69	2.10E-06	1.40E-06	1.48E-06
3	18.82	1.36E-06	1.18E-06	1.20E-06
4	15.54	1.62E-06	9.25E-07	9.52E-07
5	14.36	6.17E-07	3.03E-07	3.12E-07
6	13.82	1.75E-07	8.00E-08	7.99E-08
7	17.05	8.96E-07	6.24E-07	6.51E-07
8	19.21	5.55E-07	5.06E-07	5.15E-07
9	15.96	1.11E-06	6.69E-07	6.94E-07
10	14.94	1.13E-06	6.03E-07	6.22E-07
11	14.42	1.79E-06	8.87E-07	9.09E-07
12	17.91	1.76E-07	1.37E-07	1.42E-07
13	20.22	2.37E-07	2.43E-07	2.53E-07
14	16.61	8.23E-07	5.41E-07	5.79E-07
15	15.62	9.20E-07	5.31E-07	5.72E-07
16	15.46	2.15E-06	1.22E-06	1.37E-06
17	16.45	2.78E-06	1.79E-06	2.02E-06
18	21.05	1.54E-08	1.73E-08	1.87E-08
19	16.56	1.33E-07	8.69E-08	1.01E-07
20	17.14	4.30E-07	3.03E-07	3.51E-07
21	13.99	1.14E-08	5.36E-09	1.69E-08
-	**SUM**	1.91E-05	1.21E-05	1.29E-05

Table E.2: Accumulated fatigue damage and associated damage for ML2.

Sea state	**Mean load [% MBL]**	**DNVGL-OS-E301**	**1-hour mean**	**Cycle mean**
1	6.95	7.51E-09	1.43E-09	1.42E-09
2	5.24	3.57E-08	5.53E-09	5.62E-09
3	4.96	2.40E-08	3.59E-09	3.61E-09
4	5.58	6.51E-08	1.05E-08	1.05E-08
5	5.81	1.31E-08	2.18E-09	2.18E-09
6	5.84	3.70E-09	6.14E-10	6.13E-10
7	5.19	1.81E-08	2.79E-09	2.82E-09
8	4.90	9.00E-09	1.34E-09	1.34E-09
9	5.47	3.68E-08	5.84E-09	5.87E-09
10	5.68	2.55E-08	4.15E-09	4.15E-09
11	5.68	2.43E-08	3.96E-09	3.94E-09
12	5.05	4.07E-09	6.15E-10	6.22E-10
13	4.77	4.38E-09	6.41E-10	6.36E-10
14	5.34	2.70E-08	4.24E-09	4.23E-09
15	5.52	3.62E-08	5.80E-09	5.76E-09
16	5.44	7.42E-08	1.17E-08	1.15E-08
17	10.81	5.41E-07	1.67E-07	1.58E-07
18	4.62	3.17E-10	4.56E-11	4.55E-11
19	5.22	4.33E-09	6.67E-10	6.57E-10
20	10.64	6.79E-08	2.05E-08	1.92E-08
21	13.76	4.99E-10	2.27E-10	2.26E-10
-	**SUM**	1.02E-06	2.54E-07	2.43E-07

Table E.3: Accumulated fatigue damage and associated damage for ML3.

Sea state	**Mean load [% MBL]**	**DNVGL-OS-E301**	**1-hour mean**	**Cycle mean**
1	6.96	7.67E-09	1.46E-09	1.45E-09
2	5.20	3.26E-08	5.01E-09	5.07E-09
3	4.87	2.36E-08	3.49E-09	3.54E-09
4	5.47	6.62E-08	1.05E-08	1.06E-08
5	5.75	1.74E-08	2.86E-09	2.89E-09
6	6.26	6.81E-09	1.19E-09	1.20E-09
7	5.14	1.68E-08	2.57E-09	2.59E-09
8	4.80	8.99E-09	1.32E-09	1.35E-09
9	5.37	3.60E-08	5.66E-09	5.67E-09
10	5.64	3.06E-08	4.97E-09	4.98E-09
11	6.12	4.29E-08	7.37E-09	7.39E-09
12	5.00	3.77E-09	5.67E-10	5.72E-10
13	4.69	4.33E-09	6.27E-10	6.33E-10
14	5.23	2.59E-08	4.00E-09	4.03E-09
15	5.47	3.62E-08	5.75E-09	5.73E-09
16	5.91	9.65E-08	1.62E-08	1.58E-08
17	3.89	3.36E-08	4.43E-09	4.37E-09
18	4.55	3.18E-10	4.53E-11	4.59E-11
19	5.66	5.55E-09	9.02E-10	8.92E-10
20	3.67	4.46E-09	5.75E-10	5.81E-10
21	3.13	1.21E-11	1.47E-12	1.55E-12
-	**SUM**	5.00E-07	7.95E-08	7.94E-08

E.2 Fatigue Damage Figures

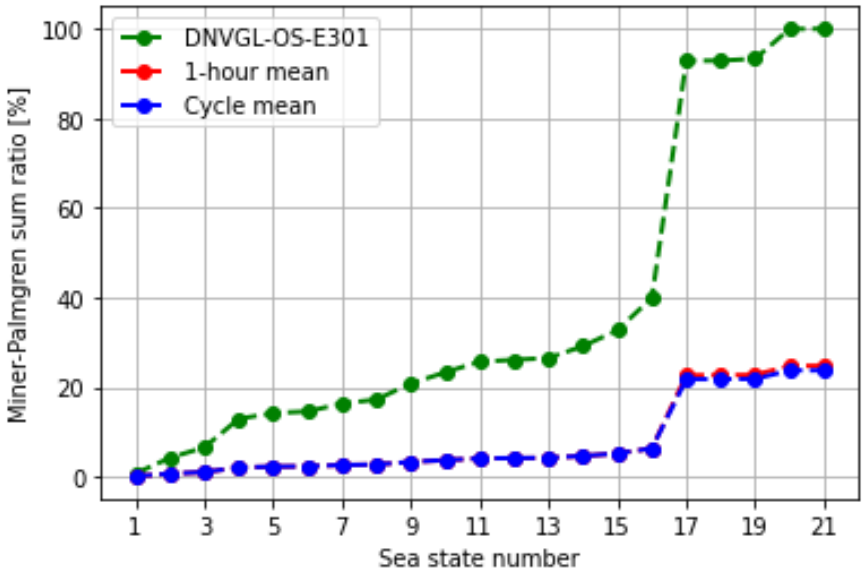

Figure E.1: Accumulated fatigue damage ratio with and without mean load correction for ML2.

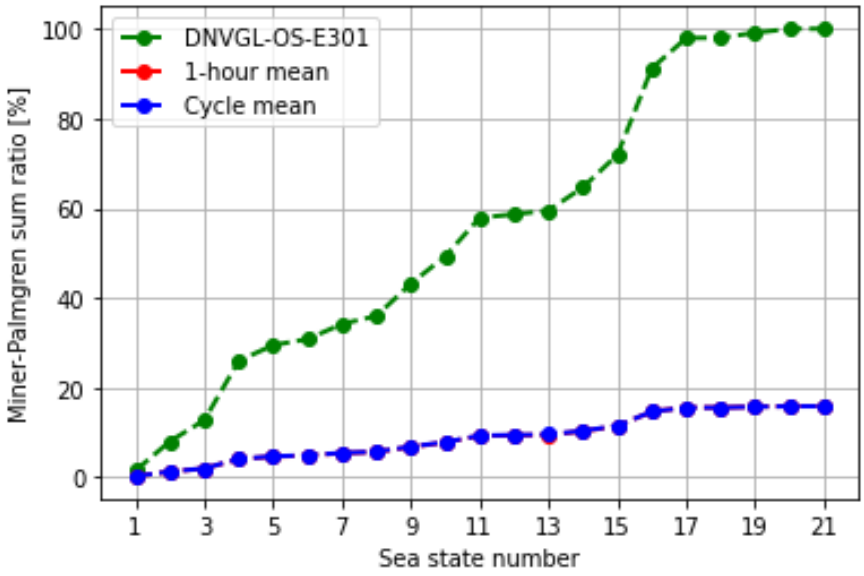

Figure E.2: Accumulated fatigue damage ratio with and without mean load correction for ML3.

Norges miljø- og biovitenskapelige universitet
Noregs miljø- og biovitskapelege universitet
Norwegian University of Life Sciences

Postboks 5003
NO-1432 Ås
Norway